Universidad Carlos III de Madrid

Escuela Politécnica Superior

Aerospace Engineering

Bachelor Thesis

Design and Fabrication of Conventional and Non-Conventional Emissive Probes for Plasma Diagnostics

---

Author

Marcos López Roso

Supervisors

Xin Chen

Jaume Navarro Cavalle

June 2018

Acknowledgements

To my family and friends, for their help and unwavering support all these years. *All that I am or hope to be I owe it to them.* And above all, for making the journey much more enjoyable.

To Xin, for guiding me through research as a magnetic line leads a free charge. To Jaume, for teaching me that even something as small as an ion can propel a rocket under the right circumstances.. To Mick, for showing me that there is not a problem that a particular kind of tape can not solve. To the Aerospace Department at UC3M and many other professors, for these years of shared knowledge. For their continuous help and dedication, without which this project could not have been possible.

Abstract

Plasma physics importance has increased over the last decades given the relatively new industrial and technological applications that involve this state of matter. For a proper performance and understanding of these applications, experimental techniques are required to determine plasma properties and to verify current main theories. This project aims to use current idealized main theories in plasma diagnostics to develop emissive probes that are able to take proper experimental measurements of plasma potential.

The first part of the thesis will develop an idealized description of the interaction between probes and plasmas. Non idealizations will be defined given the disturbance caused by a probe presence inside a plasma region. Following the plasma-probe system, the Floating Point Method accuracy will be discussed regarding experimental plasma diagnostics. This method will be established as a convenient enough approximation to measure experimental plasma bias. A material study will be performed in order to define and propose non-conventional low work function materials such as LaB_6, CeB_6 and $C12A7 : e^-$ for thermionic applications.

Both thoriated tungsten conventional probes and low work function non-conventional probes will be discussed. Due to the difficulty to machine boride emissive tips during the project time-frame, non-conventional emissive probe designs and manufacturing process will be proposed for future projects. After the chosen design for conventional probes, their thermal model will be performed, dealing with the importance of the emitted electron current on the energy balance at high temperatures. These models will show the approximate power range at which the actual devices need to be operated to be in the saturated floating point region.

Finally, the manufactured probes will be used to acquired experimental data. The results will seem to agree with the expected floating point behavior at high temperatures, where it is is extended to saturate. Measured potential deviations dependent on probe filament radius will be regarded.

Contents

Nomenclature

Abbreviations

EM	Emitted Electrons
EP	Emissive Probe
IP	Inflection Point
LP	Langmuir Probe
PE	Plasma Electrons
PI	Plasma Ions

Greek Symbols

ϵ	Emissivity factor [-]
ϵ_0	Medium permittivity $[\frac{F}{m}]$
η_{em}	Emissive efficiency
λ_B	Band structure material specific correlation factor
λ_{sh}	Sheath thickness [m]
ρ	Space charge density
ρ_0	Material resistivity at T = 293 K and p = 1 atm.[$\Omega\cdot$ m]
ρ_m	Material resistivity [$\Omega\cdot$ m]
ρ_t	Solid tungsten resistivity [$\Omega\cdot$ m]
ρ_{LaB6}	Lanthanum hexaboride resistivity[$\Omega\cdot$ m]
σ	Stefan–Boltzmann constant $[\frac{W}{m^2K^4}]$

Roman Symbols

$\dot{m}_t$	Helicon thruster mass flow rate [sccm]

A_0 Universal constant $[\frac{A}{m^2K^2}]$

A_G Generalized Richardson constant $[\frac{A}{m^2K^2}]$

A_p Filament cross section area $[m^2]$

E Electric field $[\frac{N}{C}]$

I_e Plasma electron current [A]

I_h Heating circuit current [A]

I_p Net probe current [A]. Emitted plus collected current

I_p Net probe current [A]

I_{em} Emitted electron current [A]

I_i Plasma ion current [A]

I_{th} Electro random thermal current [A]

J Electron angular momentum $[\frac{kg \cdot m^2}{s}]$

k_B Boltzmann constant [eV/K]

L Filament length [m]

m_e Electron mass [kg]

m_i Plasma ion mass [kg]

N_∞ Plasma electron density $[m^{-3}]$

q Particle electrical charge [C]

q_e Elementary charge [C]

q_i Ion electric charge [C]

q_{em} Power loss due to electron current emission[W]

q_{heat} Power supplied by the heating circuit [W]

q_{rad} Emissive material radiative power [W]

R Resistance [Ω]

r_m Relative minimum of a potential distribution curve, $|\frac{dV}{dx}|_{r_m} = 0$

r_p Probe filament radius $[m]$

r_{av}	Average quantum mechanical reflection coefficient
S_p	Probe emissive material surface [m^2]
T_e	Electron temperature [K]
T_p	Emissive probe temperature [K]
T_{em}	Temperature of the knee on the V_f-T_p curve in the Floating Point Method
v_e	Electron velocity [m/s]
V_f	Floating Potential [V]
V_p	Probe bias [V]
V_s	Plasma potential [V]
V_s^*	Plasma potential approximation [V]
W	Work function [V]

List of Figures

List of Tables

CHAPTER 1

Introduction

The properties, behavior and application of the first three states of matter, have been deeply studied during the contemporary age. It is understood that the state changes occur due to the attraction and repulsion forces between elemental atoms in a material. When the repulsion forces are negligible respect to the attraction ones, the solid state befalls. If the material atoms energy increases, their vibration amplitude will increase up to the point where they are able to move and the solid bonding is broken, leading the way to the liquid state. More energy can be applied so that the atom kinetic energy overcomes completely the attraction forces between them and a gas is formed [51]. Over the last century, two other states of matter have been discovered.

On the lower end of the scale, the Bose–Einstein condensate was described in 1924 by Satyendra Nath Bose and Albert Einstein as a microscopic quantum phenomena for some materials, for temperatures close to the absolute zero when some material particles, the bosons, fulfill their lower quantum state [34]. On the higher end of the energy scale so far, it was discovered on the early 1900s that if the electrons of a gas where provided more energy, gas properties were substituted by other different ones and hence, a change of material state was taking place. This new state was named in the 1920s by I. Langmuir as *plasma* [23].

Plasma physics have been studied during the past century as since its discovery, it is suspected to be one of the most abundant matter in the universe, explaining some previously unknown issues of astrophysics, in particular related to stars. Its technological importance has substantially increased during the past two decades given its found application to Electric Propulsion and Fusion Reactors.

1.1 Plasma Basics and Applications

Plasma is the fourth state of matter, composed by a gaseous blend of electrons and ions which properties differ to those of a regular gas or fluid. A plasma contains free charged particles, but should be globally quasi-neutral [30]. The quasi-neutrality condition imposes that in a considered region of plasma, the total electric field is null, $\vec{E} = 0$. For the ions on the plasma not to bind the electrons and form a neutral atom, the average kinetic energy of the electron plasma population needs to further exceed the Coulomb binding energy of the electron-ion interaction. This is usually known as the plasma condition [50].

Regarding its current applications, nuclear fusion is the process in which different atom nuclei are recombined to form heavier nuclei, as well as other subatomic particles, releasing a vast magnitude of energy. Three conditions have been established for fusion to occur: high temperatures, time-stability and high densities [60]. Even though the current difficulty yields on achieving reaction stability at high densities, the temperature requirement sets the mechanics of the element in its plasma state. The understanding of these mechanisms is key then to make progress in fusion applications.

Plasma physics has also been found as an application to space propulsion, given the limitations in specific impulse of chemical rockets. The specific impulse is proportional to the propellant mass and temperature ($I_{sp} \propto \sqrt{\frac{T}{M}}$) [61]. In chemical rockets, this limitation comes from the combustion exothermic reaction, in which the maximum temperature achieved is limited. However, in electric propulsion, the limit in energy provided to the propellant is only set by the electric power source of the spacecraft. That is why it is commonly said that electric propulsion is power limited [68]. As in electric propulsion the propellant is in its plasma state, at much higher temperatures than in chemical propulsion, higher specific impulses are achieved. This benefits are counteracted by the fact that plasma mass flow from an electric thruster is much smaller than that of a chemical rocket. Hence, electric propulsion thrusters are used in low thrust maneuvers. Given all these implications, it can be discussed that a better understanding on plasma physics and diagnostics will be useful in the improvement of these kind of space applications

Other current applications of plasma related to manufacturing techniques are, among others, plasma materials processing [9] and photo-lithography [66], as well the understanding of some astrophysics phenomena [52].

1.2 Plasma Diagnostics. State of the art

Under this terminology, one could classify every experimental technique intended to deduce information about a material which is in its plasma state. Plasma physics is a subject still being studied and then, sometimes plasma properties either are not fully understood or they would require long analytical derivations. Plasma diagnostics shall make use of the known valid plasma theories to provide its users with accurate information about the parameters of a plasma. As explained in [30], depending on the methods used, the type of plasma to consider and the plasma parameters measured, there exists several branches of diagnostics.

- Plasma particle flux measurements
- Magnetic measurements
- Plasma refractive index
- Electromagnetic emission from free electrons
- Electromagnetic emission from bound electrons
- Scattering of electromagnetic waves
- Neutral atom diagnostics
- Fast ions and fusion products

With regards to that categorization, this project will be focused on *plasma particle flux measurements*, which consists in analyzing the behavior of the flows of species inside a plasma. This is achieved by studying the perturbation that a probe causes in a plasma. For its measurements, different kind of probes may be immersed in a plasma region. For that reason, this technique can only be used in plasmas which conditions allow the survival of the probe for a period of time.

Irving Langmuir is perhaps the most recognized researcher when this plasma diagnostic method is involved, due to his contribution to the investigation of collective probes (also referred as *cold* probes or *Langmuir* probes). These devices, immersed in a plasma and with a time changing potential through them, work under the plasma electron collection that takes place when the probe is biased above the plasma. However, for measuring plasma potentials, the interesting voltage range to study is that which is close (higher and lower) to the plasma one. Since Langmuir probes only work for bias above the plasma, emissive probes appeared to provide measurements on a better probe potential range. In principle, emissive probes would work by emitting electrons when biased below the plasma, and as a Langmuir probe for bias

above the plasma. From this emission - collection change of behavior, the plasma potential will be inferred after a deeper analysis.

For electron emission not only a potential distribution is required on the probe-plasma system, but also energy needs to be provided to the surface electrons of the emissive material. Thermionic materials are those used, as they are in such classification given that their properties allow a substantial electron emission when heated to a certain temperature.

1.3 Emission Mechanisms and Materials

Due to material advancements, it is believed that the emissive probe performance cen be improved respect to conventional emissive materials. For the following project, some terms need to be introduced beforehand for a better understanding of the mechanisms used. The work function of a material can be defined as the energy required to extract an electron from the material surface. This is a key property in electron emission applications, as it will set the magnitude of the emitted electron current from the material surface. Electron emission relies on the excitation of such particles in a material. To explore the capability of a material as an electron source, three main types of emission can be defined [65]:

- **Thermionic emission**. Flow of electrons arising from a material surface at a given temperature. It is defined by the Richardson-Dushman equation. Electrons are released from the material if enough kinetic energy is provided to them in the presence of a potential difference [29].
- **Field emission** is a quantum process in which electrons emerge from the material in the presence of strong electric fields that reduce the energy barrier for the particle to be emitted. Hence, the material does not have to reach a certain temperature and it is referred as a cold process [18].
- **Photoelectric emission** is a phenomenon in which electrons absorb energy from light radiating the surface, at a given temperature. When this energy is enough as to reach the work function, electrons are emitted from the surface. These particles are usually named *photo-electrons* [13].

Over the last century, this emission processes have been key on the field of electronics. Apart from plasma diagnostics, some other applications for which they have been proven to be useful are listed below:

- Vacuum tube electronics [19]
- Thermionic energy converters [35]

- Electric propulsion thrusters and neutralizers [53]
- Electron microscopy [58]

Electron emission is also being currently studied to be used in photo-cathodes and photo-anodes, taking advantage of direct solar radiation in space. Devices are being designed to emit electrons that would then be used to split water molecules for the production of oxygen and hydrogen [24]. It can be then inferred that for their enhanced use in electronics and space engineering, electron emission mechanisms will play an important role in the years to come.

1.4 Thesis Structure and Project Objective

The aim of this thesis consists in the collection of plasma potential experimental data through emissive probes. For that purpose, firstly a literature review will be performed in order to theoretically describe the plasma-probe interaction. For this system, the idealizations and non-idealizations considered will be depicted.

Next, the design and manufacture of conventional thoriated tungsten probes will performed. Different probe radius will be used during manufacturing process, to see the influence of the probe radius on the Floating Point technique. Using a heat balance model and the ion to electron fluxes ratio for space charge limited emission, a model has been developed. This model will estimate the heating current required by each probe to reach the saturation region in the Floating Point Method. After these operational parameters are defined, the plasma potential will be measured using experimentally the floating potential technique.

Regarding the improvement on emissive probe performance using the recent advancements on low work function emissive materials, non-conventional emissive probe designs will be proposed. For that purpose, LaB_6, CeB_6 and $C12A7 : e^-$ will be studied.

From both the plasma potential experimental results, with conventional probes, and the developed model, it was observed that the power loss due to electron emission was not negligible. Experimentally, it was also observed the probe radius influence on the floating potential saturation. The thermal response for different probe radius showed a higher stability for larger probe radius. It was observed that the smaller the probe radius, the saturation region on the FP method plateaued at higher potentials.

With regards to the non-conventional probes, it was concluded that since material properties are strongly dependent on their formation mechanism, each species should be treated experimentally to determine accurately its properties. The key design features for a proper probe function, and the parameters affecting it, were described. Manufacturing difficulties were assessed and alternative machining processes were proposed.

CHAPTER 2

Emissive Probes

2.1 Theoretical Operational Principles

Given the importance of the plasma potential, it is essential to design a device that is able to measure it accurately. Emissive probes (EP) are stated to measure such parameter precisely enough, despite lacking the ability to measure directly the temperature or the density of plasma [26]. They are as well one of the easiest devices to implement in a system [59]. Such probes consist of an emitting filament placed in a plasma cloud. Dependent on the potential difference between probe and plasma, a consequent net current occurs.

When the probe is biased, the plasma-probe interaction results in a potential distribution as in Figure 2.2. This distribution will be considered as a sheath surrounding the cathode. The sheath shields the local disturbance form the probe, keeping the plasma globally quasi-neutral [41]. By observing the potential distribution, the current of emitted electrons (EM), plasma electrons (PE) and plasma ions (PI) can be quantitatively described. For instance, when the bias of the probe is very negative relative to the plasma potential (left panel on Figure 2.1), EM are accelerated to plasma, whereas PE are repelled and PI are attracted by the probe. On the other hand, if the probe is biased positive relative to the plasma potential, EM are reflected back while PE are attracted and PI repelled by the probe (right panel on Figure 2.1). The net current of emitted electrons, plasma electrons and plasma ions thus varies with the interaction probe potential–plasma potential ($V_p - V_s$). Such current-voltage characteristics can be used to infer the real plasma potential.

The emitted electrons population has a velocity distribution. Even in case the probe is biased slightly above the surrounding plasma, if an electron is emitted at a high enough velocity to trade its kinetic energy to overcome the potential barrier, it can reach a point in the sheath region that is still biased negative relative to the plasma (Figure 2.2, curve 4).

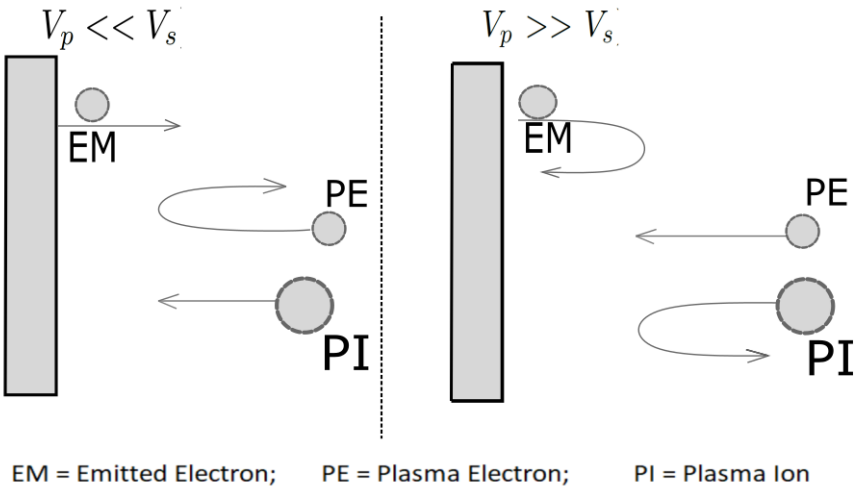

Figure 2.1: Species behavior with probe bias.

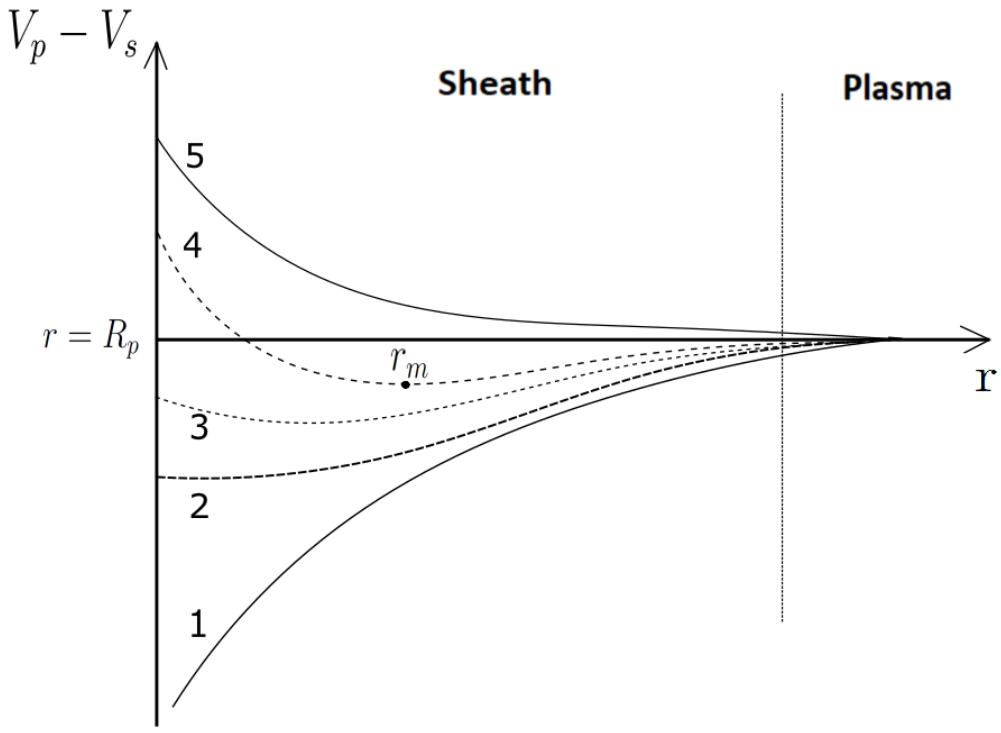

Figure 2.2: Sheath potential distribution

Defining the Electric Field ($\vec{E}$) as a vectorial field modeled by the interaction between electric charges, the force exerted on a point particle of charge q can be defined. If the field is assumed to be one-dimensional, steady in time and electrostatic, then it is given by [2]

$$m_e \frac{d\vec{v_e}}{dx} = q\vec{E} \tag{2.1}$$

Moreover, defining the electric potential as the work of the electric field and applying Faradays' Law for a steady field, it can be expressed as

$$\vec{E} = -\vec{\nabla}V = \frac{\partial V}{\partial r}\vec{e_r} + \frac{1}{r}\frac{\partial V}{\partial \theta}\vec{e_\theta} + \frac{\partial V}{\partial z}\vec{e_z} \tag{2.2}$$

Consequently, the simplest case in one dimension, for an axisymmetric field where $\frac{\partial V}{\partial r} = \frac{dV}{dr} = \frac{dV}{dx}$, yields

$$\frac{dv_e}{dx} = -\frac{q}{m_e}\vec{\nabla}V = -\frac{q}{m_e}\frac{dV}{dx}\vec{i} = \frac{\mid q \mid}{m_e}\frac{dV}{dx} = K \cdot \frac{dV}{dx} \tag{2.3}$$

Since $\frac{dV_x}{dx}$ is the slope of the potential distribution curves (Figure 2.2) and given the fact that the shape of those curves is expected to be as shown in the graph, the particle behavior can be inferred. For radial positions where the potential distribution $V_s(r)$ has positive slopes, equation 2.3 shows that the emitted electron will be accelerated towards the plasma . However for negative slopes, the electron will encounter an opposite force that will reflect it back to the probe.

Considering an emitted electron that is able to arrive at least at such point in space at $r = r_m$ (Figure 2.2) that fulfills $\frac{dV}{dx} > 0$ .In such case, that EM will be accelerated towards the plasma instead of being reflected back to the probe.

Consequently, for probe bias slightly higher than the space potential, high velocity EM can still reach the plasma. An increment in V_p increases the distance that EM need to travel to overcome the potential barrier and get accelerated. As a result, for $V_p > V_s$ there will be an electron emitted (I_{em}) current that will decrease as V_p increases, until no emitted current is achieved.

2.1.1 Current-Voltage Characteristics

The most characteristic means to analyze the system is described here quantitatively as the current-voltage (I-V) curve. Langmuir probe theory sets the following assumptions for electron collection [44] :

- Electrons follow a Maxwellian velocity distribution, at thermal equilibrium.
- Plasma is considered collision-less, non-magnetized, isotropic, homogeneous and electrostatic.

Planar theory assumes that the sheath thickness is very small compared to the probe radius ($\lambda_{sh} << r_p$). In such case, angular momentum of the particles can be neglected and no orbital effects are considered. The plasma electron current collected for bias above the plasma potential describes a saturation behavior, which is constant (Figure 2.3) [33]. For the following model, **Space Charge Effects** (SCE), that result in non-monotonic potential as in Figure 2.2, curves 3 and 4, will be disregarded.

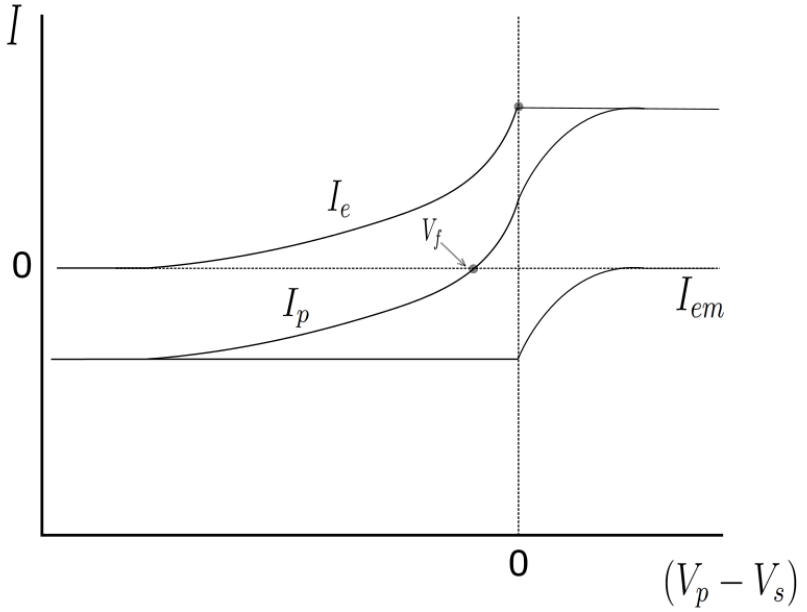

Figure 2.3: EP I-V curve. Planar collection assumption

The plasma electron current collected the probe (I_e) can be modeled as a Langmuir Probe (LP) which can be described as follows [25] [42].

$$I_e = \begin{cases} I_{th} \cdot exp(\frac{-e(V_s - V_p)}{k_B T_e}) & \text{for} \quad V_p < V_s \\ I_{th} & \text{for } V_p > V_s \end{cases} \tag{2.4}$$

I_{th} is the **electrorandom-thermal current**, commonly referred as the plasma electron saturation current. It fulfills the planar theory (Figure 2.3) and will be theoretically defined in the Appendix (A). In case of the planar assumption, it yields:

$$I_{th} = S_p e N_\infty \sqrt{\frac{k_B T_e}{2\pi m_e}} \tag{2.5}$$

with S_p the probe surface and N_∞ the electron density. From Figure 2.3, with probe bias below the plasma potential $(V_p - V_s) < 0$, the behavior of I_e can be seen to increase exponentially.

Regarding the electrons emitted by the probe, the **thermionic emission** will be the main mechanism that will be considered. Thermionic emission develops an electric current by heating up the probe. The heat introduced to the probe is converted into kinetic energy of the electrons that are emitted from the probe surface. The thermionic current has been stated to follow the Richardson-Dushman equation [29].

$$I_{RD} = A_G T_p^2 exp(\frac{-eW}{k_B T_p}) \cdot S_p, \tag{2.6}$$

with I_{RD} the thermionic current, T_p the surface temperature of the emitting material and A_G the generalized Richardson constant described in [5] as,

$$A_G = \lambda_B (1 - r_{av}) A_0 \tag{2.7}$$

with λ_B the material band structure, which describes the ranges of energies of the electrons inside a solid; A_0 the universal constant; and r_{av} the average quantum mechanical reflection coefficient. The **work function** (W) is defined as the minimum amount of energy required to rip an electron from the surface of a material. The thermionic current can be enhanced by increasing the probe temperature or using an emissive material with a lower work function 2.6.

In terms of total emitted current, I_{em} is seen to be constant for bias below the plasma potential. Most electrons are accelerated towards the plasma as long as $V_p < V_s$. When V_s is reached, emitted current does not cease intermediately. Electrons emitted at bias slightly above the plasma ($V_p > V_s$) (Figure 2.2, curve 4) with a sufficient energy, can reach a radial position space $r > r_m$ such that the potential at that point is below V_s. Thus, the electron will be still accelerated towards the plasma instead of reflected back to the probe. This hypothesis is corroborated by the analytical result obtained in equation 2.3, which shows that in such described case for $r > r_m$, $\frac{d\vec{v_e}}{dt} > 0$

The total thermionic current is modeled in [25] and when the planar assumption is applied, it yields:

$$I_{em} = \begin{cases} -I_{RD} & \text{for} \quad V_p < V_s \\ -I_{RD} \cdot exp(\frac{-e(V_p - V_s)}{k_B T_p}) & \text{for } V_p \geqslant V_s \end{cases} \tag{2.8}$$

In Figure 2.3, it can be observed how $|I_{em}|$ decreases exponentially up to no emission once $V_p - V_s \geqslant 0$. Given the up-shift of the potential distribution curve while increasing V_p (Figure 2.2, curves 3, 4, 5), it can be concluded that the higher probe bias, the higher kinetic energy an electron requires to overcome the potential barrier and get accelerated towards the plasma. Given the assumed Maxwellian velocity

distribution of the emitted electrons, the number of electrons emitted with the required kinetic energy will decrease until there are none fulfilling this condition.

According to the previous description, the total probe electron current can defined as

$$I_p = I_e + I_{em} \tag{2.9}$$

In terms of ions, plasma ion current (I_i) is negligible due to its larger mass compared to the electrons ($m_i >> m_e$). If the saturation current definition is applied to the ions (eq. 2.5), due to its larger m_i, it can be stated that $I_i << I_e$. Then, only electron current will be taken into account. In Figure 2.3, the floating potential V_f can be determined as the point where the net $I_p = 0$. As it will be discussed later, V_f can be used to infer V_s.

2.1.2 Non-ideal Effects

Space Charge

After the previously described model, it is required to depict the non-ideal effects influencing the net probe current [40]. Let us consider the distribution of electrons and ions, at their corresponding velocities, surrounding the probe. Accordingly, there must be a charge distribution in this region. Such charge density arrangement results in a potential distribution in that region of space. Gauss Law establishes Poisson's equation for the potential distribution in an electrostatic field as follows.

$$\nabla \vec{E} = \frac{\rho}{\epsilon_0} \tag{2.10}$$

Recalling equation 2.2 for the definition of an electrostatic field, it yields

$$\nabla^2 V = -\frac{\rho}{\epsilon_0} \tag{2.11}$$

with ϵ_0 the permittivity of the medium and ρ the space charge density. Notice that ρ includes EM, PE and PI and then, the distribution of each species depends on each other. In the planar case, the equation gets simplified and it yields,

$$\frac{d^2V}{dx^2} = -\frac{\rho}{\epsilon_0} \tag{2.12}$$

The integration of this equation will determine the shape of the potential distribution profiles such as in Figure 2.2.

Regarding then the charge density distribution, the possible cases will be identified as follows:

- If the probe is biased much higher than the plasma, $V_p >> V_s$ (Figure 2.2, curve 5), then:

$$\frac{d^2V}{dx^2} > 0 \qquad \frac{dV}{dx} < 0 \tag{2.13}$$

$$\frac{dv}{dx} = \begin{cases} \frac{q_e \cdot \vec{E}}{m_e} < 0 & \text{for} \quad Electrons \\ \frac{q_i \cdot \vec{E}}{m_i} > 0 & \text{for} \quad Ions \end{cases} \tag{2.14}$$

  In this case, as expected, most of the emitted electrons are accelerated on the opposite direction and therefore reflected back to the probe. At the same time, this proves that the ions are repelled by the probe. This behavior results in an **electron sheath** around the probe.

- If the probe is biased much more negatively relative to the plasma, $V_p << V_s$ (Figure 2.2, curve 1), then:

$$\frac{d^2V}{dx^2} < 0 \qquad \frac{dV}{dx} > 0 \tag{2.15}$$

$$\frac{dv}{dx} = \begin{cases} \frac{q_e \cdot \vec{E}}{m_e} > 0 & \text{for} \quad Electrons \\ \frac{q_i \cdot \vec{E}}{m_i} < 0 & \text{for} \quad Ions \end{cases} \tag{2.16}$$

  In this second case the opposite behavior is seen. Most of the emitted electrons are accelerated towards the plasma, while ions are attracted. As a result, electron charge density decays rapidly near the probe producing an **ion sheath**.

- Lastly, the issue in which $V_p \approx V_s$ is given (Figure 2.2, curve 2, 3 and 4). In such case, the acceleration in either way is lower as the difference in potential $\mid V_p - V_s \mid$ is lower than the other cases. A non-monotonic potential profile appears, given that there is a change of curvature at a distance from the probe $r > r_m$

$$\frac{d^2V}{dx^2} \mid_{r=r_m} > 0 \tag{2.17}$$

$$\frac{dV}{dx} \mid_{r<r_m} < 0 \qquad \frac{dV}{dx} \mid_{r>r_m} > 0 \tag{2.18}$$

  Given the previously described model, only electrons emitted at the sufficient kinetic energy to reach a radial position such that $r > r_m$ will encounter a $\frac{dV}{dx} \mid_{r>r_m} > 0$ and will be accelerated towards the plasma.

Space Charge Limited

It is stated in [3] that limitation of the thermionic electron current in vacuum may occur when the emitted current is increased until the Child-Langmuir threshold. At that point, the own negative space charge of the emitted current produce a retarding field for emitted electrons in the profile (Figure 2.2, curve 3). This potential distribution close to the probe surface, reflects back the EM that are not emitted at a high enough velocity to overcome that retarding field. Despite being $V_p < V_s$, not all EM are accelerated towards the plasma and thus, I_{em} is actually lower than the theoretical thermionic emitted current ($I_{em} < I_{RD}$). For the above model, this Space Charge Limited effect will be disregarded, considering only a monotonic potential profile for $V_p < V_s$. As a result I_{em} will be assumed constant for $V_p < V_s$ (Figure 2.3 & equation 2.16).

Orbital Motion

In general, to determine the electrostatic distribution produced by the densities of electrons and ions, Poisson's Potential Equation (equation 2.11) and the equations of motion produced by the electric field (equation 2.1) need to be solved [15]. Even more equations need to be coupled to the problem if orbital effects are considered. A solution for these full problems is usually obtained numerically [6].

As probe bias is increased, the sheath in cylindrical and spherical cases is expected to expand [42]. The electron current that can be collected increases because of the sheath area expanse, as developed in Appendix A. Consequently, the collected electron current I_e will not saturate for these two cases, as in Figure 2.4. Notice that the expanse is faster in spherical than in cylindrical, as the sheath radius is increased in all directions.

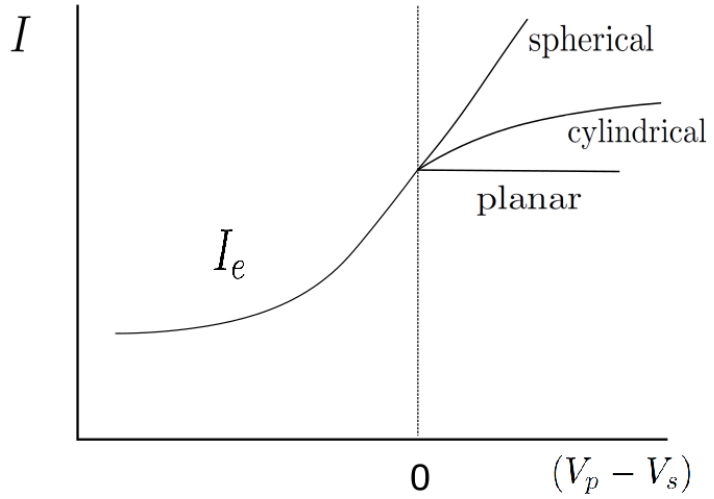

Figure 2.4: Floating potential (V_f) evolution with probe temperature (T_p).

While sheath thickness increases, the orbital motion needs to be taken into account. **Orbital Motion** differentiates between the collected and non collected electrons, for a cylindrical or spherical case, restricting the maximum angular momentum of the particles in the sheath region [42] as in Figure 2.5. To analyze it, conservation of total energy (eq. 2.19) and conservation of angular momentum (eq. 2.20) are imposed. Orbital motion imposes that even for attracted species, not all of em can be collected.

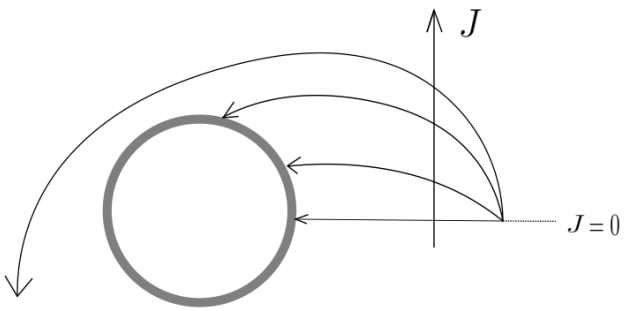

Figure 2.5: Orbital Motion Limited Theory

Defining the energy of an electron as

$$E = \frac{mv_r^2}{2} + \frac{mv_\theta^2}{2} - eV = constant \tag{2.19}$$

And the maximum angular momentum of a particle with certain energy as

$$J = mrv_\theta = constant \tag{2.20}$$

For a given collected electron total energy E^*, and operating both previous equations together, a mathematical condition for the collected electrons can be found.

$$E^* = \frac{mv_r^2}{2} + \frac{J^2}{2mr^2} - eV \tag{2.21}$$

$$r^2 m^2 v_r^2 = (E^* + eV) \cdot 2mr^2 - J^2 \geqslant 0 \tag{2.22}$$

$$J \leqslant (E^* + eV) \cdot 2mr^2 \tag{2.23}$$

The solution shows that there is a maximum angular momentum for an electron, at a certain position in the sheath region ($\vec{r}$, $V(\vec{r})$), to be collected. This can be interpreted as maximum fraction of the total energy of an electron attributed to the angular momentum, so it gets collected by the probe.

For a simplified analysis, the planar theory assumes that if the sheath thickness is small compared to the probe radius ($\lambda_{sh} << r_p$), the electron angular momentum can be neglected and the orbital effects disregarded. A full kinetic **Orbital Motion Theory** has been developed in [7].

2.2 Methods for Plasma-Potential Interpretation

Given this theoretical approach, experimental methods can be used to obtain the characteristic I-V curves and find the plasma potential. During this analysis, two methods will be discussed: the Floating Point and the Inflection Point.

2.2.1 Floating Point Method

This method comes from the previous definition of floating potential (V_f), which implies that the net current is zero ($I_p = 0$). In Figure 2.6, it can observed that the floating bias approaches the plasma potential V_s as the emitting material temperature is increased. It has been established that as thermionic emission increases, the I-V curve shifts to the right [26] (Figure 2.6). Hence, the floating potential increases, approaching the plasma potential V_s. If the curve $V_f - T_p$ is plotted, it can be observed that V_f increases rapidly with temperature at first until it saturates close to V_s (Figure 2.7).

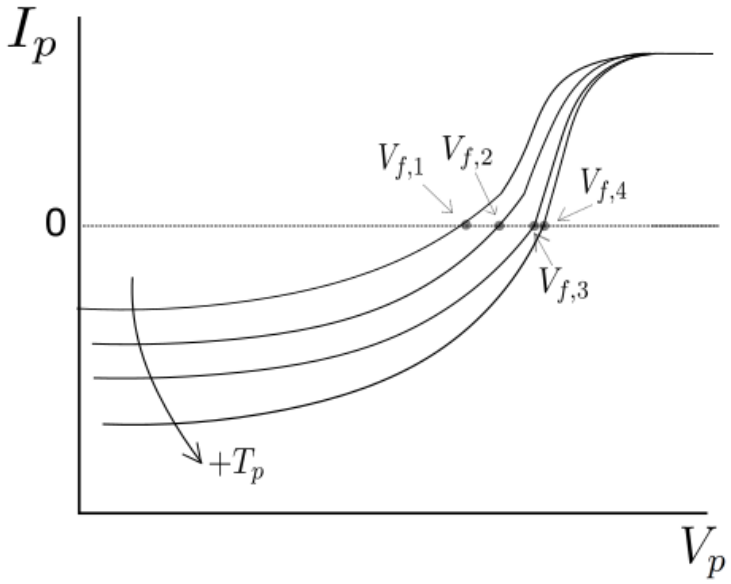

Figure 2.6: I-V curve variation with probe temperature

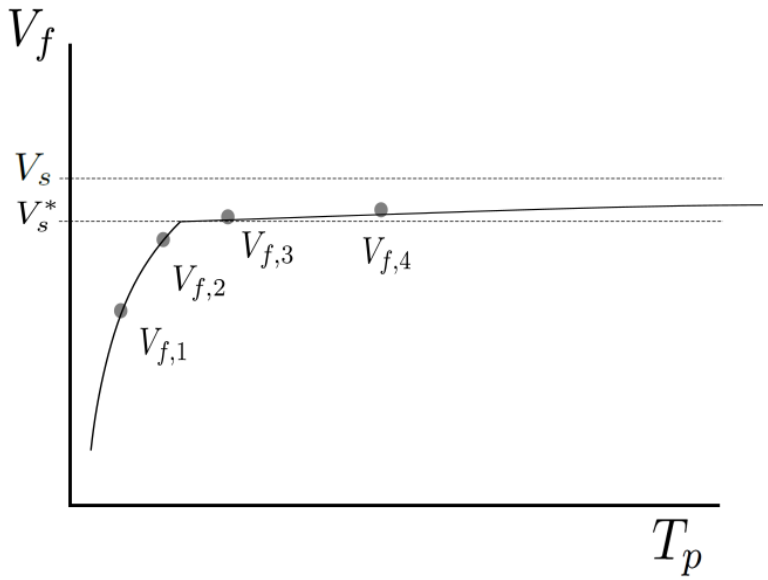

Figure 2.7: Collected current profile for different probe geometries

Given the plateau in the V_f - T_p curve behavior, a knee in the resulting plot can be observed (Figure 2.7). Such knee may be considered as the V_p at which the potential distribution curve changes from a monotonic to a non-monotonic profile (Figure 2.2, curve 2) [6] [33]. Due to the non-monotonic profile (Figure 2.2, curves 3 & 4), most EM are reflected back to the probe. Consequently, the increase of thermionic current (I_{RD}) only slightly changes V_f.

Two commonly used lab techniques can be distinguished. The first one consists in taking the knee as plasma potential. The second one lies in experimentally measuring the floating potential in the limit of large emissions, as in Figure 2.7 [6]. This saturation limit is then considered as plasma potential.

The Poisson equation (eq. 2.12) needs to be solved for the equilibrium of electrons and ions in the plasma surrounding the probe. Looking for a monotonic non harmonic solution, so that a smooth potential transition from the probe surface to the plasma is possible (Figure 2.2), the minimum potential for sheath formation can be found. The full analytical derivation has been performed in [30] and [4]. It has been found that, because of the **space charge limited effect**, the floating potential (V_f) will never reach a potential closer than T_e from the real V_s [59]. For this reason, when the floating potential saturates with temperature T_p (Figure 2.7), the approximated plasma potential V_s* is assumed to be approximated enough to the real plasma potential [26].

$$V_s = V_s^* + T_e \tag{2.24}$$

Given the fact that the curve knee and the saturation at large emissions (Figure 2.7) are similar, both approaches are assumed to have the same approximate error, $\approx T_e$. Therefore, these two experimental methods are both considered equally valid.

2.2.2 Inflection Point Method

It was developed by Smith et al. [26] in order to reduce the error of the floating potential method due to space charge effects. The method is based on the derivative of the I-V characteristic profile ($\frac{dI_p}{dV_p}$). The inflection point of the curve is defined as $\max(\frac{dI_p}{dV_p})$ or the point where the I-V curve changes from a concave to a convex behavior as in Figure 2.8. In [26], the inflection point at zero emission is said to approach the plasma potential.

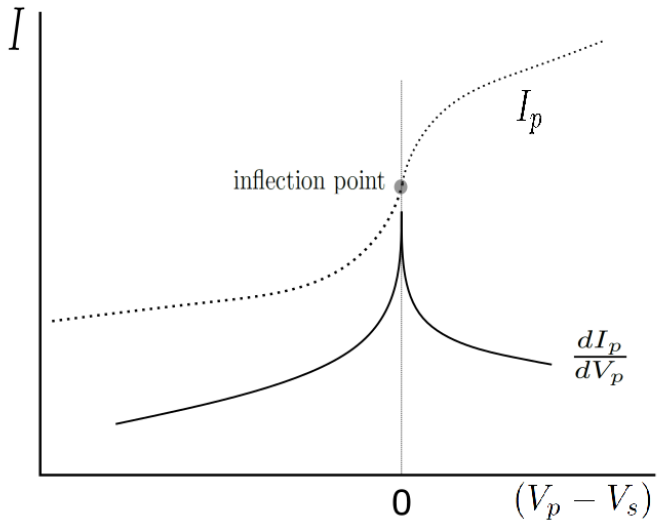

Figure 2.8: Differentiated net current $\frac{dI_p}{dV_p}$ for a cylindrical emitter with OMT in the limit of low emissions.

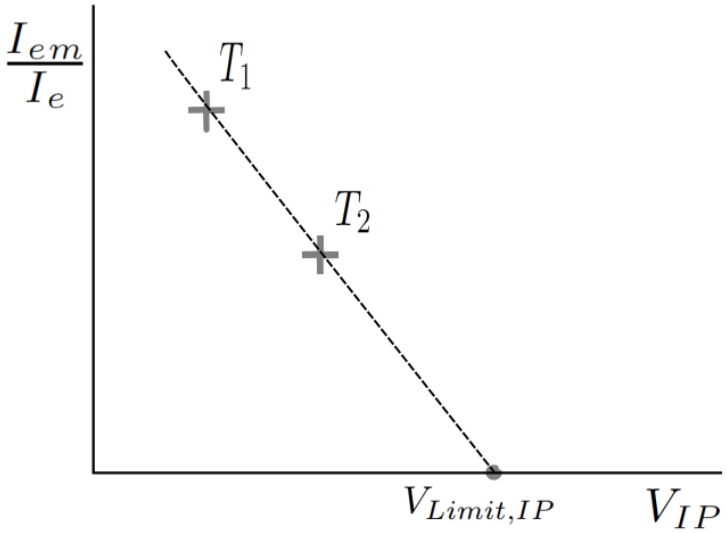

Figure 2.9: Inflection Point bias interpolation for different T_p until the limit of low emissions.

The limit of low emissions is defined as such a low thermionic level that emission occurs, but space charge effects are minimum . If there is no emission, for a Langmuir Probe, it was affirmed in [6] that the inflection point corresponds to the real plasma potential. Based on this, the inflection point at the limit of low emissions is used to approximate V_s. Inflection points are obtained for each thermionic current or probe temperature. Then, those points need to be extrapolated linearly [6], to obtain the inflection point for the zero emission condition as in Figure 2.9. The

validity for this method has been developed analytically [6] and qualitatively [8].

Langmuir probes inflection point behavior on was proved to occur in [6] for **cylindrical** emitters when a kinetic model based on the **Orbital Motion Theory** was applied as in Figure 2.8.

Comparing both methods, it is stated that usually the Floating Point underestimates the plasma potential, while the Inflection Point give results higher than the previous one, with a higher accuracy [26]. However it needs to be analyzed if the accuracy of the Floating Point Method is acceptable for this analysis.

2.3 Conventional Emissive Probes

A simple design of a common EP consists of a loop of a cylindrical conductive wire. The filament protrudes out of one end of a cylindrical insulating container. The filament is connected through the shaft to the measuring circuit by wires. The shaft prevents both the electrical connection between both sides of the filament, and any connection between the probe circuit to the outer plasma (Figure 2.10).

Regarding the manufacture of EP, it is typically divided into: **filament, connector wires, shaft and electronic circuits**

2.3.1 Filament

The filament at the tip will be the emitting material, thus being a key parameter in the design. In order to achieve emission levels, the wire needs to be heated up to the desired T_p.

Regarding the thickness of the wire, it is affirmed in [59] that EP radius should be kept as small as possible in order to minimize the disturbance of the plasma with the thread, as well as the energy needed to heat it. It is observed in [26] that smaller radius increased the slope of the curve relating emission current and inflection point (see Figure 18 of [26]). It was found that larger slopes implied less uncertainty when calculating the plasma potential with the Inflection Point Method. However, regarding longevity, thinner wires can melt faster by high energetic plasmas, whereas thicker ones can survive to such heat exchange by its increased conduction cooling by the supports. Thicker wires increase the life time of the probe [59] [22]. Its stated that most experiments implement wire with radius in the range of 0.0025 - 0.02 cm.

In [6], it has been analytically computed the radius variation (see Figure 4 of [6]). It has been found that the smaller the probe radius, the closer the knee of the $V_f - V_s$ curve is to the plasma potential. As a result, decreasing the wire radius increases the accuracy of the Floating Point Method.

With regards to the non-idealizations , it is reported in [26] that the filament is not uniformly biased. There is a distribution of voltages along it, since a voltage drop is required to make the current flow. A simple solution would be to approximate the effective bias to that of the point at a higher temperature. The whole thread suffers the same heat exchange by radiation, but the end sides of the filament are slightly cooled down by conduction by the shaft elements. Then, the point of higher T_p and therefore the effective bias is placed in the middle. Further accurate development for this section has been developed in [26].

Regarding the **material**, the filament is usually made out of tungsten, which has the higher melting point of all metals (3695 K). It allows the probe to work at a higher temperatures, while still being mechanically stable. Given the similar magnitude of the work function of the metals, a higher melting point imposes an ability to work at higher emission levels than other metals. It is also typical to dope the tungsten with thorium oxide, which was found to increase the order of magnitude of emissivity by 3 [59], reducing the work function of the metal from 4.54 (eV) to 2.63 (eV) [5]. It is worth noting that thorium is an alpha emitter radioactive material and then, it is only harmful if ingested. [26].

It is important to remark here the main disadvantage of the conventional probes, with metallic wires. Despite having high melting points, they have as well larger work functions than other materials. This implies that these EP operate at higher temperatures.

Regarding the **geometry** of the filament, it is affirmed in [33] that in low plasma densities (when space charge effects are larger), a linear filament (Figure 2.12) would obtain more accurate results than a circular one. The author explains that the accuracy increases since the linear design improves the spatial resolution as the thread has significant extent in only dimension. However, it is mentioned that this geometry lasts only for a single use. Unless the wire is given some allowance, the tension on the filament and the deformation done by the heating and cooling processes, will destroy this element.

2.3.2 Connector wires

Regarding the **materials**, the wiring between the circuits and the filaments has been implemented with various elements, such as gold plated nickel [33]. The most used material has been found to be copper due to the ease of finding it. Several authors discuss the necessity to combine both good electric conduction and low thermal expansion properties.

With regards to the **geometry**, the **connection** between these wires and the filament is said to be of great importance. As a result of the difficulty of welding tungsten due to its melting point, some authors used spot welding as in Figure 2.11. This welding process consists in joining two metallic pieces with the heat generated by the electrical resistance of the welded materials. A current is forced by two electrodes through a single point of contact between both pieces, welding them. The intensity and duration of the current is required to match the material properties. Otherwise, if not enough heat is generated, the weld will not be reliable. On the contrary, if too much heat is obtained, the pieces may be damaged, turning them useless [55]. This industrial process may be reliable for long term applications, such as space probes, but its difficulty and the requirement of specific pieces of machinery make it unnecessary for lab tests.

A simple method is to wrap the tips of both filament and connecting wire together to keep good mechanical and electrical contact [59] (Figure 2.10). An even simpler method consists in keeping the physical contact by applying radial pressure. Holes with the same diameter than the filament are machined in the shaft tip, whereas the rest of the shaft length is provided with wider holes for the connector wires. The filament ends are then forced into the narrow holes, while the wires are introduced from the other side of the shaft. It is worth noting that the reliability of this method may be questioned. Nevertheless, it has been found to be particularly useful when the tolerance between the duct in the shaft and the diameter of the connector wires is low, as no wire wrapping can be performed. Its reliability can be enhanced by introducing thin tungsten wires along with the tip in the shaft holes, improving the mechanical fastening as in Figure 2.15 and (Figure 2.14).

2.3.3 Isolating shaft

The **ceramic shaft**, has been found to be usually of alumina (Al_2O_3), which has high electrical insulating properties, a high melting point (2345 K) and a low cost. However, alumina is known to keep trapped gases during its machining process that can damage the probe when exposed to vacuum. This can be solved by outgasing

it in a vacuum before the EP is exposed to a plasma [59]. For further protection and robustness of the probe, the ceramic shaft can be placed inside a casing or a telescopic structure as in Figures 2.11 and 2.13. These structures are commonly made out of tungsten or stainless steel. Eventually, some authors [17] placed a boron nitride tube over the shaft tip to prevent secondary electron emission. This ceramic material seem to be chosen for the tip for its high electrical isolation, excellent heat conduction and high melting point (3246K). The main reason why the whole shaft is not recommended to be made out of boron nitride is it high cost compared to alumina.

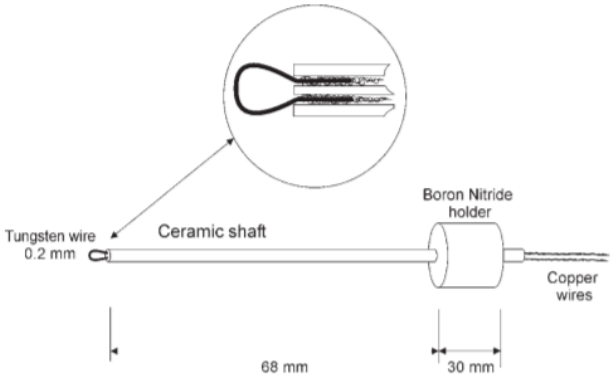

Figure 2.10: Schematic EP set up, reproduced from [57].(Hairpin tip, no casing and wrapped connector wires)

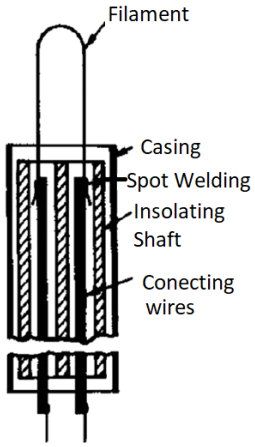

Figure 2.11: Schematic probe set up, reproduced from [59]. (Hairpin tip, casing and spot welded.)

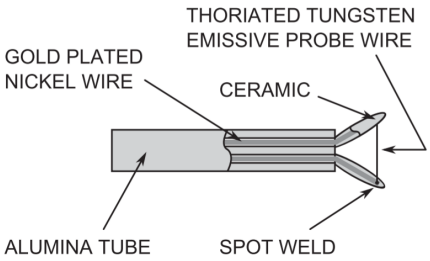

Figure 2.12: Schematic EP shaft, reproduced from [26].(Linear tip, no casing)

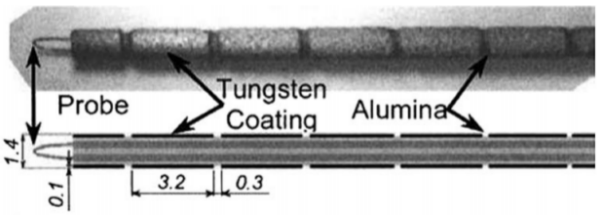

Figure 2.13: Schematic probe set up, reproduced from [59]. (Hairpin tip, supporting coating and connector wires attached by pressure

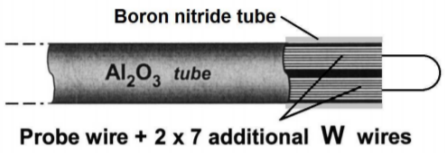

Figure 2.14: EP reproduced from [17] . Hairpin tip and multiple thread connector wires

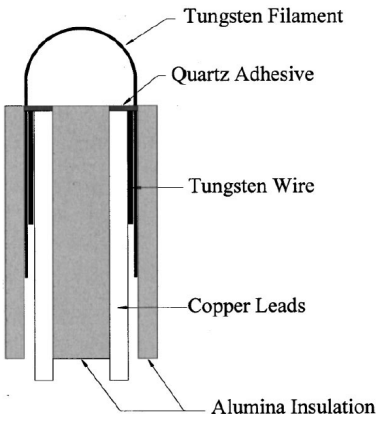

Figure 2.15: Schematic probe set up, reproduced from [21]. (Hairpin tip , casing and pressure connected.)

CHAPTER 3

Conventional Probe Design

3.1 Saturated Emission Temperature

Given that the device operates under the scope of the density of electrons that it can emit, and the required energy to do so, a minimum emission point needs to be established. For that aim, the minimum temperature required by the filament to reach the **plateau area in the Floating Potential Method** (as in Figure 2.7) needs to be described. In [27], Hobbs derived this *Saturated Emission Temperature* (T_{em}) in that method from Poisson Equation, setting that

$$\Gamma = 1 - 8.3 \cdot (\frac{m_e}{m_i})^{\frac{1}{2}} \tag{3.1}$$

Where the electron mass is constant for every element but the ion mass is plasma dependent. Such Γ introduced by Hobbs Law can also be related to the ratio between the emitted electron current and the electron random-thermal current.

$$\Gamma = \frac{I_{em}}{I_e} = \frac{I_{RD}}{I_{th}} = \frac{J_{RD}}{J_{th}} = \frac{\lambda_B(1 - r_{av})A_0 T_{em}^2 exp(\frac{-eW}{k_B T_p})}{eN_\infty \sqrt{\frac{k_B T_e}{2\pi m_e}}} \tag{3.2}$$

I_{RD} and I_{th} definitions in equation 2.6 and Appendix A result in a independence of emissive surface. Hence, it can be concluded that the emission temperature depends only on plasma and emissive material properties and thus, the probe radius does not affect it. Therefore, smaller radius filaments which can be heated with a lower required power but need to reach the same temperature that larger radius filaments, will obtain better performances in fields where the power available is limited .

Equations 3.2 and 3.1 show that the emission probe temperature only depends on the physical properties of both the plasma and the emissive surface material, and can be solved together to obtain the required temperature. With such temperature and a thermal model which depends on design geometries, conventional probes can

be manufactured and operated.

After the *Saturated Emission Temperature* in the Floating Point Method has been defined, two cases can be set: First, a material thermal analysis can be done for "cold temperatures", those which are lower than the saturation. For this temperatures ($T << T_{em}$), if the floating point method is fulfilled, the electron emission should be negligible. Secondly, for high temperatures such that $T \approx T_{em}$ and $T > T_{em}$, the influence of the emitted electron current as a function of temperature needs to be analyzed. Nonetheless, given the emissive material properties dependence found in equations 3.2 and 3.1, the conventional emissive materials need to be depicted .

3.2 Resistivity Temperature Relation

As far as it concerns the thermionic emission, it can be observed in equation 3.2 that the main emissive material properties involved in the mechanism, are its work function (W) and its Generalized Richardson Constant (A_G), which involves the material band structure (λ_B) and the average quantum mechanical reflection coefficient(r_{av}).

Since the whole plasma-solid interaction depends on both their temperatures, the thermo-electrical properties of the filament material shall be analyzed in order to tune the probe design parameters. As Jules Heating will be used to provide thermal energy to the emissive material, the resistivity of tungsten will be a parameter of high importance regarding the power required to operate it. The higher resistivity, the greater heating power can the heater circuit provide with the same current I_h.

$$q_{heat} = I_h^2 \cdot R_{filament} = I_h^2 \frac{L}{\pi r_p^2} \cdot \rho_m \tag{3.3}$$

The electrical resistivity $\rho_m(\Omega \cdot m)$ plays a crucial role in the heat transfer problem desired, as it quantifies the magnitude related to the ability of a material to oppose an electric current. Moreover, the resistivity holds a temperature dependence. For solid conductor materials, while increasing the temperature, the electrons vibrate with greater amplitudes, which makes them collide more often with the metal ions. This extracts some energy from the delocalized electrons in the lattice structure, and reduces their drift speed [1]. Hence, it reduces the velocity of the flow of electrons along the material. This reduction on transmitted current is the result of an increase in the electrical resistivity.

So far, it has not been possible to develop an analytical expression for the resistivity of solid state tungsten as a function of temperature [64]. Consequently, the

[1]Being the drift speed the average velocity of an electron though the material due to an electric field

analysis performed nowadays are based on extrapolations of experimental data. In 1984, P.D. Desai carried out an analysis of the experimental data-sheets available at the time for the tungsten resistivity [12]. The Desai polynomial fit for a wide temperature range yields,

$$\frac{\rho_t}{10^{-8}} = \begin{cases} 0.000015 + 7 \cdot 10^{-7}T^2 + 5.2 \cdot 10^{-10}T^5 & \text{for} \quad 1 \leq T(K) < 40 \\ 0.14407 - 1.16651 \cdot 10^{-2}T + 2.4137 \cdot 10^{-4}T^2 - & \\ \qquad -3.66335 \cdot 10^{-9}T^4 & \text{for} \quad 40 \leq T(K) \leq 90 \\ -1.06871 + 2.06884 \cdot 10^{-2}T + 1.27971 \cdot 10^{-6}T^2 + & \\ \qquad +8.53101 \cdot 10^{-9}T^3 + 5.14195 \cdot 10^{-12}T^4 & \text{for} \quad 90 < T(K) \leq 750 \\ -1.72573 + 2.14350 \cdot 10^{-2}T + 5.74811 \cdot 10^{-6}T^2 + & \\ \qquad +1.13698 \cdot 10^{-9}T^3 + 1.11670 \cdot 10^{-12}T^4 & \text{for} \quad 750 < T(K) \leq 3500 \end{cases} \tag{3.4}$$

Note that this was performed on purpose in such way to be a continuous function. Besides, it was stated by Desai that all data fitted was experimentally performed with mono-crystalline specimens. Because of tungsten atomic structure, it was expected to obtain similar results with polycrystalline specimens, and thus the differences were disregarded. White and Minges updated the function on the higher temperature range, from 750 K to 3600 K [47], and the addition of a thermal expansion resulted in,

$$\frac{\rho_t}{10^{-8}} = -0.968 + 1.9274 \cdot 10^{-2} \cdot T + 7.8260 \cdot 10^{-6} \cdot T^2 - 1.8517 \cdot 10^{-9} \cdot T^3 + 2.0790 \cdot 10^{-13} \cdot T^4 \tag{3.5}$$

This fit is known to have a uncertainty of 0.6% deviation and will be used to characterize the tungsten used to manufacture the conventional emissive probes. Thoriated tungsten is assumed to have an approximate resistivity 4 % higher than solid state tungsten [54], s the same curve will be applied, along with the 4 % correction factor . Other material properties used regarding the design and manufacture are as follows.

	Tungsten	**Thoriated Tungsten**
Composition	$\approx 100\%\ W$	$\approx 98\%\ W + 2\%\ ThO_2$
W [eV]	4.54	2.63
Density $[\frac{g}{cm^3}]$	19.3	18.872
Melting Point [K]	>3696	>3666
ρ_0 $[\Omega \cdot \text{m}]$	$5.642 \cdot 10^{-8}$	$5.425 \cdot 10^{-8}$
Emissivity factor ϵ	0.032 - 0.35	≈ 0.2

Table 3.1: General Properties of tungsten and thoriated tungsten obtained from [54], [20] and [28], at T = 293 K; p = 1 atm.

The only emissive material parameters influencing the emission temperature in equation 3.2 are the work function (W) and the generalized Richardson constant (A_G).

$$\Gamma = 1 - 8.3 \cdot (\frac{m_e}{m_i})^{\frac{1}{2}} = \frac{\lambda_B(1 - r_{av})A_0 T_p^2 exp(\frac{-eW}{k_B T_p})}{eN_\infty \sqrt{\frac{k_B T_e}{2\pi m_e}}} \tag{3.6}$$

$$A_G = \lambda_B(1 - r_{av})A_0 \tag{3.7}$$

Let us consider A_G, which is material dependent, to be constant for a set of materials with similar work functions. In such case, it could be observed the influence of the work function on the emission temperature.

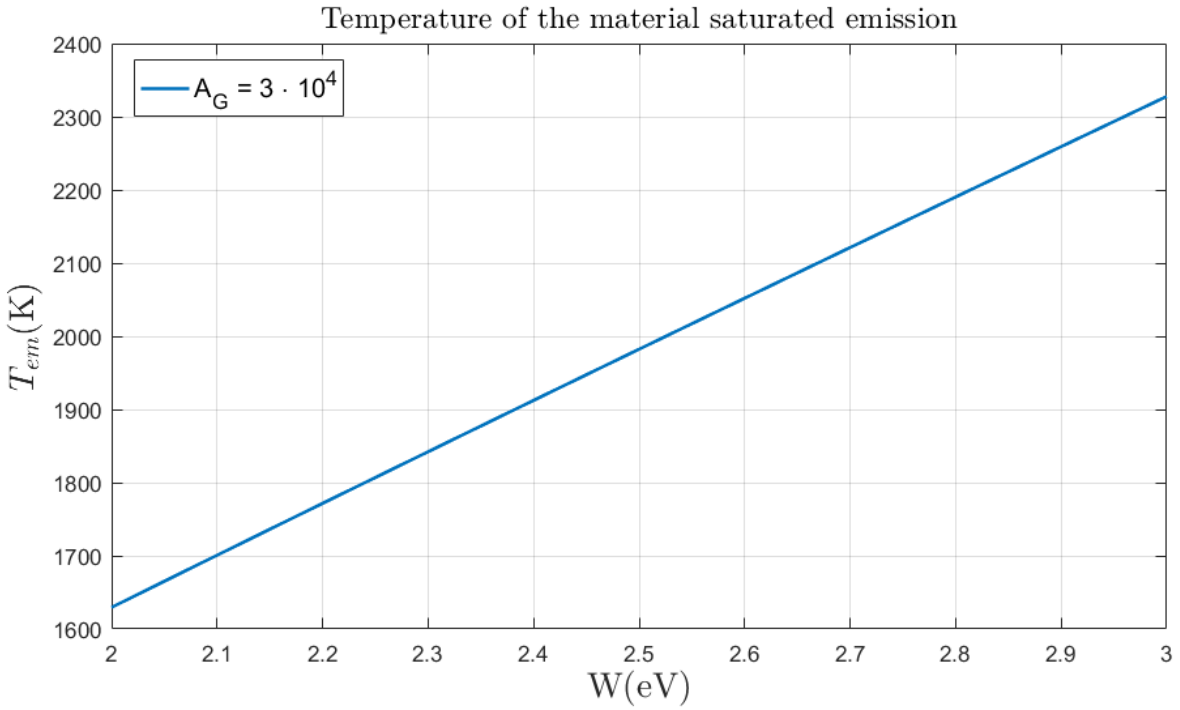

Figure 3.1: T_{em} for materials with different work functions assuming constant *generalized Richardson constant*

This rough simplification corroborates the own definition of work function. The lower work function, the lower temperature required to emit material surface electrons. In reality A_G is not equal for materials with similar work functions, but is preserved within the same order of magnitude as seen in Table 3.2. Thus, the search for non-conventional materials that can emit at lower temperatures and are mechanically stable at them, is well founded. As mentioned in Section 2.3, this line of thought is usually followed by doping tungsten threads with thorium, in order to reduce its work function but keeping a similar generalized Richardson constant. When a layer of thorium oxide (ThO_2) is absorbed by the metal surface, the work function is reduced because of the surface dipole [28].

	Tungsten	**Thoriated Tungsten**
W [eV]	4.54	2.63
A_G $[\frac{A}{m^2 \cdot K^2}]$	$8 \cdot 10^4$	$3 \cdot 10^4$

Table 3.2: Tungsten and thoriated tungsten filaments thermionic properties [20]

3.3 Thermal Model at Negligible Emission

The goal of this first thermal analysis is to roughly set beforehand the requirements for the experimental setup. Regarding the **heating system**, the simplest method described in [26] is the **Joules Heating**. It consists in running a current through the filament, until it reaches the desired temperature T_p.

Joule–Lenz Law defines the heating power generated by an electrical conductor as a function of the resistance and the current (eq. 3.9). On the other hand, given that the filament is placed in a vacuum, the thermal energy is firstly, before any further analysis, assumed to be transmitted by radiation . Then, the radiative power generated in a filament inside a vacuum in absence of plasma, may be approximated to the filament heating power (equation 3.10). Actually, this ideal energy balance needs to be particularized for each probe design in order to take into account other sources of energy variation such as conduction, convection and the kinetic energy loss due to electron emission at high temperatures. The energy loss due to emitted current will be added in the next section, after a deep analysis for the experimental probes analysis, when the presence of plasma is taken into account at temperatures close to the saturated emission in the Floating Point Method. Applying this simplification to the heat diffusion equation at the steady state, in vacuum and without plasma, it yields:

$$\sum q_{system} = q_{heating} - q_{radiative} = 0 \tag{3.8}$$

$$q_{heating} = I_p^2 \cdot R \qquad ; \qquad q_{radiative} = S_p \epsilon \sigma T_p^4 \tag{3.9}$$

$$I_p^2 \cdot R = S_p \epsilon \sigma T_p^4 = 2\pi r_p L \epsilon \sigma T_p^4 \tag{3.10}$$

Where R is the filament resistance, σ is the Stefan–Boltzmann constant and ϵ is the filament emissivity factor. In equation 3.10, it can be observed that the temperature is directly related to the electrical resistance. For a fixed current, the higher resistance, the higher temperature the filament will get.

The filament resistance (R) is related with the material resistivity (ρ) as follows,

$$R(T) = \rho(T_p)\frac{L}{A_p} \tag{3.11}$$

Where L is the length of the filament and A_p its cross section. It is clear that reducing the filament radius, the resistance and therefore the temperature will increase. This relation is not linear as the resistivity of the tungsten is known to depend on temperature [64] as well and has been fitted as a polynomial function. That feature and its importance will be further characterized in the following section.

In order to clarify such filament radius influence on the required heating power circuit, and to pre-analyze the heating system required for the shake of the desired experimental prototype, several simplified cases can modeled. For this matter, material properties that resemble the ones expected during the posterior experimentation, and a filament length of 5 mm, have been assumed.

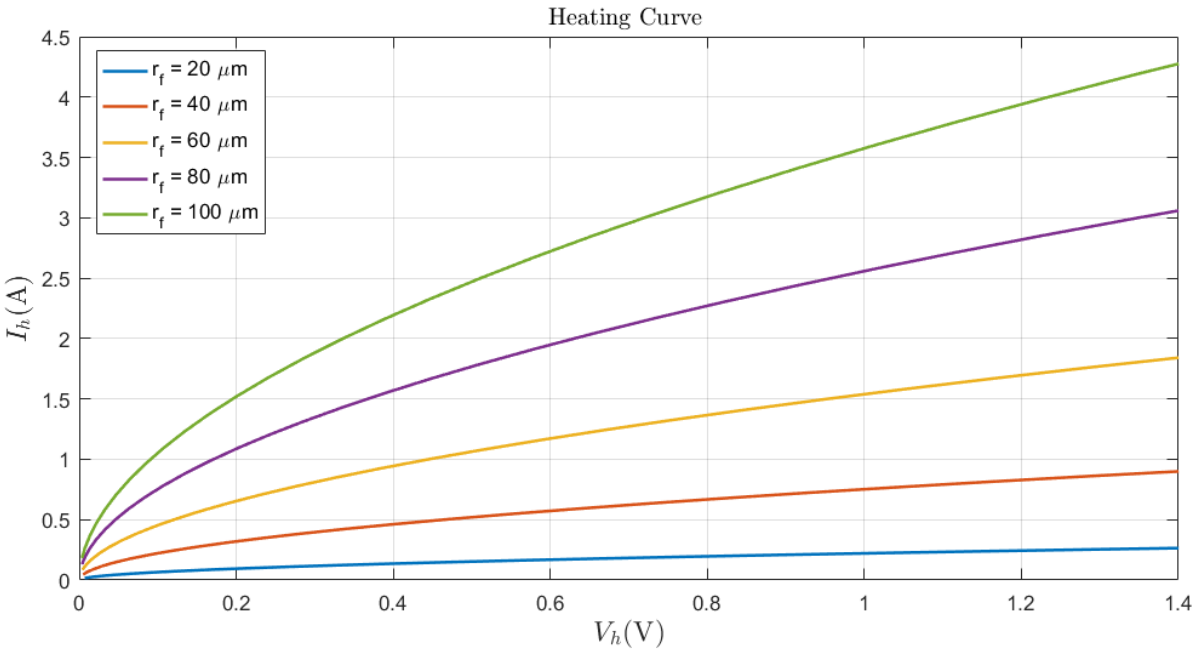

Figure 3.2: Idealized Current - Voltage curve of the filament heating circuit at negligible probe emission

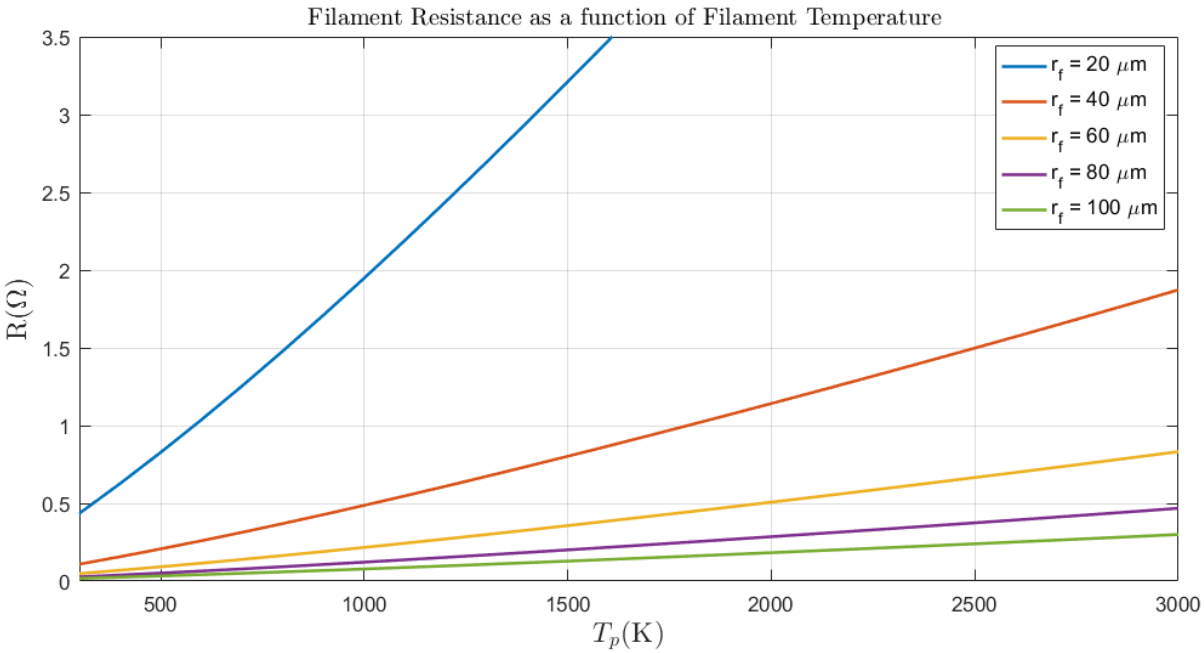

Figure 3.3: Thoriated tungsten filament resistance as a function of the filament temperature

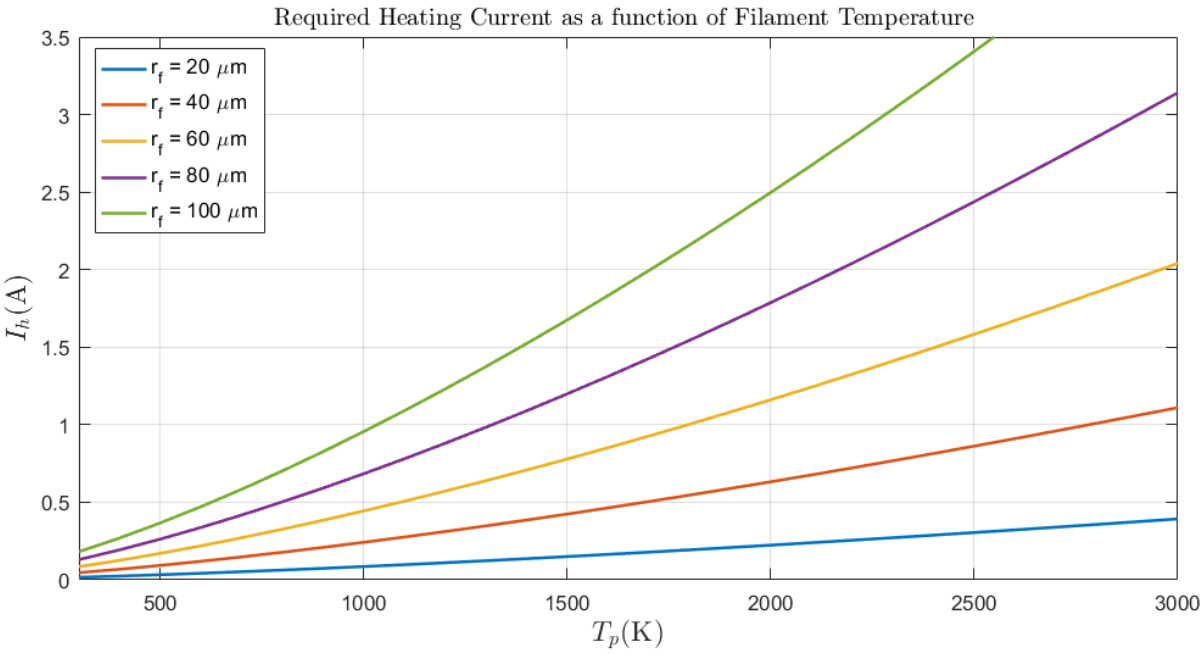

Figure 3.4: Idealized heating current required to reach T_p at negligible probe emission.

Note that Figure 3.2 represents the ideal probe heating response with no electron exchange among plasma and emissive material. It is important not to mistake this $I_h - V_h$ (Heating current vs Heating voltage) circuit response with the characteristic I-V curve of the already hot probe in the presence of plasma such as in Figure 2.3. Moreover, the behavior of the tungsten filament electrical resistance given in Figure 3.3 imposes a non-linearity on the required heating current (I_h) to to increase T_p. Note in Figure 3.3 that the resistivity is nof affected by electron emission and only depends on temperature. Then, this law should be fulfilled in all situations.
In spite of the variety of assumptions an simplifications of this first heating model, these parameters will help to perform a probe sizing before entering into a more detailed thermal analysis. These orders of magnitude will help designing such system dimensions that the filament material can reach the emission temperature provided by a finite and an available power source. It can be assumed that this model will be valid for probe temperatures lower than the saturated emission temperature depicted in Section 3.1

3.4 Thermal Model at High Emission

After the first design sizing performed in Section 3.3, a heat model of the electric circuit needs to be set, in order to be able to operate the probes experimentally. Such model is also required to set the probes operational point in terms of heating

power supplied and filament temperature. The final goal of this analysis is to be able to perform **fast emissive probes scanning** so that the floating potential curve is not measured, only the floating points at the limit of large emissions.

3.4.1 Operational range

Firstly, recalling the theory review, equations 3.2 and 3.1 can be used to obtain the saturated emission temperature, knowing that the elements involved are thoriated tungsten and argon plasma.

$$\Gamma = \frac{\lambda_B(1-r_{av})A_0T_p^2 exp(\frac{-eW}{k_BT_p})}{eN_\infty\sqrt{\frac{k_BT_e}{2\pi m_e}}} = 1 - 8.3 \cdot (\frac{m_e}{m_i})^{\frac{1}{2}} \tag{3.12}$$

The helicon thruster used in the experiment for plasma generation can operate at different argon mass flows, so plasma parameters can be varied (T_e and N_∞). In addition, thruster performance is influenced by a vast number of parameters and experimental disturbances, such as heating of the thruster coil over time. Hence, each time the thruster is ignited, plasma density and plasma electron temperature can be subjected to both large intentional and small non-intentional changes. For that, the heating circuit should be capable to work at different operational points. Varying those parameters on equation 3.12 with the capability range of the helicon thruster, the temperature of emission (T_{em}) that the probes need to be able to reach, in order to get to the saturated floating potential region in Figure 2.7, can be observed.

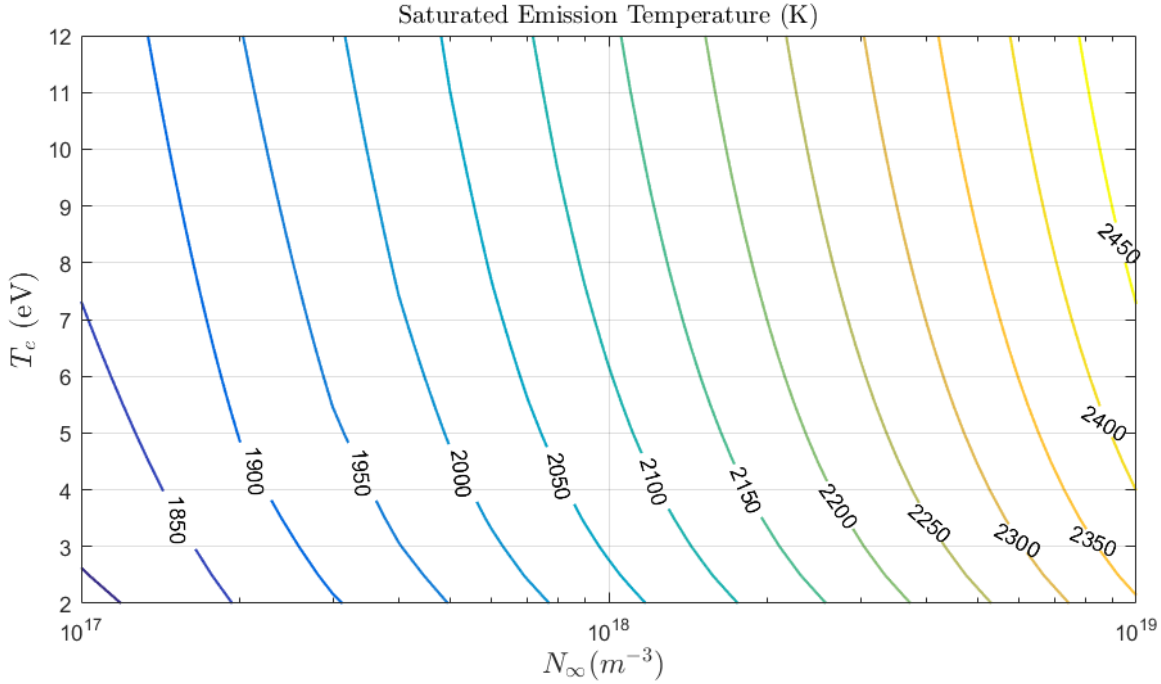

Figure 3.5: V_f saturated knee emission temperature (T_{em}) contour of a thoriated tungsten probe immersed in an argon plasma with T_e and N_∞ properties

3.4.2 Energy Balance

The thermal interaction of the probe with the plasma needs to be reviewed in order to establish a more accurate model of2 each probe operation. It was clearly seen during the first tests of the probes that the energy balance of the system was substantially disturbed at high temperatures in comparison with the heat balance of the probe operation in vacuum. The energy loses due to the geometry of the design, such as heat conduction to the alumina shaft and to the semi-exposed copper wires, is assumed to be constant for both operations in vacuum and in plasma. Therefore, it must be interpreted so that the interaction between the emissive material and the plasma can not be neglected in terms of energy balance.

When it comes to emissive proves in vacuum, it was established in Section 3.3 that the main mechanism of energy loss was the radiative power caused by the glowing filament.

$$q_{rad} = \epsilon \sigma T_p^4 \cdot S_p \tag{3.13}$$

In the presence of plasma, a potential distribution will appear. Such potential will allow electrons from the surface of the filament to reach the plasma under certain circumstances. Let us assume that the probe will be heated from its lowest temperature when it has not been turned on in a period of time. Then, since

$$V_p = V_h = I_h \cdot R_p \tag{3.14}$$

if the heating current is gradually increased from zero for the heating cycle, one can assume that the probe will be biased below the plasma potential $V_p << V_s$. In fact, if this was not the case, the whole idea of an emissive probe will be useless. Consequently, the energy loss to the plasma as a result of the flow of electrons emitted from the probe, needs to be taken into account. The more energy is lost by the heating circuit, the cooler the probe will be. For this, one could expect higher heating currents (I_h) than those resulted in Figure 3.4

The work function was defined as the energy required to rip an electron from a material surface. This would explain an energy loss of the heating circuit to the electrons. That energy is converted into electron kinetic energy so that they can be emitted. Hence, the power loss due to the emissive current will be defined to be the emitted current by the work function of the emissive material. As the operational point of the probe during the heating cycle will be with $V_p << V_s$ until a thermal equilibrium is reached, the emitted current can be assumed to be the Richardson-Dushman thermionic current.

$$q_{em} = I_{em} \cdot W = I_{RD} \cdot W = A_G T_p^2 exp(\frac{-eW}{k_B T_p}) \cdot S_p \cdot W \tag{3.15}$$

Let us define the probe **emissive efficiency** of each device as the energy loss by the emitted electrons, which is the objective of the device, compared to the energy loss by radiation, which is a collateral substantial effect. It can be seen as the ratio between the energy loss that its desired as a design feature, compared to the rest of power losses in the energy balance, which do not contribute to the goal of the probe. By this definition, equations 3.13 and 3.15 can be compared to check the temperature influence.

$$\eta_{em} = \frac{q_{em}}{q_{rad}} = \frac{A_G exp(\frac{-eW}{k_B T_p}) \cdot W}{\epsilon \sigma T_p^2} \tag{3.16}$$

Notice that it is not dependent of filament geometry, just on its temperature and material properties. For thoriated tungsten it yields the following.

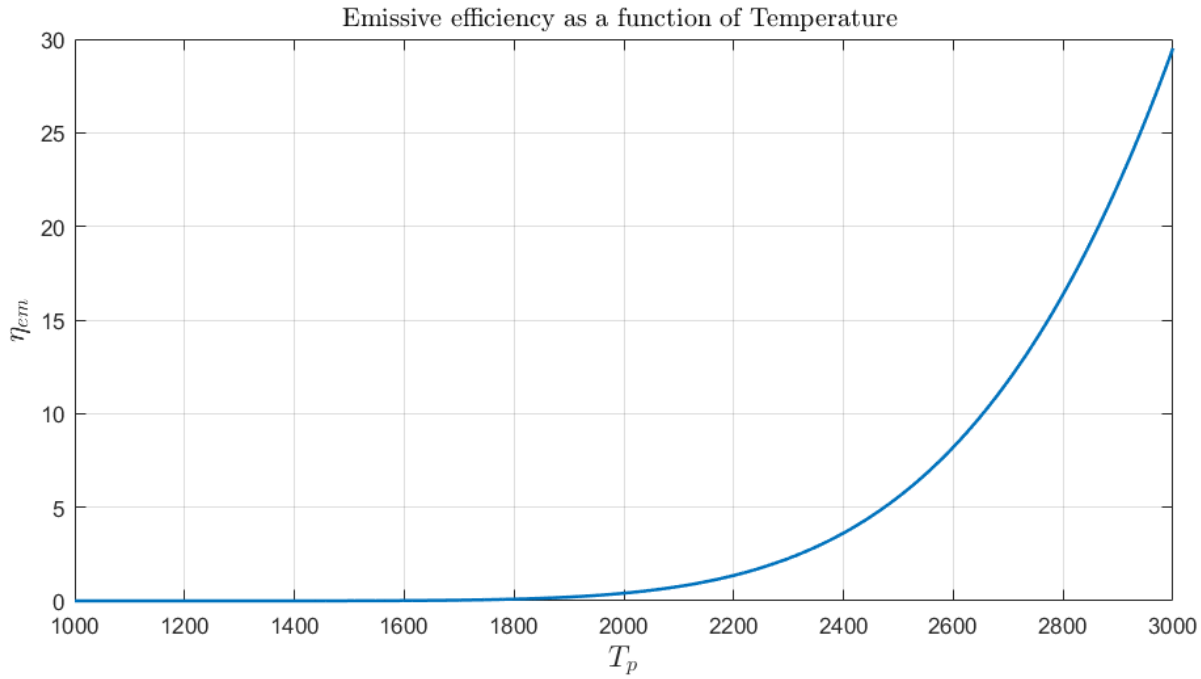

Figure 3.6: Emissive efficiency of a thoriated tungsten filament for a wide operational temperature range

From the previous figure, it can be then concluded that the emissive power loss can not be neglected as temperature increases. The expected operational temperature range for emission saturation observed in Figure 3.9 is seen to be a critical range. Within this range, the power loss due to electron emission goes from almost negligible at 1600 K to several times the power loss by radiation, as seen in Figure 3.7

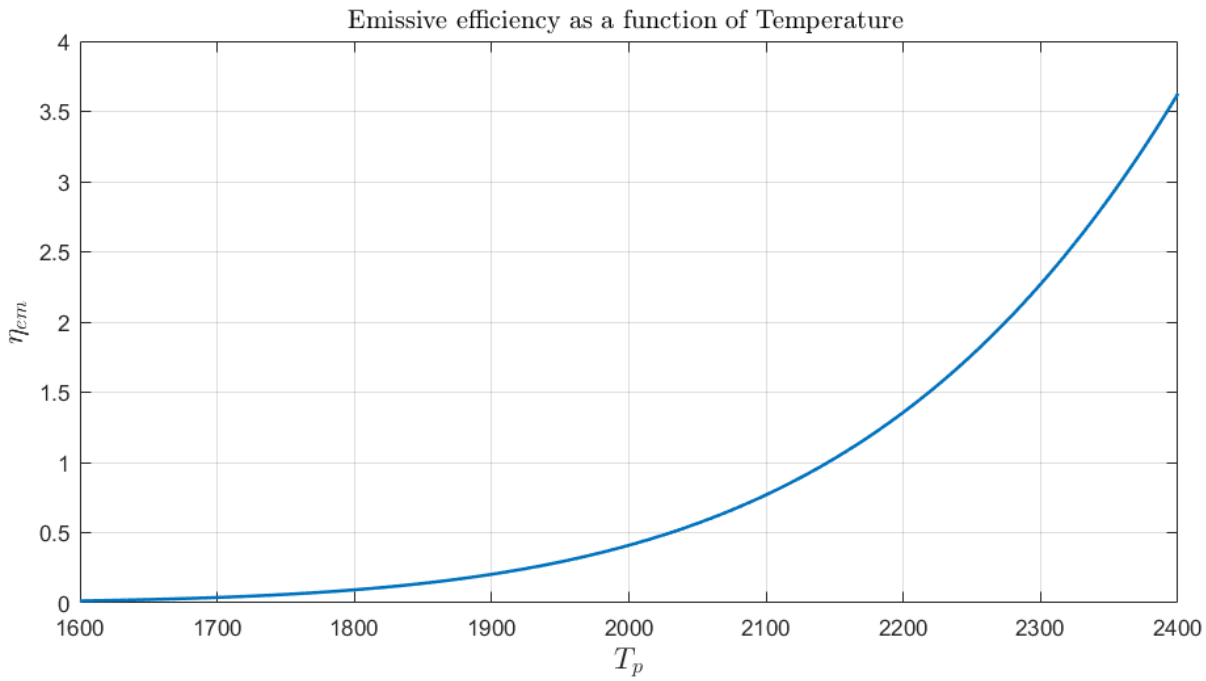

Figure 3.7: Emissive efficiency of a thoriated tungsten filament on the expected operational temperature range

It can be concluded that the electron emission must be taken into account when performing the balance of the heating mechanism, in order to be able to operate it accurately in the laboratory. Finally, if the process is assumed to be steady and adiabatic, so that the probe is shielded by the sheath and no convection between the tungsten and the argon occurs, the energy balance yields

$$q_{heat} - q_{rad} - q_{em} = 0 \tag{3.17}$$

$$I^2 \cdot R = S_p \epsilon \sigma T_p^4 + I_{em} \cdot W \tag{3.18}$$

Once again, if the probe is assumed to be biased below the plasma potential during heating operation, the final **energy balance** of the model can be depicted as

$$I^2 \cdot R = S_p \epsilon \sigma T_p^4 + A_G T_p^2 exp(\frac{-eW}{k_B T_p}) \cdot S_p \cdot W \tag{3.19}$$

Where R is the total resistance of the probe and the heating circuit connections and wires.

$$R = R_p + R_{circuit} = \frac{l}{\pi r_p^2} \cdot \rho_t(T) + R_{circuit} \tag{3.20}$$

Then, the power equation for the heating mechanism yields,

$$I^2 \cdot (\frac{l}{\pi r_p^2} \cdot \rho_t(T) + R_{circuit}) = S_p \epsilon \sigma T_p^4 + A_G T_p^2 exp(\frac{-eW}{k_B T_p}) \cdot S_p \cdot W \tag{3.21}$$

3.4.3 Probe Heating Mechanism

Given the fact that the saturated emission temperature for the filament immersed in different argon plasma conditions is known and the energy balance of the probe has been defined in equation 3.21, the required heating current (I_h) of each probe can be obtained. This current will depend on the filament radius, but also on the plasma properties as $T_{em} = f(T_e, N_\infty)$. Then, for different plasma conditions, the heating current required for each probe to reach the saturated floating potential emission temperature can be obtained. Note that the resistance of the heating circuit of each probe has been taken into account after being measured experimentally as follows. Note that the circuit wiring is not equal for both probes as they use different feed through wires inside the vacuum chamber.

Probe	r_p **(m)**	R_p **at 273K** (Ω)	$R_{circuit}$ (Ω)
I	$5{\cdot}10^{-5}$	0.156	0.494
II	$1.25{\cdot}10^{-5}$	2.97	0.9

Table 3.3: Circuit resistance of each probe manufactured.

Probe I ($r_p = 5 \cdot 10^{-5} m$)

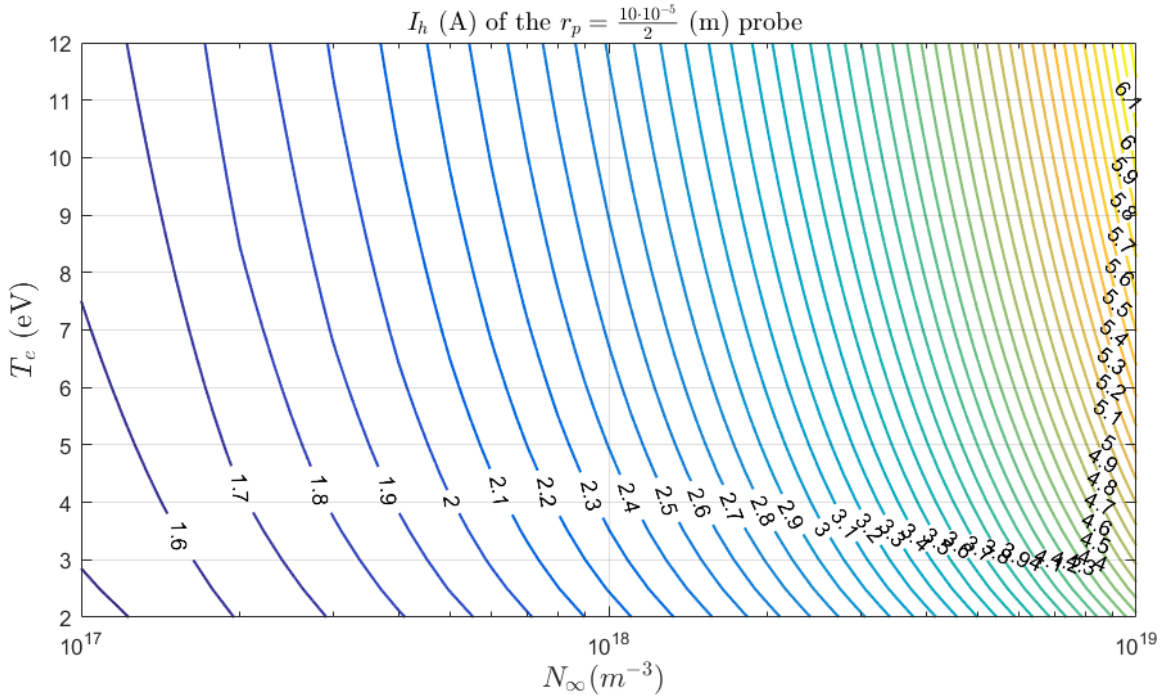

Figure 3.8: Heating current contour of a thoriated tungsten probe with $r_p = 5 \cdot 10^{-5} m$, immersed in an argon plasma with T_e and N_∞ properties

Probe II ($r_p = 1.25 \cdot 10^{-5} m$)

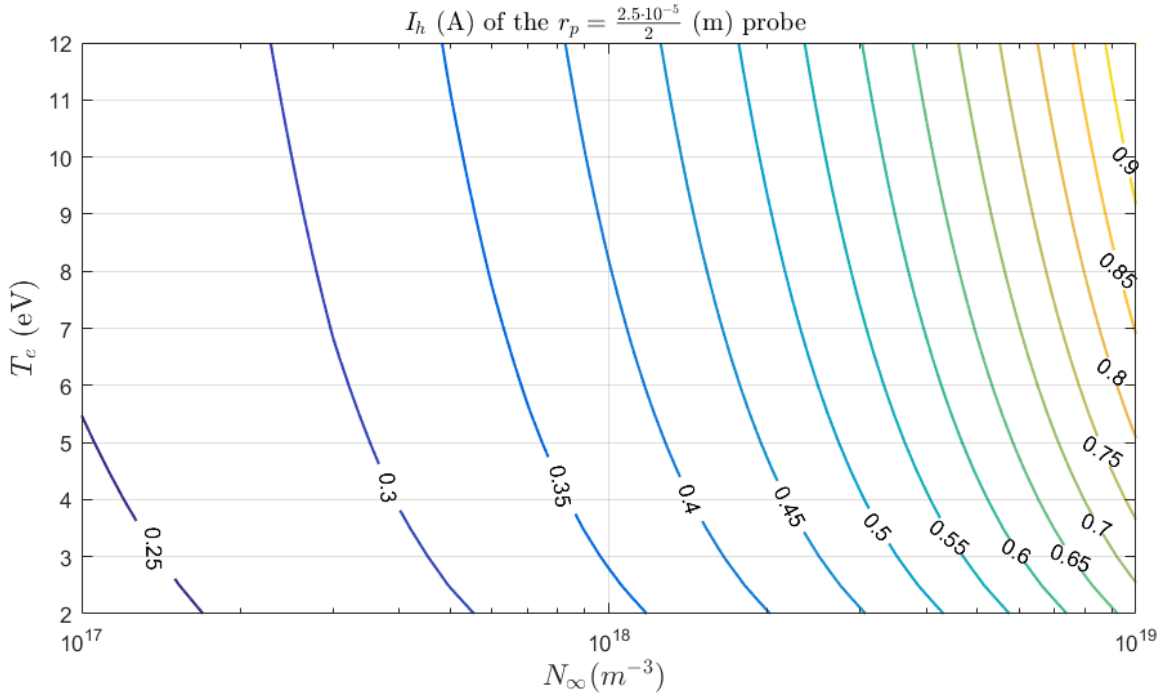

Figure 3.9: Heating current contour of a thoriated tungsten probe with $r_p = 1.25 \cdot 10^{-5} m$, immersed in an argon plasma with T_e and N_∞ properties

Finally, an approximate known plasma condition at which the probes will be operated can be analyzed. At such condition, the thruster is expected to generate an argon plasma with the following properties.

Electron temperature, T_e **[eV]**	**Plasma density** N_∞ $[m^{-3}]$
4	10^8

Table 3.4: Approximate plasma experimental condition, similar to those at which the probe will be initially tested

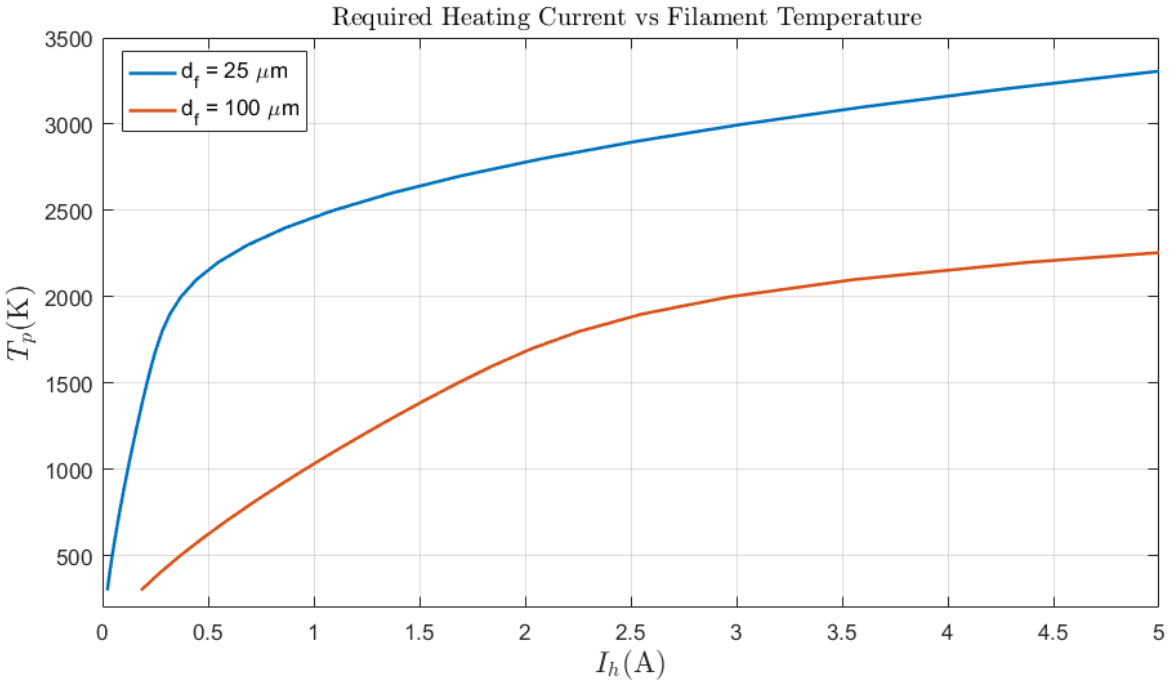

Figure 3.10: Required heating current of both probes immersed in an argon plasma with T_e and N_∞ properties as in Table 3.4

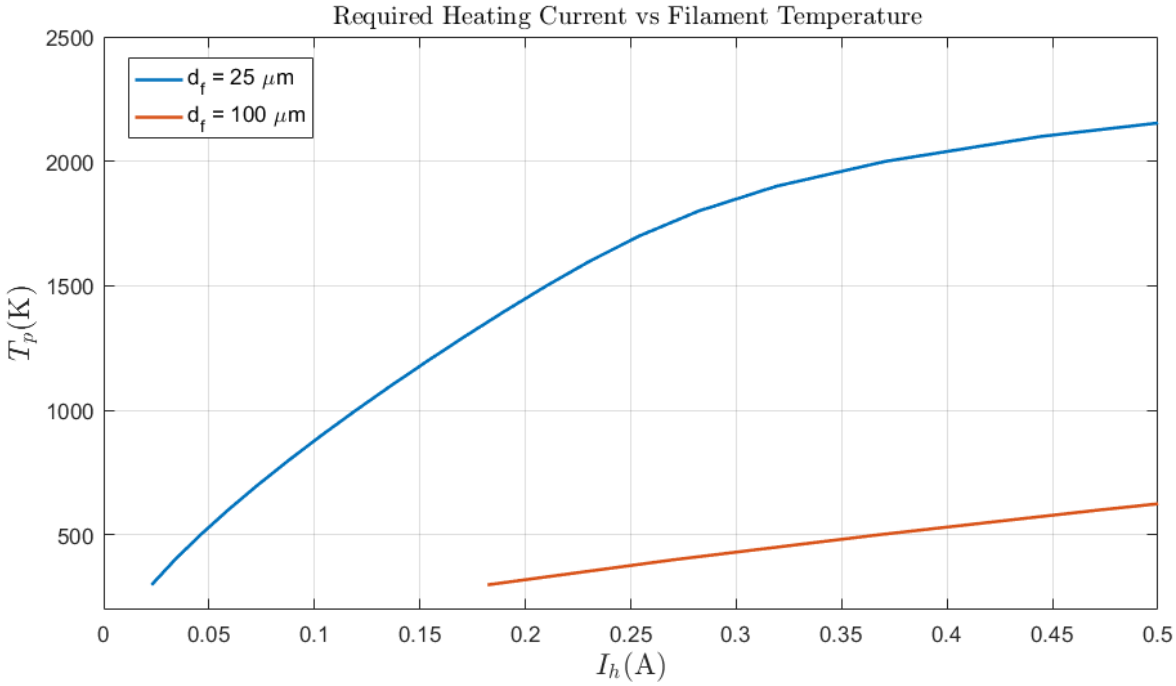

Figure 3.11: Required heating current of both probes immersed in an argon plasma with T_e and N_∞ properties as in Table 3.4

Notice in Figure 3.10 how the slope of the curve is suddenly decreased at high temperatures. This is due to the contribution of the emitted current power loss

analyzed in Figure 3.7. At about T_{em} (2000K), η_{em} increases abruptly and then the energy balance mainly behaves according to q_{em}. This results in lower temperature increases per heating current raise, when the probe has reached the emission saturation temperature.

$$\left.\frac{dT_p}{dI_h}\right|_{T_p<T_{em}} < \left.\frac{dT_p}{dI_h}\right|_{T_p>T_{em}} \tag{3.22}$$

It can be concluded then that for low probe temperatures ($T_p << T_{em}$), the thermal behavior is dominated by probe material radiation (q_{rad}), whereas for high probe temperatures ($T_p \approx T_{em}$ & $T_p > T_{em}$)), the system thermal equilibrium is dominated by electron emission (q_{em}).

3.5 Design Features and Manufacturing Process

From the literature review in Section 2.3, it was decided to design the probes in the simplest and more time efficient way, since the first goal is to check whether or not the whole emissive probe theoretical concept works.

Regarding the **filament**, a set of 4 tungsten threads with different radius were used (i.e. $50\mu m$, $25\mu m$, $12.5\mu m$ and $6.75\mu m$). For certain difficulties during the first tests, note that only two probe sizes were able to finally be used in plasma, and to achieve useful results. Different filament thicknesses have been used to observe the behavior of the measured floating potentials during different tests, under the same or different conditions. It is discussed that the lower filament radius, the higher accuracy of the Floating Point Method. However, note that thiner probes also hold lower lifespans. In fact, failure due to thermal expansion was observed to increase for smaller filament radius: the $6.75\mu m$ radius filament usually broke during fabrication process by the heat provided by the manufacturers hands.

Probe	r_p **(m)**
I	$5{\cdot}10^{-5}$
II	$1.25{\cdot}10^{-5}$

Table 3.5: Probe filament radius

The geometry of the filament was composed by a semi-circular loop protruding our from an end of the shaft tube. The filament was given some allowance to counteract thermal expansion, in order to avoid a mechanical failure. This geometry was selected over the linear one, for both simplicity and the amount of cycles until failure: it was stated in [33] that linear geometries only last one use, even though they tend

to be more accurate in low density plasmas.

The **isolating shafts** were made out of an alumina tube (⌀ 5 mm) with two symmetrical bores along its cross section, from tip to tip, which was 30 mm. This material was chosen for its low cost, high thermal conduction and good electrical isolation properties. However, note that it is both hard and brittle. This makes it fragile to handle and tough to cut into smaller pieces. The cutting was made with an diamond electric circular saw, with water as coolant to avoid sparks. Impacts on the pieces are recommended to be avoided.

Multi-threated copper **connector wires** were used along the shaft bores. In the probe tip end, each wire was wrapped with a filament end. Multi-threated wires were used in order to improve both the mechanical and electrical contact, as if wrapped correctly, the connection should last. On the other tip of the connector wires, a male pin was welded so that the probe an be able to be plugged in the feed circuit while they are placed inside the vacuum chamber. Thermo-retractile material was used to isolate the remaining copper wire between the male pins and the alumina bore. This material also secured the assembly, preventing the copper wires from sliding inside the shaft bores, so that the filament is fixed.

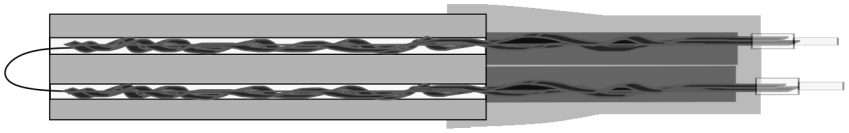

Figure 3.12: Schematic cut view of the manufactured conventional probes

3.6 Expected $I_p - V_p$ Performances

According tho the theoretical emissive probe behavior developed in Chapter 2 and given a known approximate plasma operational point in Table 3.4, the performance of each probe can be analyzed. This would be helpful in order to have an understanding the facts that will occur during experimental testing. Notice that **Space Charge Limited** effects were disregarded in the model and then, for V_p slightly lower than V_s, this idealized total probe current will differ from the real one.

Let us assume the heating circuit has been able to accurately make each probe filament to a desired T_p. Then, making a voltage sweep with a voltage source on the probe from a bias below the plasma potential ($V_p << V_s$) to a bias above

it ($V_p >> V_s$), the different behaviors of emitted and collected current explained in Figure 2.2 and Section 2.1.1 could be seen. Defining the probe current as the addition of the emitted current and the collected current, for a filament at T_p, when planar theory is assumed, the **performance model** yields,

$$I_p = I_e + I_{em} \tag{3.23}$$

$$I_{em} = \begin{cases} -I_{RD} & \text{for} \quad V_p < V_s \\ -I_{RD} \cdot exp(\frac{-e(V_p - V_s)}{k_B T_p}) & \text{for } V_p \geqslant V_s \end{cases} \tag{3.24}$$

$$I_e = \begin{cases} I_{th} \cdot exp(\frac{-e(V_s - V_p)}{k_B T_e}) & \text{for} \quad V_p < V_s \\ I_{th} & \text{for } V_p \geqslant V_s \end{cases} \tag{3.25}$$

$$I_{th} = S_p e N_\infty \sqrt{\frac{k_B T_e}{2\pi m_e}} \qquad I_{RD} = A_G T_p^2 exp(\frac{-eW}{k_B T_p}) \cdot S_p, \tag{3.26}$$

From equations 3.23 through 3.26, the collected and emitted currents can be obtained as a function of the difference between the plasma and the probe potentials ($V_p - V_s$), at a given operational probe temperature.

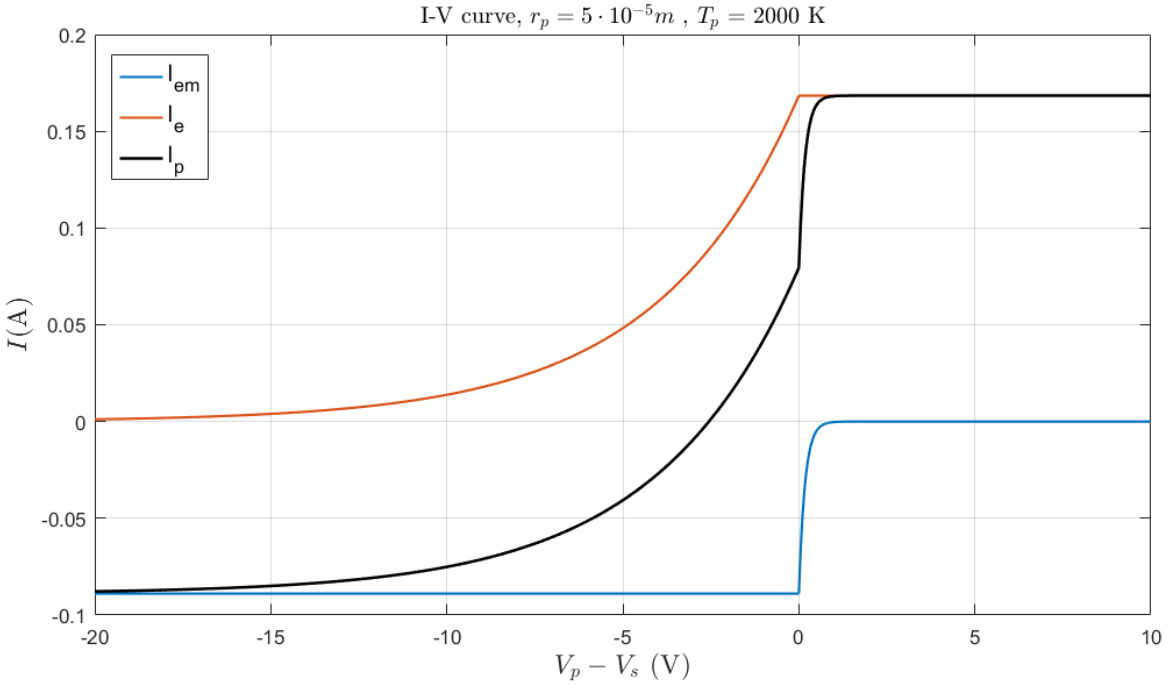

Figure 3.13: I - V_p curve of Probe I ($r_p = 5 \cdot 10^{-5} m$) at 2000 K. Collected current (I_e), Emitted current (I_{em}) and net probe current ($I_p = I_e + I_{em}$). Assumed plasma conditions from Table 3.4

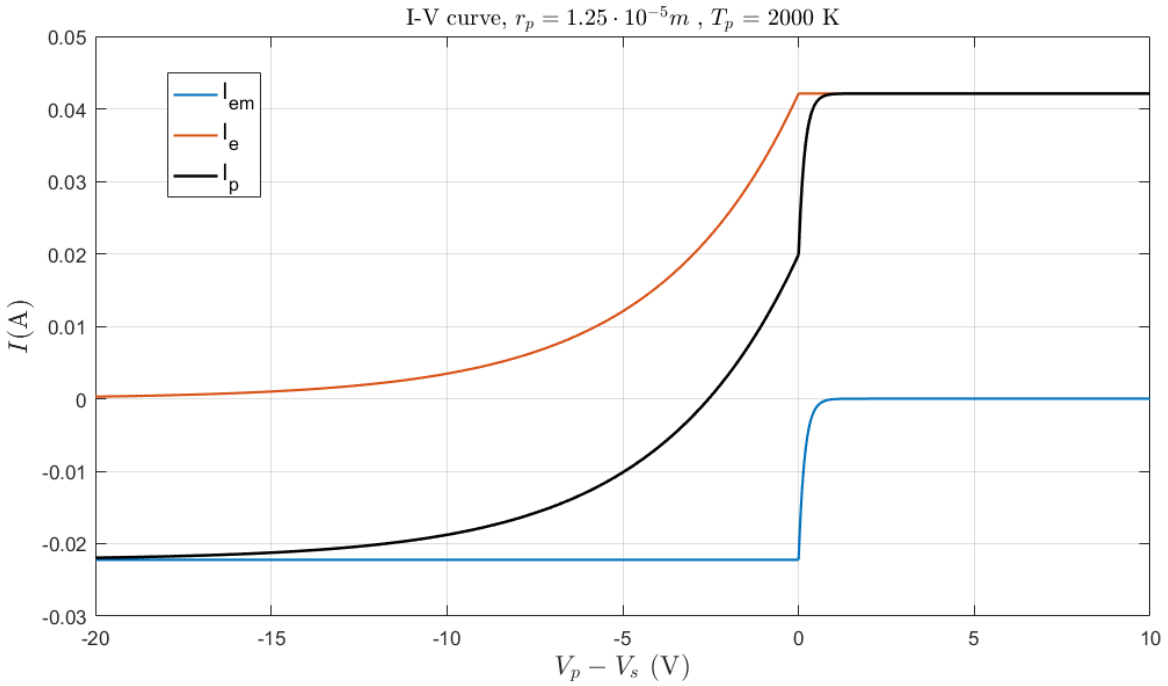

Figure 3.14: I - V_p curve of Probe II ($r_p = 1.25 \cdot 10^{-5} m$) at 2000 K. Collected current (I_e), Emitted current (I_{em}) and net probe current ($I_p = I_e + I_{em}$). Assumed plasma conditions from Table 3.4

Given that the behavior of the $I_p - V$ curve is as predicted from the literature review in Chapter 2, the net current at different temperatures shall be obtained.

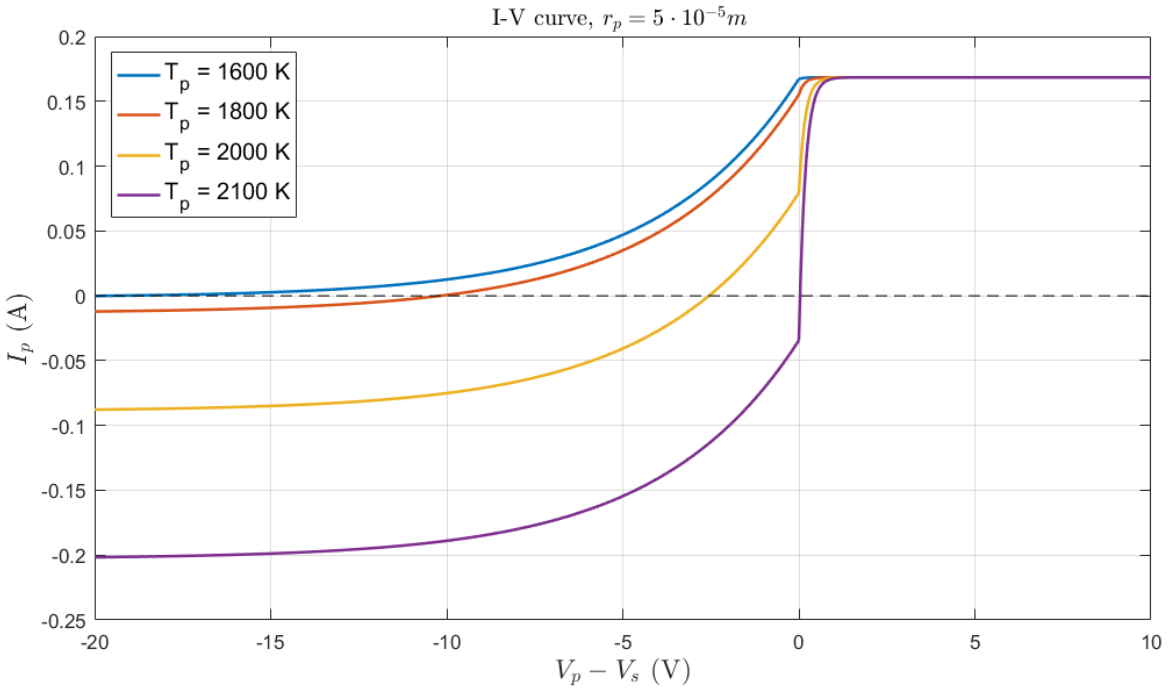

Figure 3.15: I_p - V_p curve of Probe I ($r_p = 5 \cdot 10^{-5} m$) for different operational probe temperatures. Net probe currents. Assumed plasma conditions from Table 3.4

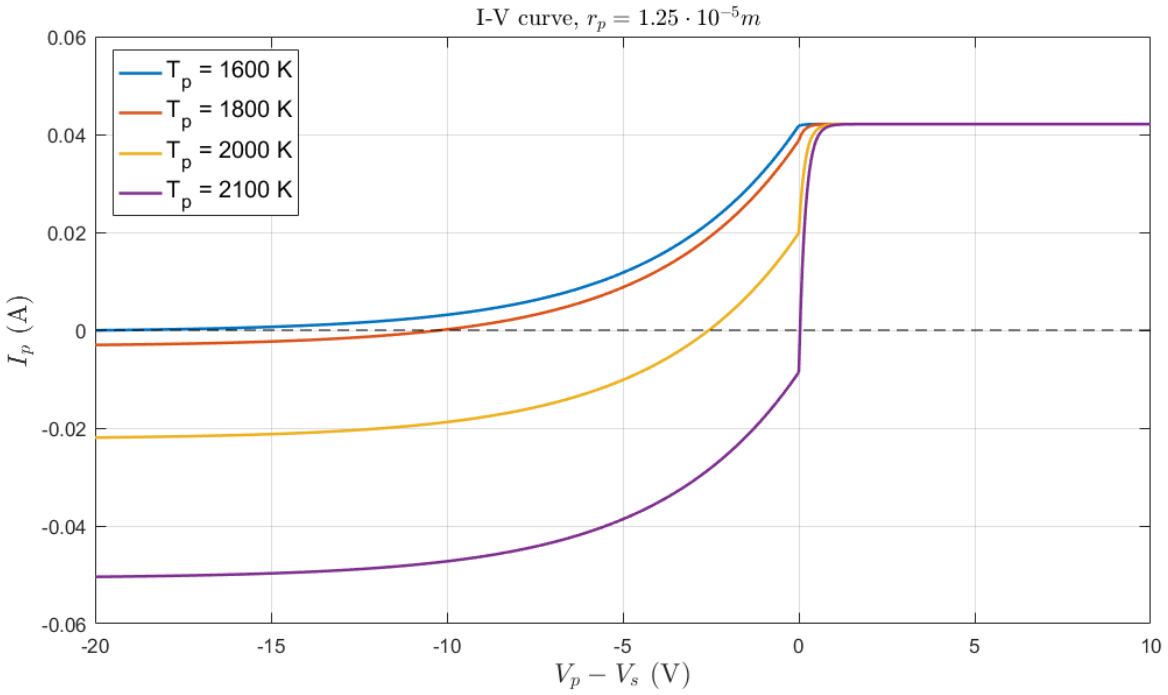

Figure 3.16: I_p - V_p curve of Probe II ($r_p = 1.25 \cdot 10^{-5} m$) for different operational probe temperatures. Net probe currents. Assumed plasma conditions from Table 3.4

From Figures 3.15 and 3.16, it can be seen that the emitted current increases with probe temperature. This,once again, proves the need to add the power loss for the outgoing electrons to the energy balance of the system as in equation 3.21.

Recall that in the models used **Space Charge Limited Effects are not taken into account**. From Hobbs Law in equation 3.1, where these effects are considered, it was set that $|\Gamma| \leqslant 1$. For the assumed plasma conditions it was computed that $T_{em} = 2000K$. Notice in Figures 3.15 and 3.16 that Hobbs Law needs to be fulfilled for $T_p > T_{em}$ (as for instance for the curve of T_p=2100K). This temperature would not fulfill Hobbs Law ($\frac{I_{em}}{I_e} = 1$) if $V_p < V_s$ in equations 3.24 and 3.25, since the magnitude of the Richardson-Dushman emission is larger than the electro-random thermal current. In such case a solution is only found if $V_p > V_s$ and $\Gamma = \frac{I_{RD} \cdot exp(\frac{-e(V_p - V_s)}{k_B T_p})}{I_t h} = 1$. This would mean that the floating potential at the saturated emission temperature found with Hobbs Law, which is the knee of the curve in the Floating Potential Method, corresponds exactly with the plasma potential. This is **not valid** in reality when non-ideal effects are considered, and just shows the limited validity of the equations taken to model the plasma-probe interaction. This also depicts the difficulty to obtain the plasma potential analytically, and the need to experimentally measure it so that non-idealizations are considered.

3.7 Experimental Set Up

With regards to the probes placement, a **stand** was also designed and manufactured. The stand was designed in order to accommodate the probes, while being compatible with the supports already set up inside the chamber. Different emissive probes must not be operated together so that they do not disturb each other. However, a it is a nice feature to place them at the same time and switch between probes. In such case, the thruster can be assumed to be under similar conditions. For that, the stand was designed to hold four emissive probes with the previously described geometry, plus a cold Langmuir probe ($\varnothing$ 11.5 mm), in case some results want to be contrasted with a collecting probe. The probes were secured inside each stand whole by a screw.

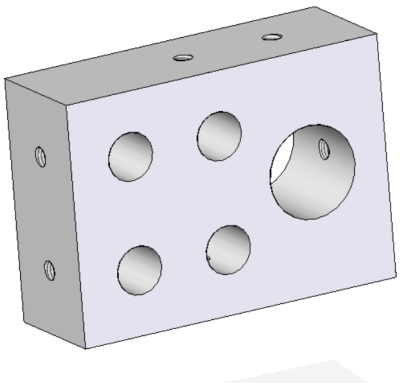

Figure 3.17: Designed probes stand. Detailed blueprints in Appendix B

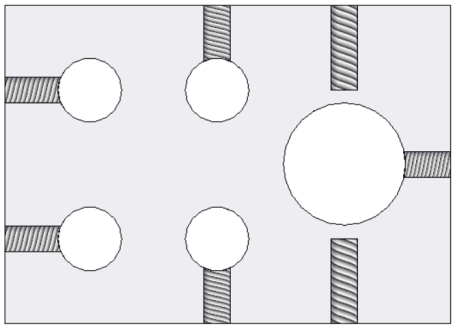

Figure 3.18: Central cut view of the stand. Threaded holes for the tightening M3 screws

The chamber used for the experiments was the *Leybold UNIVEX S XTT* of the *EP2 Space Propulsion and Plasma team* at UC3M, capable of achieving vacuums at pressures as low as 10^{-9} bar. Moreover, in terms of plasma generation, a helicon thruster cable of achieving densities in the range of $[10^{17} - 10^{19}\ m^{-3}]$, and plasma electron temperatures of $[2 - 12$ eV$]$, was used.

The built in support inside the chamber allows azimuthal and radial movements. The probes were fixed to the stand, and the stand was secured to the built-in support. The assembly was placed directly facing the thruster nozzle at 120 mm of radial distance. The thruster central axis was located on the mid point between the 4 EP in the stand by means of a laser pointer, as in Figure 3.23. The position of the Langmuir probe was then off set, given that it was there only for future measurements checks. The back side of the probes assembly was then covered on aluminum tape to protect it from the plasma, avoiding other disturbances as well.

Regarding the heating circuit, a BK precision PVS60085MR programmable power source was directly connected to the probes. This power source was connected with regular wires to pins on the chamber wall. Each pair of pins was connected inside the chamber to a probe by a shielded cable. Such cable consist sin two copper wires, isolated from each other by plastic covering. Those two are then shielded from secondary electron emission by a metallic mesh that covers them both. The shield is covered by another layer of covering which is vacuum rated. Besides, the shield was grounded to the chamber wall.

Once the probe was heated with the power source, a Keithley 6487 was used as a voltmeter to find the floating potential with a software interface. An scheme of the floating circuit used to take measures performing the Floating Potential Technique is displayed in Figure 3.19

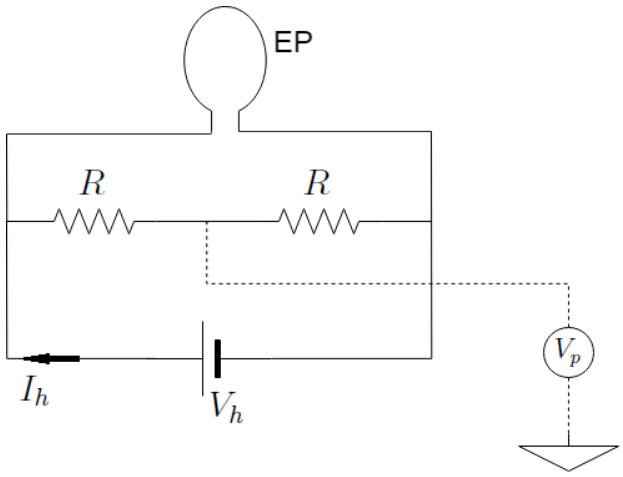

Figure 3.19: Emissive probes floating measuring circuit

In the scheme depicted in Figure 3.19, the power source provides the heating current (I_h) and the heating voltage (V_h). The emissive probe (EP) is forced not to collect or to emit any current in this closed circuit. For this, the circuit needs to be electrically isolated from ground, i.e. floating. The resistances (R) located in the middle division need to be large enough so that the current, I, flowing through this section can be considered negligible. By using two identical resistances, a voltmeter connected to the midsection can be assumed to be measuring the probe floating potential (V_p)

Figure 3.20: Vacuum chamber side I. On the center: sealed feed-through connections for the probe and other inner devices

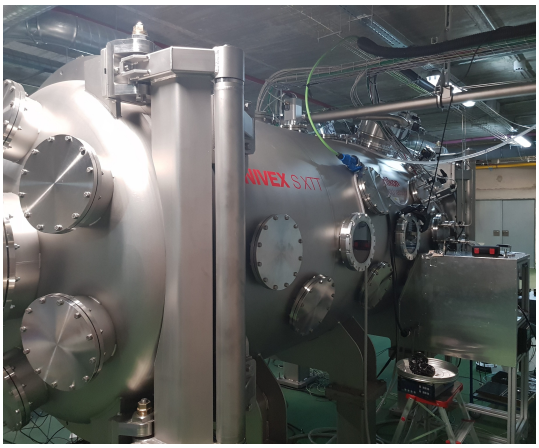

Figure 3.21: Vacuum chamber side II. EP2 facilities at UC3M.

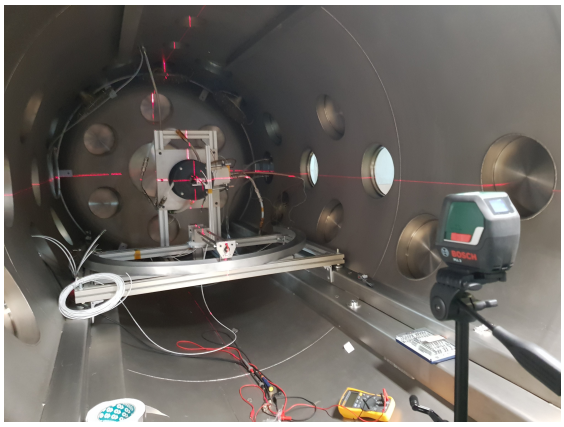

Figure 3.22: Inside of the chamber during set up. On the center: Helicon thruster and probe stand. On the left: shielded white cables connected to the wall feed-through.

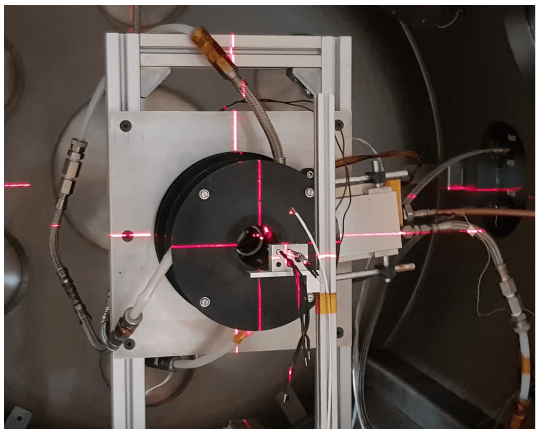

Figure 3.23: Probe assembly positioning, facing the thruster nozzle. Probes not connected to the feed-through cables. Backside of the probes not covered with aluminum tape yet.

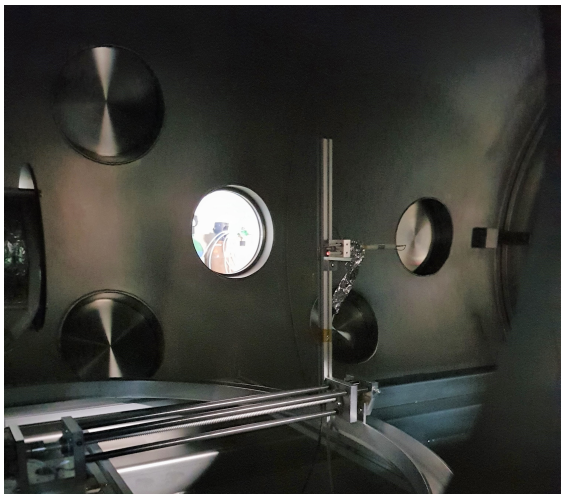

Figure 3.24: Probes assembly facing the thruster. Vacuum without plasma. All EP OFF.

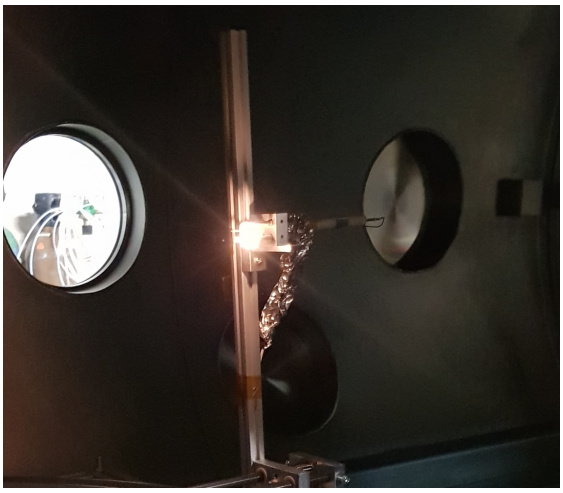

Figure 3.25: Probes assembly facing the thruster. Vacuum without plasma. One EP is ON. Connection cables covered with aluminum tape.

CHAPTER 4

Experimental Results and Discussion

With regards to both manufactured **conventional probes** (Probe I & Probe II) in the presence of plasma, the floating potential is directly measured by the voltmeter used along with the software interface, which takes several V_f for each probe temperature and then averages them, performing an EP scanning. Both current (I_h) and voltage (V_h) of the heating circuit are directly given by the power source interface during probe operation. I_h is limited while V_h is allowed to adapt according to the probe requirements. With them, the resistance of the probe filament is estimated, taking into account the resistance of the cables from the feed-through to the probe pin connectors. These circuit resistances are measured experimentally as in Table 3.3. Then, for each measurement of each probe:

$$\frac{R}{R_0} = \frac{\frac{V_h}{I_h} - R_{circuit}}{R_0} \tag{4.1}$$

where $R_{circuit}$ is different for each probe and $R_{p,0}$ is the probe resistance of each probe, measured at room temperature at the manufacturing process. Then, from the definition of resistance in equation 3.11 and the resistivity law used from equation 3.5, the probe temperature can be estimated.

$$\frac{R}{R_0} = \frac{\rho(T_p)}{\rho_0} \rightarrow T_p = f(\frac{R}{R_0}) \tag{4.2}$$

Note that this temperature is obtained from the resistivity and hence it will change if other law is used. As explained in Section 3.2, thoriated tungsten resistivity is still an issue under discussion. The resistivity law used to determine the probe temperature is given in equation 3.5. The numerical results of this derivations can be found in Appendix C.

From Γ in Hobbs Law in Section 3.4.1, the required temperature to reach the plateau area in the FP Method was observed to be in the order of magnitude of 2000K. Although the information regarding plasma conditions (T_e, N_∞) is only an estimation from previous tests, the order of magnitude of the required heating current of each probe to reach that temperature was correct to be a design guideline, as in Section 3.4.3.

	Probe I	**Probe II**
$r_p\ (m)$	5	1.25
$I_h\ (A)$	1.8	0.22

Table 4.1: Required heating current order of magnitude. Dependent on plasma conditions

During the experimental section, the probe tests will be named after the following nomenclature:

$$Test\_YYYY/MM/DD - HHMM \rightarrow Test\_Year/Month/Day - HourMinute \tag{4.3}$$

4.1 Heating curves in vacuum

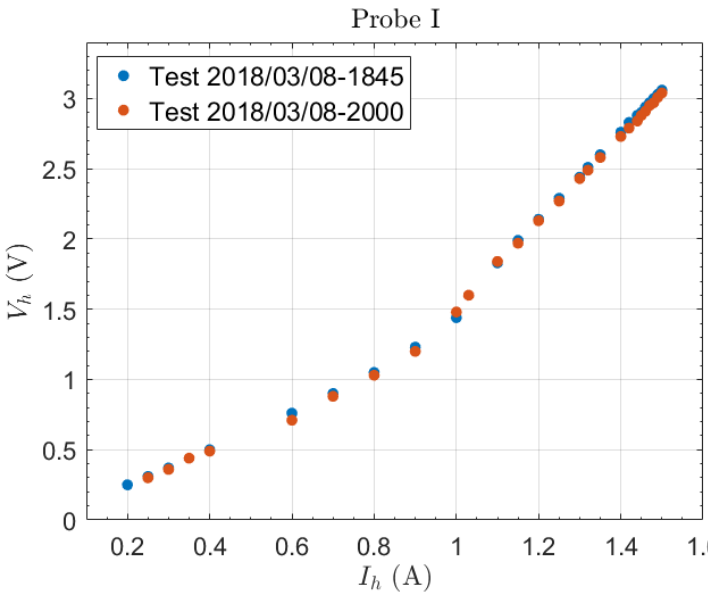

Figure 4.1: Probe I.Experimental I_h-V_h. Vacuum.

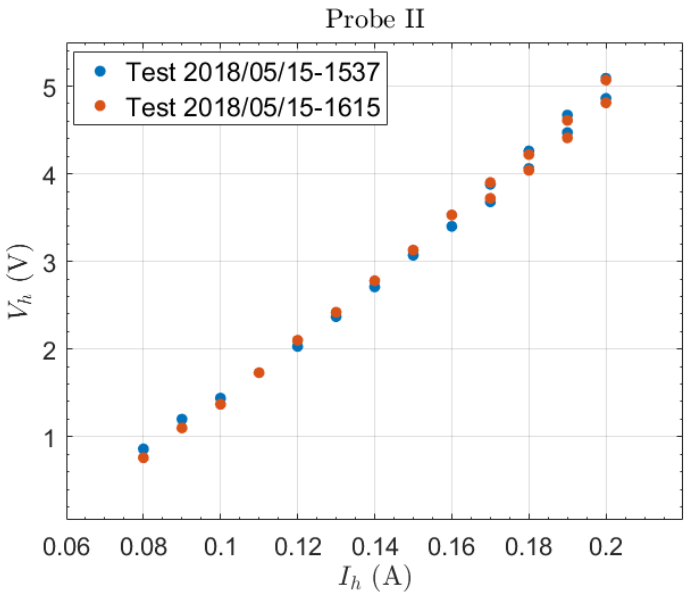

Figure 4.2: Probe II. Experimental I_h-V_h. Vacuum.

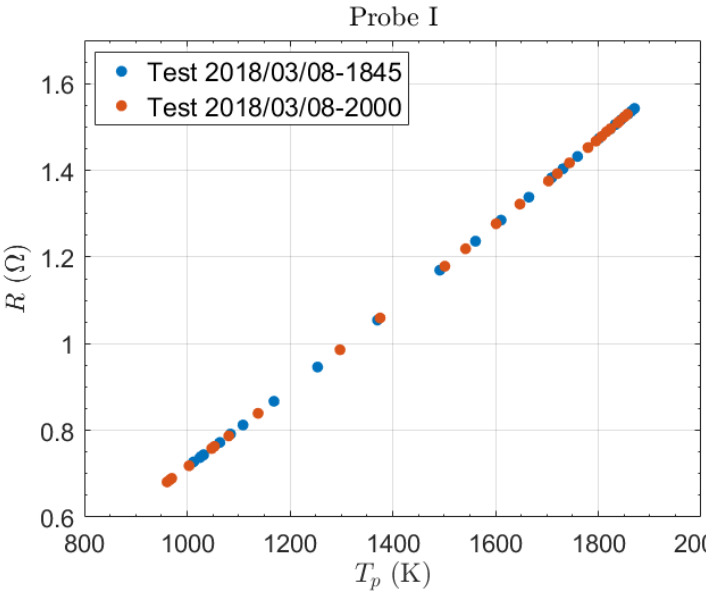

Figure 4.3: Probe I. Experimental T_p-R. Vacuum.

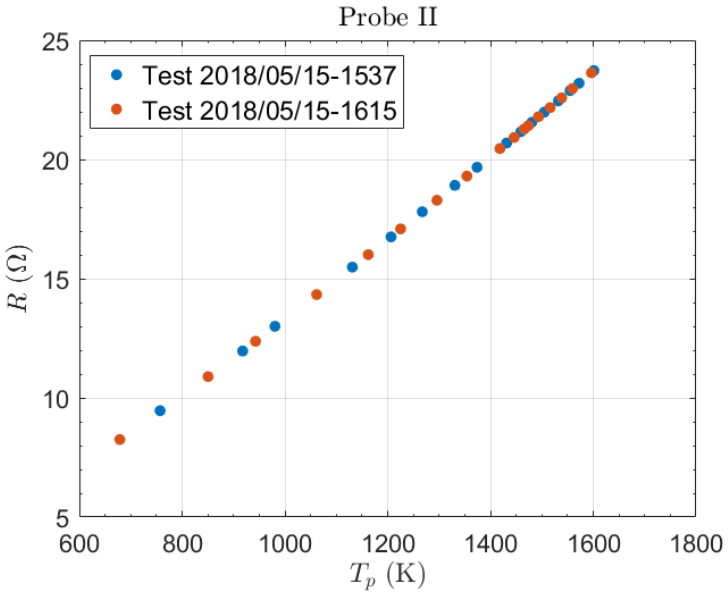

Figure 4.4: Probe II. Experimental T_p-R. Vacuum.

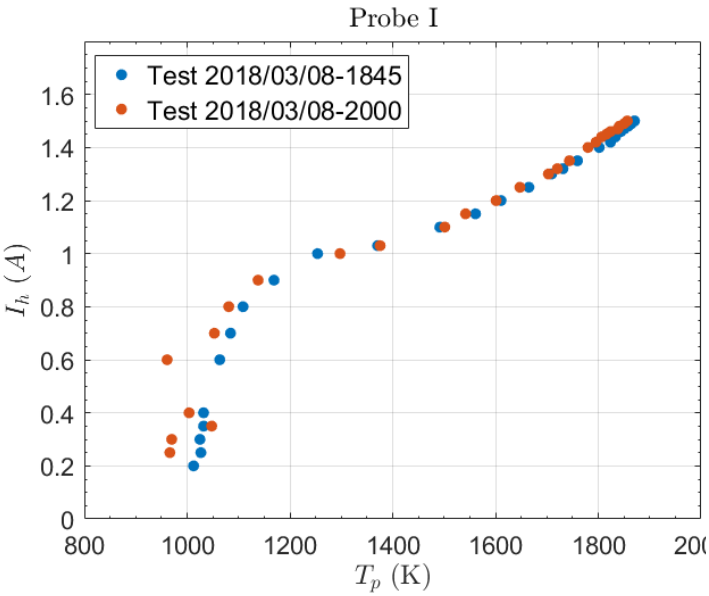

Figure 4.5: Probe I. Experimental T_p-I_h. Vacuum.

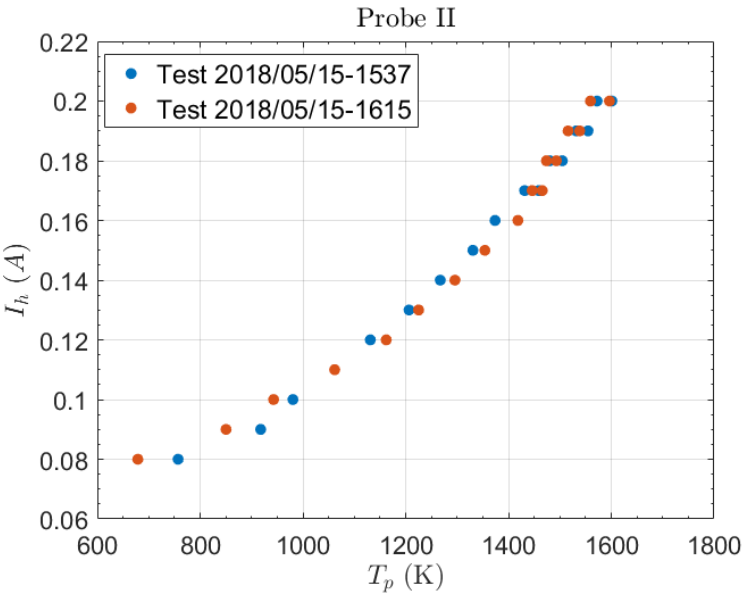

Figure 4.6: Probe II. Experimental T_p-I_h in vacuum

The probes were tested in vacuum to observe their behavior. The I_h-V_h curve of each probe (as in Figures 4.1 and 4.2) can be used as a reference to gauge the contamination level of the probe. In previous tests, it was observed that high pollution levels decrease the resistance of the probe. For that reason, it was decided to use heat to remove any pollution from the filament surface. Both tests performed with each probe were performed on the same day, without interruption on the chamber

vacuum, to try to reduce the pollution to a minimum level.

In these cases, Figures 4.1 & 4.1 and 4.5 & 4.6 show that probe behavior of both tests on each probe seem to agree. However, the agreement is weaker in Probe I than in Probe II. Regarding this thermal response, more tests performed afterwards showed even higher instability on the I_h-V_h curve of Probe II, while Probe I was see to have a more stable response.

These results lack of importance for plasma diagnostics but show a consistency on the probe results. In Figure 4.5, the temperature of the probe seems to plateau for low heating currents. This may be due to other heat losses as conduction to other components (given the probe inner geometry and imperfections) that only seem to be overcome when the probe operates at high temperatures. In Figures 4.5 (at high temperatures) and 4.6, the probes seem to behave as expected in Section 3.3

4.2 Heating curves in the presence of plasma

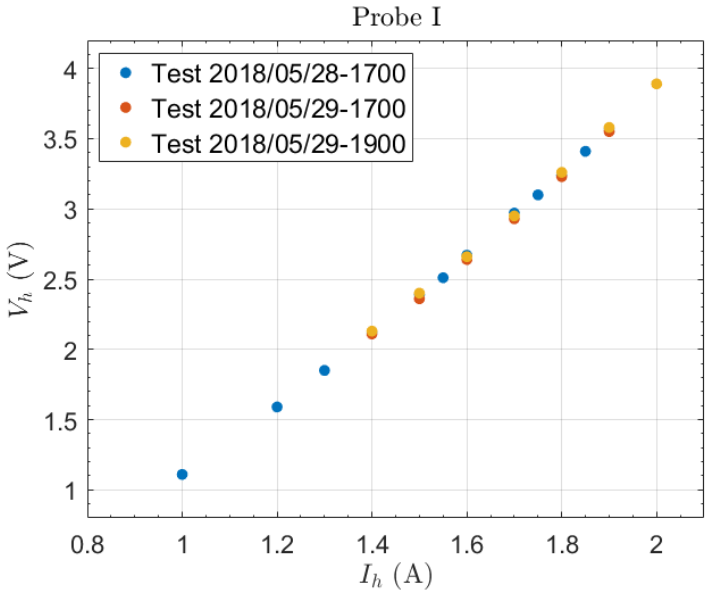

Figure 4.7: Probe I. Experimental I_h-V_h in plasma

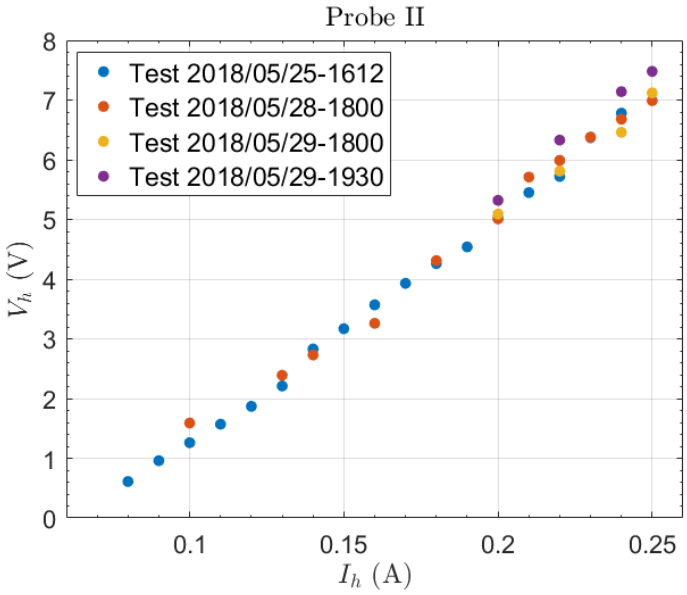

Figure 4.8: Probe II. Experimental I_h-V_h in plasma

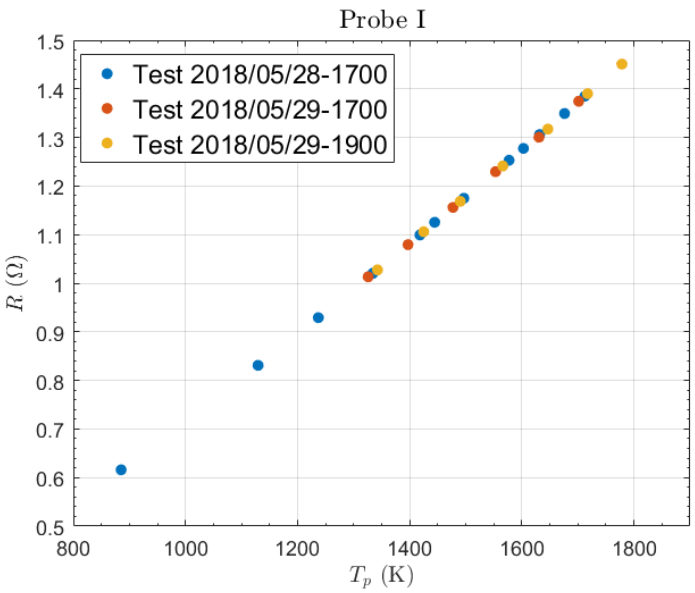

Figure 4.9: Probe I. Experimental T_p-R in plasma

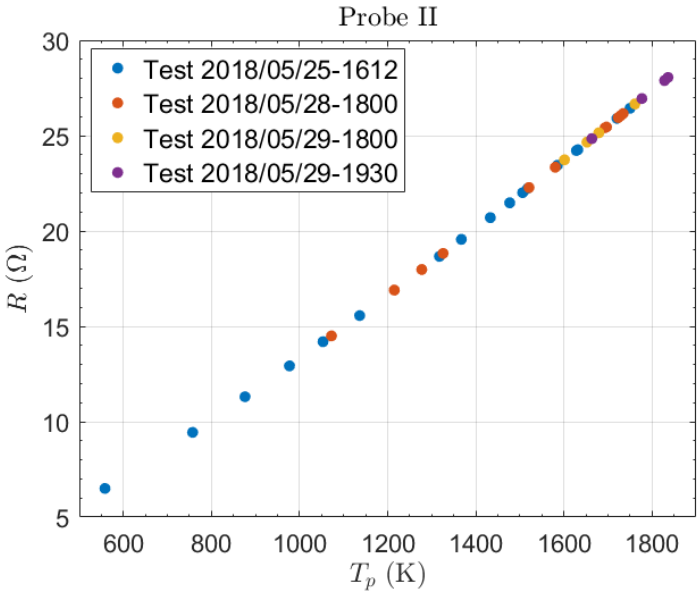

Figure 4.10: Probe II. Experimental T_p-R in plasma

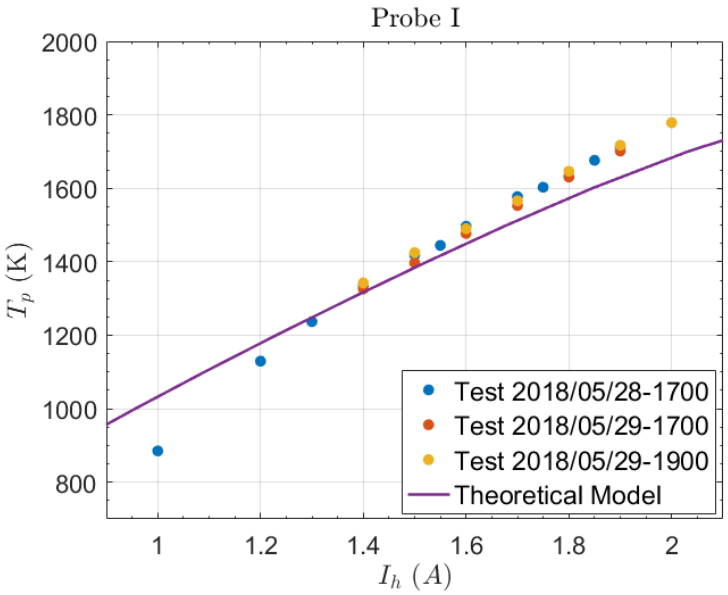

Figure 4.11: Probe I. Experimental I_h-T_p in plasma

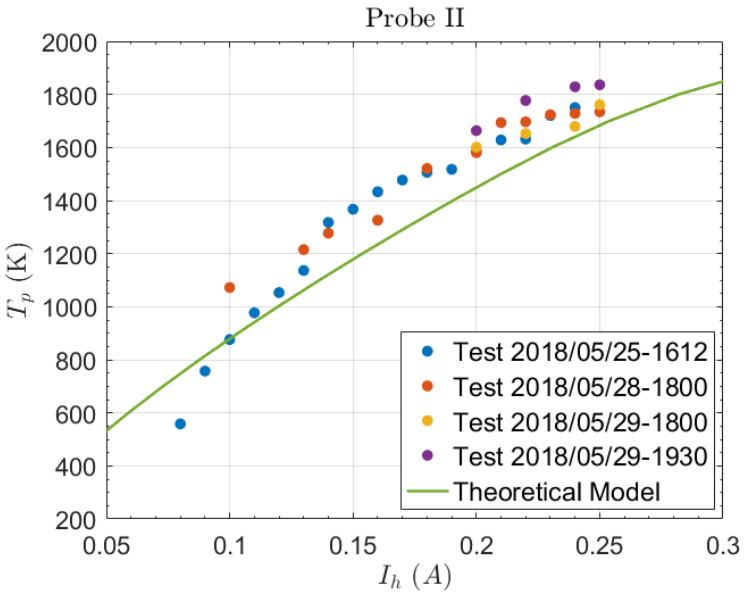

Figure 4.12: Probe II. Experimental I_h-T_p in plasma

Let us assume that, for the thruster operations that were run repeatedly in shot periods of time, the plasma was at the same condition. Besides, the mass flow of the plasma can also be changed, which would generate other plasma conditions. This is important to be remarked as even if the probes are supposed to behave equally at all cases, the measured floating potential, which depends on each plasma potential, will not be the same. Different tests have been joined under similar conditions (I,

II and III) in Appendix C.

Data in this section show the heating performance of both probes under **different plasma conditions**. It can be seen in Figures 4.7 and 4.11 that different tests of Probe I agree with each other, although the results for Probe II in 4.8 and 4.12 are more scattered. Moreover, in Figures 4.11 and 4.12, the theoretical models from Section 3.4.3, in equation 4.4, are seen to resemble the experimental results, apart from deviations caused by other parameters not taken into account in the model. In principle, this would suggest that the energy balance from equation 3.21 is not accurate, but instead an estimation.

$$I^2 \cdot \frac{L}{\pi r_p^2} \cdot \rho_t(T) = S_p \epsilon \sigma T_p^4 + A_G T_p^2 exp(\frac{-eW}{k_B T_p}) \cdot S_p \cdot W \tag{4.4}$$

The maximum deviations between the experimental results and the theoretical model are seen to be of around 100K for Probe I(Figure 4.11) and around 200K for Probe II (Figure 4.12). Some error sources have been identified as follows:

- Due to manufacturing errors and the dislocation of the filament by thermal expansion and contraction during heating cycles, the emissive surface parameters (S_p and L) were not regarded correctly.
- Due to Space Charge Limited effects, the emitted current may be lower than the theoretical Richardson Dushman emission, $I_{em} < I_{RD}$. If the actual energy loss was lower than expected, the material temperature would be higher.
- Since the resistivity law applied to both the theoretical model and the experimental data is the same, it should not be a source of deviation.

Finally note that even though the difference in plasma conditions for different tests is similar in both probes, Probe I seem to behave more uniformly as in contrast between Figures 4.7-4.8 and 4.11-4.12. In Figures 4.7and 4.8, given that $R_p = V_h/I_h$, it can be concluded that the resistance of Probe I behaves smoothly while the resistance of Probe II changes abruptly.

From this experimental results, two conclusions can be made. Firstly, the energy model developed in Section 3.4 can be assumed to be a decent approximation, which accuracy is still pending to be analyzed. Secondly, a larger probe filament radius as in Probe I ($r_p = 5 \cdot 10^{-5} m$) show a more uniform performance during different tests and plasma conditions. Probe II, with a smaller probe filament radius ($r_p = 1.25 \cdot 10^{-5} m$), seem to perform slightly irregularly for different tests and conditions. Due to manufacturing imperfections, the probes are not exactly equal, each probe should behave equally for different firings. For that, it can be inferred that a probe filament is more disrupted by small disturbances in the system as its radius decreases.

4.3 Floating Potential

4.3.1 V_f as a function of Heating Current

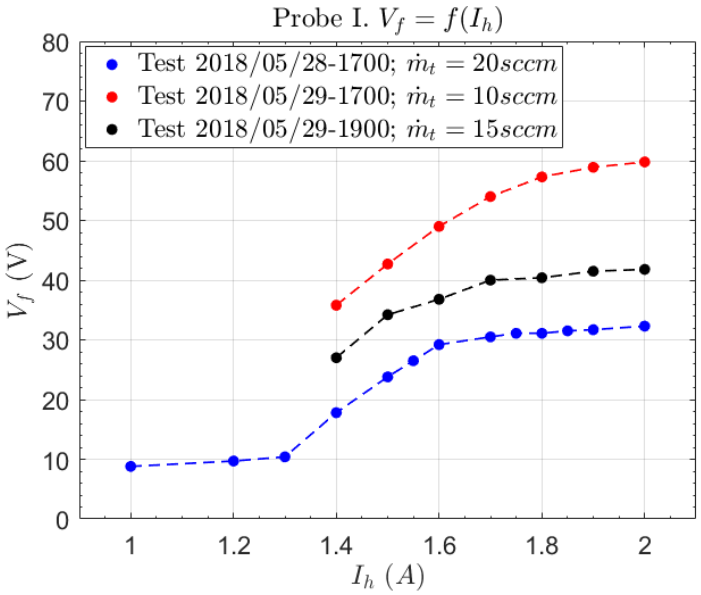

Figure 4.13: Probe I. Floating potential for different plasma conditions

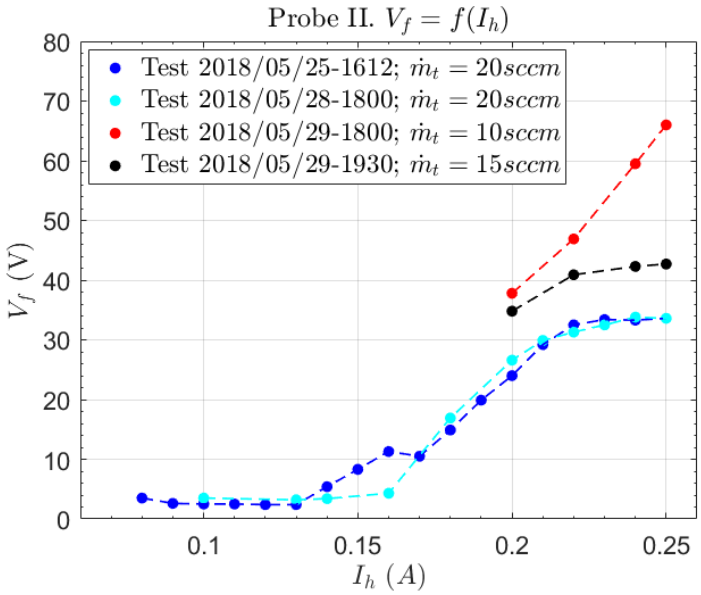

Figure 4.14: Probe II. Floating potential for different plasma conditions

During the tests on the previous section, the floating potential was also measured for each plasma condition. The highest floating potentials for each plasma condition measured by each probe are depicted below.

	$\dot{m}_t$= *20 sccm*		$\dot{m}_t$ = *15 sccm*		$\dot{m}_t$ = *10 sccm*	
	Probe I	**Probe II**	**Probe I**	**Probe II**	**Probe I**	**Probe II**
$V_{f,max}$ **(V)**	32.3	33.6	41.8	42.7	59.8	66

Table 4.2: Maximum measured floating potentials

The behavior of the high emission plateau region of both figures is caused by Space Charge Limited effects, as explained in 2.2.1. For low heating currents, at low probe temperatures, the flat region of the floating potential is dominated by the fact that the emitted current is negligible respect to the plasma electron current and the plasma ion current, in that case $V_f = f(I_e, I_i)$.

In Figure 4.13, Probe I appears to perform smoothly for all three plasma conditions. The three test curves seem to be shifted up and right, and they appear to have reached the plateau region. From the curve shift and the thruster mass flow

rate of each plasma condition, it can be stated that for lower $\dot{m}_t$, a plasma at higher potential will be generated and a greater probe temperature (or current) will be required.

In Figure 4.14 the floating potential of Probe II at $\dot{m}_t = 20sccm$ and $\dot{m}_t = 15sccm$ seems to have reached the plateau region. For $\dot{m}_t = 10scmm$, it has not reached the saturation region. In spite of this, Probe II is already measuring potentials of 66V, which is higher than the 59.8V measured in the plateau region of this plasma condition by Probe II (Figure 4.13). It can be expected to float above Probe I when it reaches the saturation region.

4.3.2 V_f as a function of T_p for equal plasma conditions

Since each probe require different I_h to get to the saturated region, let us plot each floating potential as a function of probe temperature, as the theory shows that the probes should be at similar temperatures.The current is different only due to the thickness difference.

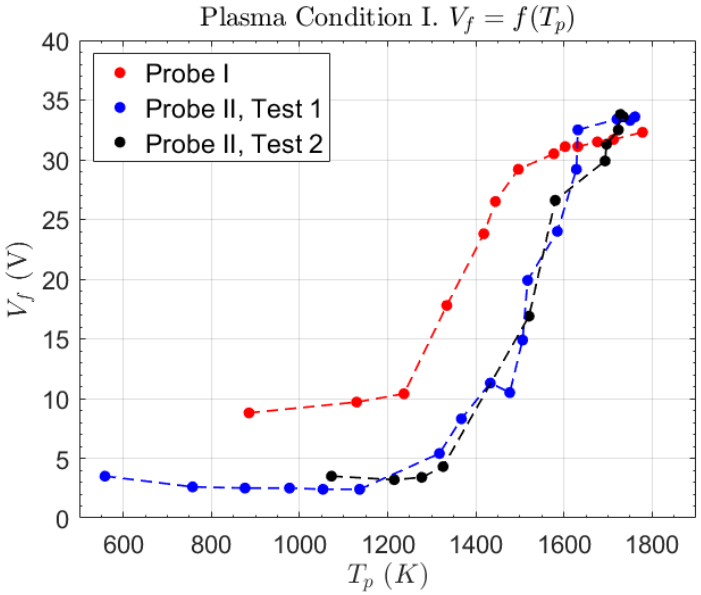

Figure 4.15: Plasma Condition I ($\dot{m}_t = 20sccm$). $V_f(T_p)$ for different probes

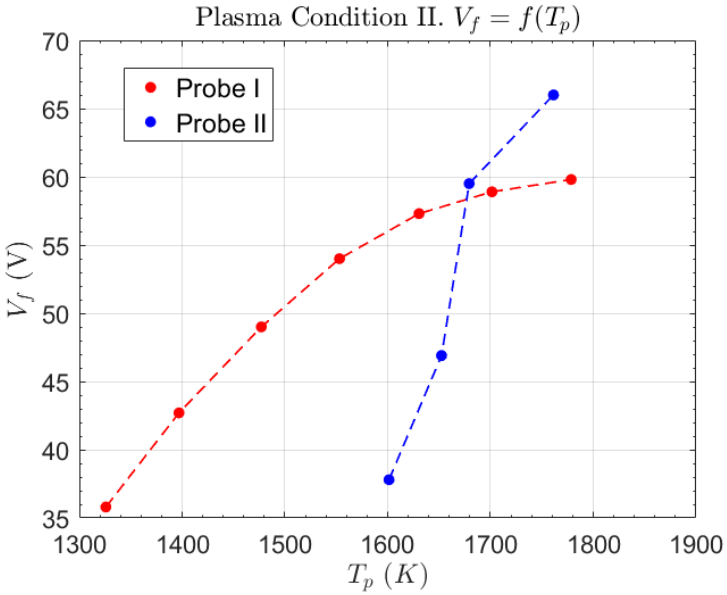

Figure 4.16: Plasma Condition II ($\dot{m}_t = 10sccm$). $V_f(T_p)$ for different probes

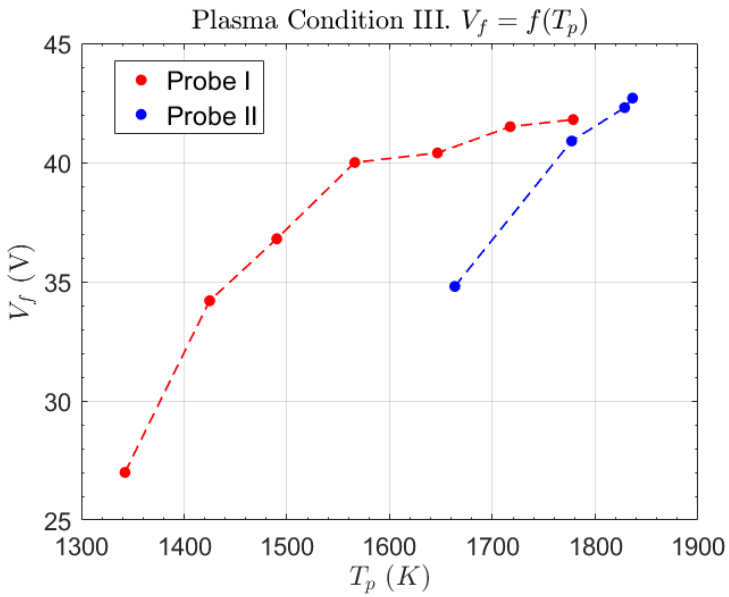

Figure 4.17: Plasma Condition III ($\dot{m}_t = 15sccm$). $V_f(T_p)$ for different probes

Firstly, it can be observed that the thermal response of Probe I is not stable even for the same plasma conditions as in Figure 4.15. For the three plasma conditions, it can be seen the abrupt behavior of the $T_p - V_f$ curves for Probe II. This is related with the representative $I_h - V_h$ abnormally deviated results in Figure 4.8.

In theory, the floating potential measured by both probes at low temperatures, before the exponential V_f increase, should be equal. It can be observed in Figure 4.15 that this was not fulfilled during the experiments.

It can be observed that the thiner probe holds steeper slopes in the $V_f - T_p$ curve. This is the characteristic curve of the Floating Point Method and thus, these are important parameters to analyze. Given the curve behaviors in Figures 4.15, 4.16 and 4.17, the thinner probe is seen to saturate at higher probe temperatures and floating potentials. Recalling the theory in Section 2.2.1 (Figure 2.7), when the probe bias is close to the plasma potential ($V_p \approx V_s$), the non monotonic profile of the sheath potential distribution needs to be considered (Figure 2.2, curves 3 & 4). On that region, due to the non monotonic profile, most emitted electrons will be reflected back to the probe. As a result, an increase on the thermionic current (increasing temperature) will only slightly increase V_f. Since from the experimental results, the thiner probe is seen to float at higher potentials, it could be discussed if thinner probes are more accurate when it comes to determine a plasma potential.

CHAPTER 5

Non Conventional Probe Preliminary Design

Recent material advancements have lead to the use of new low work function materials in thermionic emission applications. The use of these new materials in plasma diagnostics is beginning to be studied as in [46]. A lower work function will result in a lower probe temperature at the saturation region of the Floating Point Method (equation 3.2). For this, the floating potential of non-conventional probes will saturate at lower temperatures in the F.P. Method. It is suspected that the range of increasing temperatures after the saturation begins, until probe failure, will be larger than in conventional tungsten probes, since the saturation begins at lower temperatures [46]. Not only this means that the plasma potential accuracy increases (since the floating point slightly increases from the knee of the F.P.Method, as in Figure 2.7), but also the performance can be stated to be enhanced.

5.1 Non-Conventional Emissive Materials

Hexaboride emitters

The search for specimens able to maintain a sufficient emission level at lower temperatures has lead to refractory ceramic materials, such as lanthanum hexaboride (LaB_6) and cerium hexaboride (CeB_6), which are also able to resist decomposition by heat, chemical effects or pressure. In addition, the use of electron doped dodecacalcium hepta-aluminate (C12A7 electride) will be considered as experimental material due to its ionic inorganic material properties.

Borides are substances composed by boron and a less electronegative element. Hexaboride properties depending on its temperature, composition and its formation mechanism have not been deeply studied so far. However, the analysis of LaB_6 has arisen given the importance that is has reached as thermionic emissive material in industrial processes, and even so, only the single-crystal thermionic properties are being studied in detail.

The difficulties related with the analysis of hexaboride properties are abroad, but are mainly related to the substantial lattice structure variations given by its impurities. The amount and type of impurity are usually the result of the formation method that is used to obtain the hexaboride [45]. In 1986, studies of three LaB_6 single-crystal specimens showed the homogeneity on LaB_6 properties for different crystals, which were assume not to have the exact same impurities [37]. This properties homogeneity was observed for temperatures up to 2000 K. It can be concluded that given its low work function, the temperature at which this material emission reaches a sufficient level will not surpass 2000 K. For that reason, single crystal LaB_6 is typically used for industrial applications, as its performance can be anticipated and its powder can be easily originated from oxide powders as in [16].

$$La_2O_3 + 6B_2O_3 + 21Ca \rightarrow 2LaB_6 + 21CaO \tag{5.1}$$

With regards to the application of hexaborides to emissive probes, if Jules Heating method is applied, the electrical properties of the materials shall be mentioned. On one side, LaB_6 is considered as a superconductor with a critical temperature of 0.41 K. Hence, a lower resistivity than tungsten is expected. Experimental studies have been performed regarding this parameter measurement. In [67], it was concluded that as a function of temperature, it could be linearly fitted as

$$\rho_{LaB6}(T) = 4.1 \cdot 10^{-10} D^{\frac{-8}{3}} \cdot T \tag{5.2}$$

with D as the ratio between the measured LaB_6 specimen density divided by the theoretical LaB_6 material density. On the other hand, the resistivity of CeB_6 is currently being studied and would have to be fitted from experimental data.

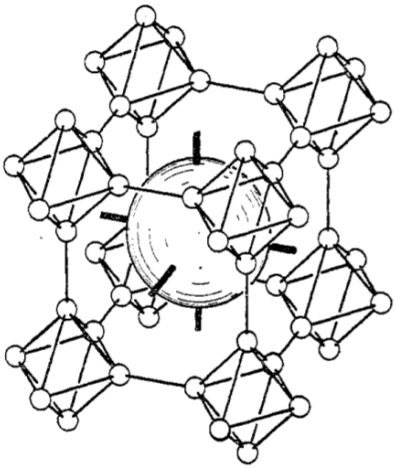

Figure 5.1: Hexaboride lattice, reproduced from [32]. Metallic atom (large) and boron atoms (small).

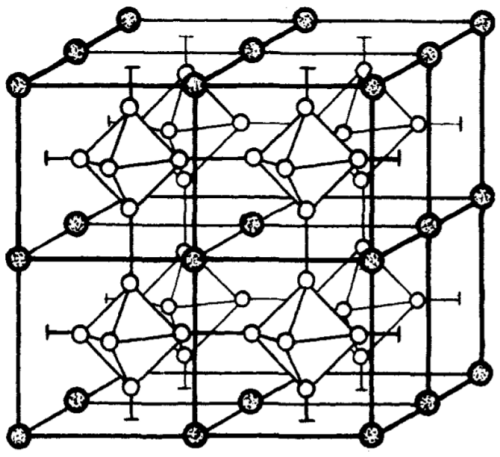

Figure 5.2: Hexaboride lattice, reproduced from [31]. Metallic atoms (gray) and boron atoms (white).

Both LaB_6 and CeB_6 are structured in the same cubic structure as in Figures 5.1 and 5.2. Boron atoms, being smaller in radius with respect to both Lanthanum and Cerium alkali metals, form a framework which traps the larger metallic atom inside. Each boron atom has three valence electrons divided into 5 bonds with the other boron atoms. In theory, there are no bonds between the boron atoms and the trapped metallic one. Hence, the valence electrons of the metal atom become free electrons [38]. For that, these materials are good electrical conductors. On the other hand, the strong bonding forces between boron atoms provide the materials with high melting points and mechanical stability at high temperatures, which makes them suitable for cathode applications. When these substances are heated to high temperatures, the surface metallic atoms evaporate, but are immediately replaced by diffusion by other metallic atoms from deeper material layers. During this process, the boron structure changes are minimum and can be neglected. As a result, the surface of the material is kept thermionically active at all times, until there are no metallic atoms left, and the emissive material is assumed to be too degraded.

When it comes to material performance, CeB_6 shows lower evaporation rates than LaB_6 up to temperatures temperatures around 1800 K. As a consequence, under that temperature, the lifespan of CeB_6 emitters will be higher than that of LaB_6 emitters. Even though CeB_6 emitted current density is slightly lower than LaB_6 current density [1], cerium boride may be more convenient for emissive temperatures up to 1800 K.

C12A7 electride emitters

$C12A7 : e^-$ is a novel substance with considerable physical properties regarding electron emission when it is at the electride state. Such properties are a result of its lattice [43]. This porous material is composed by dodecacalcium hepta-aluminate ($2CaO \cdot 7Al_2O$), a mineral inorganic solid that rarely occurs in nature. When it does, it naturally appears in the form of chlormayenite, a calcium aluminum oxide mineral. $C12A7 : e^-$ has a nanostructure which forms a cubic crystal lattice as shown in Figure 5.4.

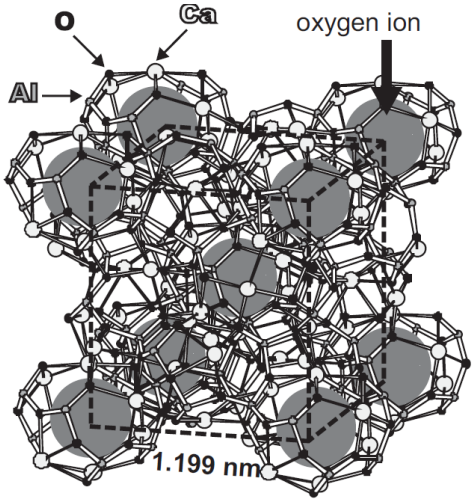

Figure 5.3: C12A7 crystal structure, reproduced from [62]

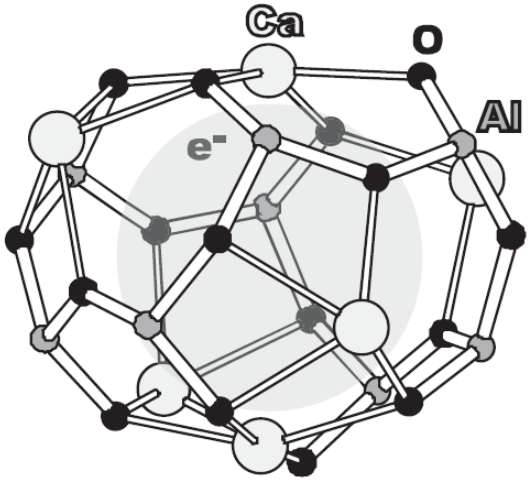

Figure 5.4: $C12A7 : e^-$ unitary neutral cell, reproduced from [62]

Individual cells of C12A7 formed by $[Ca_{24}Al_{28}O_{64}]^{4+}$ are positively charged, which means that there are less electrons than the 4 electrons that are needed to neutralize the cell [43]. This polarity is neutralized in natural C12A7 by means of two atomic oxygen ions, $2 \cdot O^{2-}$ in the cell composition. $[Ca_{24}Al_{28}O_{64}]^{4+}(O^{2-})_2$. This two O^{2-} can be substituted in the structure by 4 electrons in order to form the C12A7 electride, $[Ca_{24}Al_{28}O_{64}]^{4+}(e^-)_4$ (also known as $C12A7 : e^-$) [36].

Electrides are compounds structurally characterized by having electrons placed in the lattice to neutralize it acting as anions. Thus, those electrons are not delocalized. As a consequence of the large lattice distance in the cell, the energy required to extract those electrons from the material is lower, which results in a lower work function, and an increase of electron emission [14]. Most electrides form crystalline salts with alkali metals and decompose in medium to high temperatures. However, $C12A7 : e^-$ is known for being stable at high temperatures and hence, this makes it a suitable candidate for thermionic emission purposes. However, its performance and reliability are still pending to be analyzed.

	LaB_6	CeB_6	$C12A7 : e^-$
W [eV]	2.66	2.6	0.6
A_G $[\frac{A}{m^2K^2}]$	$2.9{\cdot}10^4$	$3.6{\cdot}10^4$	-
Emissivity Factor ϵ	0.765	0.779	-
Melting point [K]	2483	2463	1670
ρ_0 $[\Omega \cdot \text{m}]$ at T = 293 K; p = 1 atm.	$5{\cdot}10^{-10}$	$6.5{\cdot}10^{-10}$	-
Density $[\frac{g}{cm^3}]$ at T = 293 K; p = 1 atm.	4.72	7.8	2.68
Vaporization rate at 1750 K $[\frac{g}{cm^2 \cdot s}]$	$2.2{\cdot}10^{-9}$	$1.6{\cdot}10^{-9}$	-

Table 5.1: General properties of non conventional thermo-emissive materials obtained from [38], [63] and [48]

5.2 Preliminary Design Material Considerations

In reference to the material parametrization performed in Section 5.1, non conventional probes are intended to be studied. For these probes both LaB_6 and CeB_6, along with $C12A7 : e^-$, will be proposed to be used as thermionic materials. However, it was stated during the analysis of these emitters that is not possible to shape their raw materials into a thin filament. For this reason, the current conventional probe design has to be disregarded. That brings the need to use other materials and geometries in order to have a useful emitting surface.

To begin with, all three non-conventional materials are usually obtained as powders. This is solved in [46] by using small cylindrical boride rods as thermionic tips, and then using a complex holding system to both keep the tip in position and to provide it with an electrical current. The holding system acts as a clamp and its designed to accommodate the tip for thermal expansions.

It is clear that as a tip holding system is more complex than a filament wrapped around a wire, as in conventional probes, more parts will be involved in these designs. As a heating current needs to be driven through the emissive tip, the idea is to design tweezers that act as a conductive connector between the tip and the power source, while holding it in place. Due to the thermal and electrical conditions at which this clamping system will be exposed, its composition needs to be analyzed.

Emissive Tip

Known non-conventional material properties are depicted in Table 5.1. The idea of using this material comes from their low work function. Because of it, the temperature required to reach a substantial emitting is reduced a lot. However, these species

are also good electric conductors, specially LaB_6 which is a superconductor at low temperatures ($< 1K$). Jules Heating is the intended mechanism to be used to get the emissive surface to the required temperature. The resistivity developed by these materials, ρ, is expected to be low. Thus, the tip geometry needs to be sized so that a finite and achievable current I_h is required to reach the desired temperature, T_p. The tip performance analysis would have to be performed experimentally as the resistivity law changes depending on specimen composition.

Holding Tweezers

The clamping system must be capable of withstanding the tip in a stable position throughout the whole probe operation. For that, the heat expansion coefficient (α)can be analyzed.

	Tungsten	**Stain. Steel**	**Aluminum**	**Copper**	**Steel**	**Graphite**
W [eV]	4.54	4.4	4.06-4.26	4.65	4.67 - 4.81	≈ 5
α $[\frac{m}{m \cdot K}]$	4.5	9.9 - 17.3	21-24	16-16.7	11-12.5	4-8

Table 5.2: Material properties from [20] and [10]

Since a current is going to be driven through the material, it is important to design it with conductive materials and a cross section wide enough so that it will not provide a large resistivity and heat up too much. If it heats up to a certain temperature, it may start to emit electrons from its surface and the probe measurements may be affected. In [46], graphite tweezers are used for good electric conductivity at high temperatures high work function and low thermal expansion of carbon.

Ideally, it is seen that carbon would be the most suitable material for the clamping system. However, more common metals shall be used in the first designs for their low cost, given the amount of material needed.

Both plates that form the tweezers need to be electrically isolated from each other to avoid shot circuits. An alumina fulcrum can be used as supporting point, for its good electric isolation and low cost.

Heat protection

The emissive surface is required to be completely immersed in the plasma plume for the probe to operate properly. As a result, it means that the holding system will be exposed or semi-exposed to the plasma, at high electron temperatures. In [46], apart

from the tip, the probe is covered in Rescor^{TM}310M silica foam and boron nitride foam, isolating the holding mechanism from the plasma and acting as a thermal barrier. The probe side closer to the tip is actually covered by high performance boron nitride foam. This heat protection would be desirable in a definitive probe design. Nonetheless, those materials are fairly expensive and it has been decided to include them once these probes are experimentally proved to be more useful than a cheaper conventional thoriated tungsten probe.

5.3 Design Features

Finally, based on the ideas provided in [46] and by boride cathode manufacturer designs, a simple conceptual design is depicted in Figures 5.5 and 5.6. The main goal of the concept is to be able to be adapted to the conventional design experimental set up, as well as be reusable as the emissive tips are degraded.

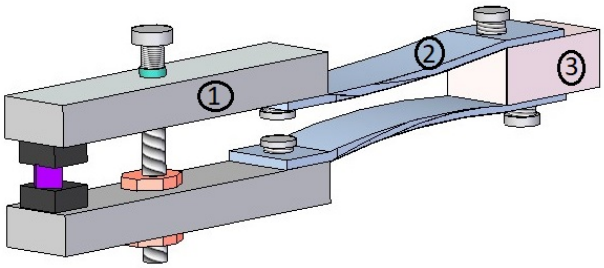

Figure 5.5: Conceptual non conventional probe design. Left side

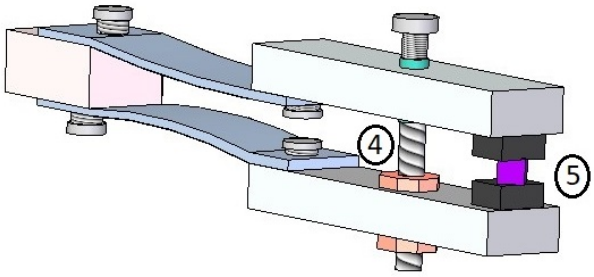

Figure 5.6: Conceptual non conventional probe design. Right side

Remark in Figures 5.5 and 5.6 the following features:

- **No. 1**. The main structure is made out of aluminum. It needs to be stiff enough to act as a clamp in the boride tip when perpendicular force is applied by the screw.
- **No. 2**. It is made out of spring steel. It provides flexibility to the mechanism, so that it is possible to change tips easily.
- **No. 3**. It needs to be made out of an electrical isolator material as alumina. It acts as support point and separates electrically the upper side from the lower side of the tweezers. The external heating circuit must be connected on both sides of the probe so that the current is forced to flow through the emissive tip.
- **No. 4**. This mechanism makes the holding system to act as a lever. Two nuts are fixed on the lower part, where the hole through the aluminum plate is flat.

The screw can rotate freely there but it can not move perpendicular to the plate. In the upper side hole, an alumina collar is placed to electrically isolate the screw from the upper plate , so that shot circuits are avoided. The collar is screwed, so that when the screw is rotated the plate is forced perpendicular to it. This mechanism hold the tip in position.

- **No. 5**. Two carbon pieces are placed between the plates and the boride tip, to avoid material depletion.

This probe geometry is only a proposition, and it can be simplified or changed in a vast amount of modes depending on the purpose, the re-usability and the available setup where it would be used. As long as the material considerations in Section 5.2 are regarded, the key feature to focus is the emissive tip.

5.4 Device Manufacture

While most parts of the probe can be manufactured with simple conventional methods, the non-conventional material tips deserve certain consideration given the problems that they bring. The non-conventional materials are available as powders, but a solid rigid body is required to be used as tip. Firstly, a hydraulic press was used to apply mechanical pressure to each species, at relatively low pressures. The electride was successfully solidified, and it was ready to me, machined into a useful tip. However, this method failed to process both borides. Despite their good thermionic properties, it was seen that this materials imposed an extra degree of complexity related to their machining process.

Cold Isostatic Press

This method was then tried to achieve greater mechanical pressures on the boride powders. In this method, powder is covered by a flexible plastic, shaped as a small chip, and immersed in a liquid. The container holding the liquid is pressurized by means of a fluid pump. Hydrostatic pressure is then applied to the whole surface of the chip , so the pressure of distributed homogeneously. This isostatic process conducted at room temperature is deeply analyzed in [49].

After applying a pressure of 6000 psi for 15 minutes on each boride, a brittle semmisolid piece was obtained. It was then concluded that the powders were not going to be processed only by pressure, and an increase of material temperature was required to achieve a mechanically stable piece.

Hot Pressing

This kind of pressing is the first proposed solution to introduce sintering. Sintering is the process of forming a solid piece from powder by applying heat and pressure but without reaching the melting point of the powder. Other cases of LaB_6 powder consolidation by hot pressing have been recently reported in [56]. By the temperature and pressure that current hot pressure machinery provides, it seems to be a suitable method. Nonetheless, it is suspected that as no powder melting occurs, single crystals are not going be achievable. Hence, impurities will always decrease the thermionic properties of the boride tips fabricated with this method.

Inert Gas Arc Float Zone Refining

This technique is currently being used by electron emission cathodes manufacturers to achieve professional quality on the boride tips. It consists on an electric arc melting a pressed powder rod of LaB_6 or CeB_6 inside a chamber where only an inert gas is present [11]. The power is driven to its liquid phase and then solidifies in a selected orientation, which allows the manufacturers to grow single crystals. This crystals are said to have the best thermionic properties due to the low amount of impurities. This method is typically used on electron microscopy.

Given the melting point of the borides ($> 2000K$), an electric arc seems to be the appropriate method to fuse the powders. Following the previous idea, an arc furnace can be used to try to sinter the boride powders. For simplicity on the first probe designs, the inert atmosphere will not be necessary, as the amorphous solid obtained can be then machined into a rod. Given the unavailability of the required furnace on the project timespan, the manufacture and test of the non-conventional material tips will be left as a future project development. As a result, there will not be experimental plasma measurements with these probes.

CHAPTER 6

Conclusion

After a literature study on emissive probes and its plasma interaction, conventional emissive probes have been designed.Overall, it was seen experimentally that the probe with larger filament radius (Probe I) showed decent results.

The thermal response of the probes has been studied. The first conclusion obtained was that the energy loss due to emitted electron current ($W \cdot I_{em}$) could not be neglected on the energy balance of the probe. In particular, it was seen that on the temperature range of the saturation of floating potentials on the FP Method, this energy loss increased exponentially as in Figure 3.16. The deviation between the theoretically estimated energy loss and the experimental one can has been regarded in the temperature difference on Figures 4.11 and 4.11.

Thermionic emissive material properties have been seen to have a great importance on the probe-plasma interaction. Γ was described by Hobbs as the key parameter to define at which T_p would the floating potential saturate on the FP Method .

$$\Gamma = 1 - 8.3 \cdot (\frac{m_e}{m_i})^{\frac{1}{2}} = \frac{\lambda_B(1 - r_{av})A_0 T_p^2 exp(\frac{-eW}{k_B T_p})}{eN_\infty \sqrt{\frac{k_B T_e}{2\pi m_e}}} \tag{6.1}$$

Γ was seen to influence two parameters:

- The emissive material importance for high plasma electron densities. It was observed that for higher N_∞, the temperature of the beginning of the plateau region on the FP Method increased. However, this temperature was seen do decrease for lower emissive material work functions. It was then concluded that given that Γ is independent on probe geometry, the chosen emissive material properties is the key for EP design.

- From Γ, even though the plasma parameters during the experiments were only an estimation from previous tests, a guideline for experimental set-up design can be obtained.

The influence on conventional probe radius has been assessed. It was observed that smaller probe radius approached better the real plasma potential, given that the measured floating potentials at the same conditions were the highest. This is a consequence of the Floating Point Method underestimating the plasma potential for Space Charge Limited Effects. Due to the relation between the filament cross section, the resistivity and the required heating current on Jules Heating, smaller probes were seen to be characterized by a lower heating power requirement. However, it was observed on the experimental results that the smaller probe achieved a worse thermal response. From this, it was suspected that disturbances in the plasma produced larger perturbations on smaller probes. Nonetheless, this bad thermal response was also suspected t be caused by probe mechanical malfunctions caused by an imperfect probe manufacturing (on the filament wrapped with the copper connector wires). It was concluded that as smaller probes are much harder to manufacture due to the filament thickness, the mechanical and electrical contact fabricated was not as reliable as in larger probes. Thermal expansion is also suspected to affect this, since if the worse mechanical fixation, the more dislocation will be produced by thermal expansion and contraction cycles.

Disregarding non-idealizations as space charge and orbital effects on electron collection, the performance model of two conventional probes has been simulated. For that, the energy balance of the system has been depicted. It was seen in Figure 3.7 that at low probe temperatures, the main energy loss comes from the filament radiation. Nonetheless, at high probe temperatures, the equilibrium of the thermal system was dominated by electron emission, assuming a monotonic potential profile and $V_p < V_S$. From the model results and Γ estimation, the experimental power requirements were obtained to perform a fast EP Scanning.

From the previous deductions on emissive material influence and probe manufacture difficulties, non-conventional probes were introduced as a possible solution:

- A low work function would allow to measure floating potentials at higher plasma electron densities on Hobbs Law (Γ). From this either same plasmas can be diagnosed with low probe temperatures, or more energetic plasmas that those at which conventional EPs can be exposed to, can be measured.
- The unreliable thermal contact between the filament and the wire, on a conventional probe caused by the manufacturing difficulty, can be overcame by non-conventional probe designs as in Figure 5.5. The time-consuming process of replacing probe filaments on conventional probes can be disregarded by these kind of designs in which the emissive tip can be replaced without any difficulty.

A characterization of non-conventional materials with low work function was performed. A probe design was proposed in order to compare its performance with respect to conventional thoriated tungsten probes. Due to the innovative character of these materials, some manufacturing difficulties were encountered when it came to fabricate the boride emissive tips. Manufacturing methods inspired by what it is currently being used to fabricate LaB_6 cathodes in electron emission microscopy have been proposed. Due to the boride property dependence on formation method, the performance of the probes shall be tested before using them to determine a plasma potential. It was concluded that despite their appropriate thermionic properties, borides impose an extra degree of complexity on probe manufacturing as their powders need to be sintered at high temperatures.

Future prospects

As a consequence of the experimental results obtained and the manufacturing issues obtained, there is still plenty of room for improvement. In first place, it is recommended to perform again the experiments with more probe radius to check the trend of the $V_f - T_p$ results. In particular, larger probe sizes are recommended due to their more stable thermal response. Besides, a deeper analysis of the probe thermal response variation with filament radius needs to be assessed. Plasma diagnosis tests in which Langmuir probes are also used should be performed to asses qualitatively the thoriated tungsten resistivity law used. From that analysis, the accuracy of the probe resistance as a function of temperature depicted on this project shall be assessed. Other methods to estimate the relation between resistance and material temperature should be attempted.

Furthermore, the thermal model proposed should be improved to take into account other parameters influencing the plasma-probe interaction, as the plasma ion current. Other non-idealizations from Chapter 2 could be considered on the model.

Regarding experimental measurements with conventional probes, complete I-V curves could also be obtained to check the validity of the test with the theory. The Inflection Point Method from Section 2.2.2 shall be performed along with the FP Method to asses the difference of their results. This would provide quantitative data to the current argument on their differences and accuracies.

Following the guidelines from this project and the proposed manufacturing techniques for the boride emitters, non-conventional probes shall be fabricated and tested. The variance on their floating potential results respect to the conventional probes in the same plasma conditions shall be assessed.

Appendices

A Electron random-thermal current

I_{th} can be obtained from the velocity distribution average $< v >$ of only the collected plasma electrons moving towards the probe. Such average velocity is said to be the result of the first moment of the distribution function in a steady and spatial homogeneous situation [30].

$$< v >= \int_0^\infty v \cdot f(\vec{r}, \vec{v}, t) dv \qquad , \qquad I_{th} = S_p e < v >_{Maxw} \tag{2}$$

The electrons are assumed to follow a Maxwellian Distribution. The **Maxwellian Velocity Distribution** is defined as the most probable distribution of velocities for a group of particles in thermal equilibrium [4].

- For a **Planar** case, the first moment of distribution function is applied to the electrons towards the probe. [4]

$$f(v)_{Maxw.} = N_\infty \sqrt{\frac{m}{2\pi k_B T_e}} \cdot exp(\frac{-m_e v^2}{2k_B T_e}) \tag{3}$$

Applying equation 2 to this distribution, it yields:

$$I_{th} = S_p e \int_0^\infty v \cdot N_\infty \sqrt{\frac{m}{2\pi k_B T_e}} \cdot exp(\frac{-m_e v^2}{2k_B T_e}) dv =$$

$$= S_p e N_\infty \sqrt{\frac{m}{2\pi k_B T_e}} \int_0^\infty v \cdot exp(\frac{-m_e v^2}{2k_B T_e}) dv \tag{4}$$

Imposing a change of variable such that $x = \frac{m_e v^2}{2k_B T_e}$ and $dx = \frac{dx}{dv} dv$, it results in:

$$I_{th} = S_p e N_\infty \sqrt{\frac{m_e}{2\pi k_B T_e}} \cdot \frac{k_B T_e}{m_e} \quad = \quad S_p e N_\infty \sqrt{\frac{k_B T_e}{2\pi m_e}} \int_0^\infty exp(-x) dx \tag{5}$$

$$I_{th} = S_p e N_\infty \sqrt{\frac{k_B T_e}{2\pi m_e}} \tag{6}$$

As expected from the planar collection theory, it will be constant for a given probe geometry, plasma temperature and density. It has been proved that the current is conserved along r.

- For the **Cylindrical** case, the velocity of the electrons towards the probe will be integrated [6]. Applying equation 2, it yields:

$$v^2 = v_r^2 + v_\theta^2 \tag{7}$$

$$I_{th} = S_p e \int_{v_{r1}}^{v_{r2}} \int_{v_{\theta 1}}^{v_{\theta 2}} v_r \cdot N_\infty (\frac{m}{2\pi T_e k_B})^{\frac{2}{2}} exp(-\frac{m_e(v_r^2 + v_\theta^2)}{2k_B T_e}) dv_r dv_\theta \quad (8)$$

Imposing a change of variable, given the fact that the angular momentum (J) and the total energy (E) are conserved in r.

$$E = \frac{mv_r^2}{2} + \frac{mv_\theta^2}{2} \quad , \quad J = mv_\theta \cdot r = \sqrt{2mE} \cdot r \quad (9)$$

The limits of integration will impose no potential barrier given that all electrons can reach eventually the probe: E = [0,+∞]. From eq. 9 and since $E > J$ at the probe surface, $0 < J < \sqrt{2mE} R_p$. Then, eq. 8 yields:

$$I_{th} = 2eS_p \frac{N_\infty}{2\pi k_b T_e m_e r} \int_0^\infty \int_0^{r\sqrt{2m_e E}} exp(-\frac{E}{k_b T_e}) dE dJ \quad (10)$$

dJ is a direct integral while dE can be solved by a change of variable $x = \frac{E}{k_B T_e}$ and then integrated by parts. It results in:

$$I_{th} = S_p e N_\infty \sqrt{\frac{k_B T_e}{2\pi m_e}} \quad (11)$$

Again, it has been shown that the current is conserved along the radial direction.

- Regarding the **Spherical** case, Laframboise proved again in [39] this radial conservation of current, which yields the same expression.

However, note that the effective surface considered (S_p) as the sheath frontier, is not the same in the different cases. Then, the surface variation experienced by the sheath when its radius increases would not behave equally in all cases.

$$S_p = \begin{cases} \epsilon_{inf} & \text{in } \textit{Planar} \\ 2\pi r \cdot L & \text{in } \textit{Cylindrical} \\ 4\pi r^2 & \text{in } \textit{Spherical} \end{cases} \quad (12)$$

Being ϵ_{inf} an infinitesimal dimension. Since the sheath length increases with probe potential, this rate of change in effective probe surface explains the behavior of the collected plasma electron current of Figure 2.4 in Chapter 2.

B Probes Stand

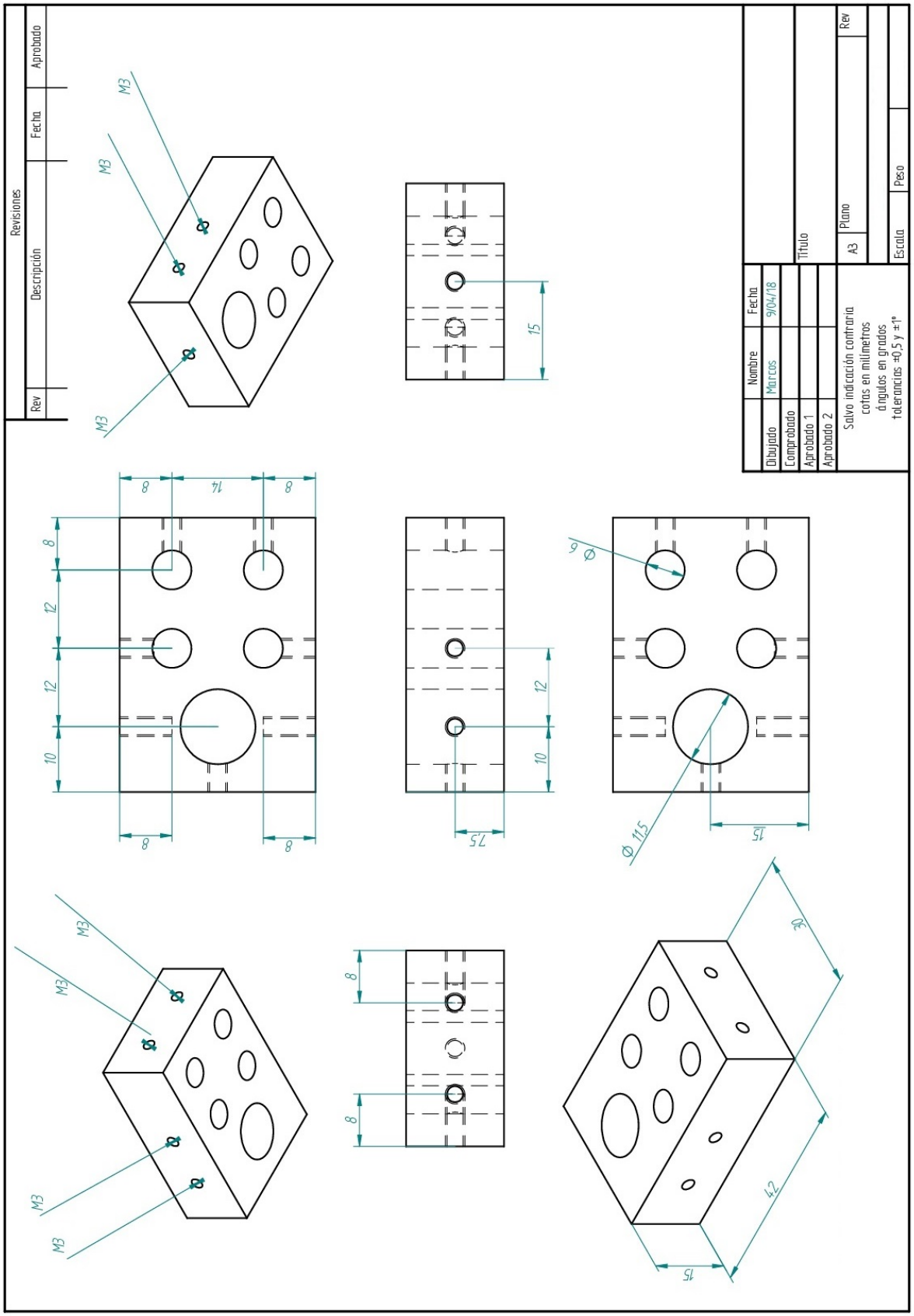

C Numerical experimental results

Each single table considered in this section is composed by data points measured consecutively in single heating cycles. Those cycles were performed increasing the current gradually, in order to try to achieve homogeneity in the procedures and results.

C.1 Vacuum Tests

Probe I	*Test_20180308_1845*	$p = 10^{-8}$ *(bar)*	*Vacuum*
I_h **(A)**	V_h **(V)**	$\mathbf{R}/R_0$	T_p **(K)**
0,20	0,25	4,6624	1012,60
0,25	0,31	4,7409	1026,72
0,30	0,37	4,7262	1024,96
0,35	0,44	4,7686	1032,00
0,40	0,50	4,7660	1032,00
0,60	0,76	4,9489	1063,56
0,70	0,90	5,0739	1084,49
0,80	1,05	5,2078	1108,78
0,90	1,23	5,5584	1169,00
1,00	1,44	6,0641	1253,85
1,03	1,60	6,7599	1370,58
1,10	1,83	7,4977	1491,71
1,15	1,99	7,9259	1561,18
1,20	2,14	8,2382	1610,89
1,25	2,29	8,5769	1665,03
1,30	2,44	8,8649	1709,34
1,32	2,51	8,9983	1731,40
1,35	2,60	9,1790	1759,68
1,40	2,76	9,4478	1801,92
1,42	2,83	9,5861	1823,74
1,44	2,88	9,6538	1833,24
1,45	2,90	9,6494	1833,24
1,46	2,94	9,7197	1844,14
1,47	2,97	9,7629	1850,36
1,48	3,00	9,8054	1858,13
1,49	3,03	9,8474	1864,34
1,50	3,06	9,8889	1870,55

Table 1: Probe I ($r_p = 5 \cdot 10^{-5} m$) measurements in vacuum. $p_{chamber} = 10^{-8}$ (bar)

Probe I	*Test_20180308_2000*	*p = 1.3* 10^{-9} *(bar)*	*Vaccum.*
I_h **(A)**	V_h **(V)**	$\mathbf{R}/R_0$	T_p **(K)**
0,20	0,12	0,5082	177,16
0,25	0,30	4,3974	966,41
0,30	0,36	4,4188	969,98
0,35	0,44	4,8598	1047,81
0,40	0,49	4,6058	1003,76
0,60	0,71	4,3654	961,04
0,70	0,88	4,8919	1053,07
0,80	1,03	5,0465	1081,00
0,90	1,20	5,3803	1138,12
1,00	1,48	6,3205	1297,47
1,03	1,60	6,7910	1375,53
1,10	1,84	7,5559	1501,44
1,15	1,97	7,8144	1541,85
1,20	2,13	8,1848	1601,29
1,25	2,27	8,4744	1647,55
1,30	2,43	8,8156	1703,02
1,32	2,49	8,9254	1720,38
1,35	2,58	9,0840	1743,98
1,40	2,73	9,3104	1780,04
1,42	2,79	9,4056	1795,68
1,44	2,84	9,4758	1806,60
1,45	2,88	9,5433	1815,95
1,46	2,91	9,5880	1823,74
1,47	2,95	9,6756	1837,91
1,48	2,97	9,6972	1841,03
1,49	3,01	9,7614	1850,36
1,50	3,04	9,8034	1856,58

Table 2: Probe I ($r_p = 5 \cdot 10^{-5} m$) measurements in vacuum. $p_{chamber} = 1.3 \cdot 10^{-9}$ (bar)

Probe I	*Test_20180528_1945*	$p = 10^{-8}$ *(bar)*	*Vacuum.*
I_h **(A)**	V_h **(V)**	$\mathbf{R}/R_0$	T_p **(K)**
0,50	0,34	1,1923	335,83
0,80	0,62	1,8013	467,51
1,00	1,13	4,0449	901,51
1,10	1,36	4,7587	1030,24
1,20	1,61	5,4071	1143,28
1,30	1,86	6,0049	1243,74
1,40	2,12	6,5403	1334,13
1,45	2,25	6,7803	1373,88
1,50	2,40	7,0684	1421,59
1,55	2,53	7,2758	1455,92
1,60	2,68	7,5505	1499,81
1,65	2,83	7,8279	1545,08
1,70	2,98	8,0701	1583,68

Table 3: Probe I ($r_p = 5 \cdot 10^{-5} m$) measurements in vacuum. $p_{chamber} = 10^{-8}$ (bar)

Probe II	*Test_20180515_1537*	$p = 3\ 10^{-8}$ *(bar)*	*Vaccum.*
I_h **(A)**	V_h **(V)**	$\mathbf{R}/R_0$	T_p **(K)**
0,08	0,86	3,2625	757,19
0,09	1,20	4,1259	917,78
0,10	1,44	4,4833	980,67
0,11	1,73	4,9424	1061,81
0,12	2,03	5,3389	1131,23
0,13	2,37	5,7769	1206,50
0,14	2,71	6,1405	1267,31
0,15	3,07	6,5222	1330,81
0,16	3,40	6,7833	1373,88
0,17	3,68	7,1343	1431,41
0,17	3,88	7,2980	1459,18
0,18	4,06	7,4333	1480,34
0,18	4,26	7,5796	1504,68
0,19	4,47	7,7450	1532,16
0,19	4,67	7,8930	1554,74
0,20	4,86	7,9991	1572,43

Table 4: Probe II ($r_p = 1.25 \cdot 10^{-5} m$) measurements in vacuum. $p_{chamber} = 3{\cdot}10^{-8}$ (bar)

Probe II	*Test_20180515_1615*	p = *3*·10^{-8} *(bar)*	*Vacuum.*
I_h **(A)**	V_h **(V)**	$\mathbf{R}/R_0$	T_p **(K)**
0,08	0,76	2,8458	678,77
0,09	1,10	3,7556	850,41
0,10	1,37	4,2667	942,95
0,11	1,73	4,9424	1061,81
0,12	2,10	5,5194	1162,15
0,13	2,42	5,8923	1225,15
0,14	2,78	6,3071	1295,80
0,15	3,13	6,6556	1354,04
0,16	3,53	7,0542	1418,31
0,17	3,72	7,2152	1446,13
0,175	3,90	7,3373	1465,70
0,18	4,04	7,3857	1473,84
0,185	4,22	7,5148	1493,33
0,19	4,41	7,6459	1516,01
0,195	4,61	7,7877	1538,62
0,20	4,81	7,9222	1559,57

Table 5: Probe II ($r_p = 1.25 \cdot 10^{-5} m$) measurements in vacuum. $p_{chamber}$ = 3·10^{-8} (bar)

C.2 Plasma Condition I. Thruster operating at $\dot{m} = 20sccm$

Probe I	*Test_20180528_1700*	*p =3·10^{-10} (bar)*	*With plasma*	
I_h **(A)**	V_h **(A)**	$\mathbf{R}/R_0$	T_p **(K)**	V_f **(V)**
1,00	1,11	3,9487	885,22	8,8
1,20	1,59	5,3269	1129,51	9,7
1,30	1,85	5,9556	1236,99	10,4
1,40	2,12	6,5403	1334,13	17,8
1,50	2,39	7,0470	1418,31	23,8
1,55	2,51	7,2138	1444,49	26,5
1,60	2,67	7,5304	1496,57	29,2
1,70	2,97	8,0324	1577,25	30,5
1,75	3,10	8,1886	1602,89	31,1
1,80	3,24	8,3718	1631,63	31,1
1,85	3,41	8,6490	1676,13	31,5
1,90	3,57	8,8779	1712,49	31,7
2,00	3,89	9,3013	1778,48	32,3

Table 6: Probe I ($r_p = 5 \cdot 10^{-5}m$) measurements in the presence of plasma at a given condition (I). $p_{chamber} = 3{\cdot}10^{-8}$ (bar)

Probe II	*Test_20180528_1800*	*p =3·10^{-10} (bar)*	*With plasma*	
I_h **(A)**	V_h **(V)**	$\mathbf{R}/R_0$	T_p **(K)**	V_f **(V)**
0,10	1,59	5,0000	1072,31	3,5
0,13	2,39	5,8282	1214,98	3,2
0,14	2,73	6,2000	1277,38	3,4
0,16	3,26	6,4917	1325,84	4,3
0,18	4,31	7,6815	1520,86	16,9
0,20	5,01	8,0500	1580,48	26,6
0,21	5,71	8,7635	1693,54	29,9
0,22	5,99	8,7758	1696,71	31,3
0,23	6,38	8,9464	1723,53	32,5
0,24	6,68	8,9778	1728,29	33,8
0,25	6,99	9,0200	1734,55	33,6

Table 7: Probe II ($r_p = 1.25 \cdot 10^{-5}m$) measurements in the presence of plasma at a given condition (I). $p_{chamber} = 3{\cdot}10^{-8}$ (bar)

Probe II	*Test_20180525_1612*	*p =3·10^{-10} (bar)*	*With plasma*	
I_h **(A)**	V_h **(V)**	$\mathbf{R}/R_0$	T_p **(K)**	V_f **(V)**
0,08	0,61	2,2417	558,16	3,5
0,09	0,96	3,2556	757,15	2,6
0,10	1,26	3,9000	876,06	2,5
0,11	1,57	4,4576	977,11	2,5
0,12	1,87	4,8944	1053,07	2,4
0,13	2,21	5,3667	1136,40	2,4
0,14	2,83	6,4381	1317,50	5,4
0,15	3,17	6,7444	1367,27	8,3
0,16	3,57	7,1375	1433,05	11,3
0,17	3,93	7,4059	1477,09	10,5
0,18	4,26	7,5889	1506,30	14,9
0,19	4,54	7,6649	1517,62	19,9
0,20	5,03	8,0833	1585,27	24,0
0,21	5,45	8,3508	1628,45	29,2
0,22	5,72	8,3667	1631,63	32,5
0,23	6,37	8,9319	1720,38	33,4
0,24	6,78	9,1167	1750,26	33,3
0,25	7,12	9,1933	1761,25	33,6

Table 8: Probe II ($r_p = 1.25 \cdot 10^{-5} m$) measurements in the presence of plasma at a given condition (I). $p_{chamber} = 3{\cdot}10^{-8}$ (bar)

C.3 Plasma Condition II. Thruster operating at $\dot{m} = 10 sccm$

Probe I	*Test_20180529_1700*	*p =3·10^{-10} (bar)*	*With plasma*	
I_h **(A)**	V_h **(V)**	$\mathbf{R}/R_0$	T_p **(K)**	V_f **(V)**
1,40	2,11	6,4945	1325,84	35,8
1,50	2,36	6,9188	1396,95	42,7
1,60	2,64	7,4103	1477,09	49,0
1,70	2,93	7,8816	1553,13	54,0
1,80	3,23	8,3362	1630,53	57,3
1,90	3,55	8,8104	1701,44	58,9
2,00	3,89	9,3013	1778,48	59,8

Table 9: Probe I ($r_p = 5 \cdot 10^{-5} m$) measurements in the presence of plasma at a given condition (II). $p_{chamber} = 3{\cdot}10^{-10}$ (bar)

Probe II	*Test_20180529_1800*	*p =3·10^{-10} (bar)*	*With plasma*	
I_h **(A)**	V_h **(V)**	$\mathbf{R}/R_0$	T_p **(K)**	V_f **(V)**
0,20	5,09	8,1833	1601,30	37,8
0,22	5,81	8,5030	1652,40	46,9
0,24	6,46	8,6722	1679,31	59,5
0,25	7,12	9,1933	1761,31	66,0

Table 10: Probe II ($r_p = 1.25 \cdot 10^{-5} m$) measurements in the presence of plasma at a given condition (II). $p_{chamber} = 3{\cdot}10^{-10}$ (bar)

C.4 Plasma Condition III. Thruster operating at $\dot{m} = 15 sccm$

Probe I	*Test_20180529_1900*	*p =3·10^{-10} (bar)*	*With plasma*	
I_h **(A)**	V_h **(V)**	$\mathbf{R}/R_0$	T_p **(K)**	V_f **(V)**
1,40	2,13	6,5861	1342,45	27,0
1,50	2,40	7,0897	1424,89	34,2
1,60	2,66	7,4904	1490,12	36,8
1,70	2,95	7,9570	1566,02	40,0
1,80	3,26	8,4430	1646,45	40,4
1,90	3,58	8,9116	1717,25	41,5
2,00	3,89	9,3013	1778,56	41,8

Table 11: Probe I ($r_p = 5 \cdot 10^{-5} m$) measurements in the presence of plasma at a given condition (III). $p_{chamber} = 3{\cdot}10^{-10}$ (bar)

Probe II	*Test_20180529_1930*	*p =3·10^{-10} (bar)*	*With plasma*	
I_h **(A)**	V_h **(V)**	$\mathbf{R}/R_0$	T_p **(K)**	V_f **(V)**
0,20	5,32	8,5667	1663,41	34,8
0,22	6,33	9,2909	1777,00	40,9
0,24	7,14	9,6167	1828,57	42,3
0,25	7,48	9,6733	1836,36	42,7

Table 12: Probe II ($r_p = 1.25 \cdot 10^{-5} m$) measurements in the presence of plasma at a given condition (III). $p_{chamber} = 3{\cdot}10^{-10}$ (bar)

D Project Budget

The aim of this section is to asses the main costs associated to the development of the project. The main elements to take into account are specified below.

- **Software tools**. Matlab has been used to perform the simulations of the models. Microsoft Excel was used in the lab to take and compare data as the experiments took place. Solid edge was used for CAD design. For all of them, academic licenses were used, and there exist free alternatives as Python, OpenOffice and FreeCAD. For that reason, these costs have been disregarded.
- **Materials**.
  - Thoriated tungsten wire average price oscillates around 15 €/m. It is estimated that during manufacturing process, 50 cm of filament were used or waisted.
  - The 30 mm alumina tube used is priced at 233 €. It is estimated that 15 mm of length were used, accounting for 116.5 €.
  - The Kapton® Insulated Wire and Cable used inside the chamber to feed the probes is priced at 105 €per 1.5 m. One cable of one meter was used in each probe, which amounts for 140 €
  - Other items as the copper cables used inside the probes, male and female pins, thermo retractile material and other consumable goods, can be estimated to have a cost about 10 €.
  - The total material cost for the conventional probes manufactured is then 274 €.
  - LaB_6 powder is priced at 729 €/100g. CeB_6 powder was fabricated at UC3M by a former student. Since it has not been possible to finally manufacture a useful tip, these costs are disregarded for this project.
- **Hardware tools**.
  - A BK Precision PVS60085MR power source is priced at 4.779,50 €
  - A Keithley 6487 voltage source is priced at 6.509,80 €
  - A Leybold Univex S XTT space simulator is only sold under budget request.
  - The helicon thruster is granted to the university by SENER and it is not priced. The argon gas that was using as fuel is priced at 89 €per 50 L from industrial suppliers.
  - Other associated costs:

    * Manual tools to machine the probes: diamond electric saw (≈ 200 €), tin welder (449 €), heat gun (1999 €).
    * Electricity to power all the tools during manufacturing and during testing phases (vacuum pumps, computers, voltage/power sources and the probes). These figures are unknown but power consumption in the lab is expected to be high.

- **Workload**.
  - The time spent by the author researching, manufacturing, setting the experiment and testing the probes is roughly estimated to be 500 hours over the period of 7 months.
  - It should be also taken into account the amount of time spent by other researchers, PhD students and shop technicians when it came to put together the experimental set up.

Bibliography

[1] M. Bakr et al. Comparison between the hexaboride materials as thermionic cathode in the rf guns for a compact mir-fel driver. *Zero-Carbon Energy Kyoto, pp. 202-210*, 2009.

[2] J.D. Callen. Fundamentals of plasma physics. *p. 16*, 2003.

[3] M.D. Campanell. An alternative model of space-charge limited thermionic current flow through a plasma. 2017.

[4] F.F. Chen. Introduction to plasma physics and controlled fussion. *Volume 1, Chapters 1 & 7*, 1974.

[5] X. Chen. Review on low-work-function materials. 2017.

[6] X. Chen and G. Sanchez-Arriaga. Current-voltage and floating potential characteristics of cylindrical emissive probes from a full-kinetic model based on the orbital motion theory. 2017.

[7] X. Chen and G. Sanchez-Arriaga. Orbital motion theory and operational regimes for cylindrical emissive probes. *Phys. Plasmas 24, 023504*, 2017.

[8] P. Coakley, N. Hershkowitz, and J.R. Smith. Inflection point method of interpreting emissive probe characteristics. *Rev. Sci. Instrum. 50*, 1979.

[9] National Research Council. Plasma processing of materials: Scientific opportunities and technological challenges. *The National Academies Press*, 1991.

[10] CRC. Handbook of chemistry and physics. *98th edition*, 2017.

[11] L.H. Damon. The making of lab6 crystals. *Microscopy Today Vol. 3, Iss. 2, pp. 18-19*, 1995.

[12] P. D. Desai, T.K. Chu, H.M. James, and C.Y. Ho. Electrical resistivity of selected elements. *J. Phys. Chem. Ref. Data 13, 1069 pp. 1091-1095*, 1984.

[13] L.A. DuBridge. A further experimental test of fowler's theory of photoelectric emission. *Phys. Rev. 39*, 1932.

[14] J.L. Dye. Anionic electron in electrides. *Nature 365, 10–11*, 1993.

[15] R.D. Estes and J.R. San Martin. Cylindrical langmuir probes beyond the orbital-motion-limited regime. *Phys. Plasmas 7, No 10*, 2000.

[16] D. Agaogullary et al. Preparation of lab6 powders via calciothermic reduction using mechanochemistry and acid leaching. *ONA Powder and Particle Journal*, 2015.

[17] N.J. Fisch, N. Hershkowitz, I. Kaganovich, Y. Raitses, and J.P. Sheehan. A comparison of emissive probes techniques for electric potential measurements in a complex plasma. *Physics of Plasmas, Vol 18, No. 7*, 2011.

[18] G.N. Fursey. Field emission in vacuum microelectronics. 2005.

[19] G. Gaertner. Historical development and future trends of vacuum electronics. *Journal of Vacuum Science & Technology, 30*, 2012.

[20] W.F. Gale and T.C. Totemeier. Electron emission. *Smithells Metals Reference Book*, 2003.

[21] A.D. Gallimore and J.M. Haas. Internal plasma potential profiles in a laboratory-model hall thruster. *Phys. Plasmas 8, 652*, 2001.

[22] D. Gates, B. Hershkowitz, N.and Nelson, and J. Pew. Self emissive probes. *Review of Scientific Instruments*, 1983.

[23] R.J. Goldston and P.H. Rutherford. Introduction to plasma physics, pp. 1-2. *Taylor and Francis Group*, 1995.

[24] M. Grätzel. Photoelectrochemical cells. *Nature, Vol 414, pp. 338–344*, 2001.

[25] N. Hershkowitz. How langmuir probes work. *Plasma Diagnostics Vol. 1, pp. 113-183*, 1989.

[26] N. Herskowitz and J.P. Sheehan. Emissive probes. *Plasma Sources Sci. Technol.*, 2011.

[27] G.D. Hobbs and J.A. Wesson. Heat flow through a langmuir sheath in the presence of electron emission. *Plasma Physics.Vol.9. pp. 85-87*, 1967.

[28] G.D. Hobbs and J.A. Wesson. A review of thermionic cathodes. *Vacuum Vol. 19, Iss. 8, pp. 353-359*, 1969.

[29] J. Holzl and F.K. Schulte. Work function of metals. *Solid surface physics*, 1979.

[30] I.H. Hutchinson. Principles of plasma diagnostics. *Chapter 1: Plasma Diagnosis and Chapter 3.2 : Probes in collisionless plasmas without magnetic fields*, 1987.

[31] R.W. Johnson and A.H. Daane. The lanthanum-boron system. *Institute for Atomic Research and Department of Chemistry, Iowa State University*, 1960.

[32] R.W. Johnson and A.H. Daane. Thermionic emission properties of a lanthanum hexaboride/rhenium cathode. *J. Appl. Phys. 16*, 1965.

[33] R.F. Kemp and J. M. Sellen. Plasma potential measurements by electron emissive probes. *Review of scientific Instruments, 37*, 1966.

[34] W. Ketterle. Twenty years of atomic quantum gases: 1995 - 2015. *Universal Theme of Bose-Einstein Condensation, Cambridge University press*, 2017.

[35] K.A.A Khalid, T.J. Leong, and K. Mohamed. Review on thermionic energy converters. *IEEE Transactions on Electron Devices, Vol 63, Iss. 6*, 2016.

[36] S.W. Kim and H. Hosono. Synthesis of a room temperature stable 12cao·7al2o3 electride from the melt and its application as an electron field emitter. *Chem. Mater., 18, pp. 1938–1944*, 2006.

[37] M.M. KorsukovaV, N. Gurin, T. Lundström, and E. Tergenius. The structure of high-temperature solution-grown lab6: A single-crystal diffractometry study. *Journal of the Less Common Metals Vol. 117, pp. 73-81*, 1986.

[38] J.M. Lafferty. Boride cathodes. *Journal of Applied Physics Vol. 22*, 1951.

[39] J.G. Laframboise. Tbeory of sphierical and cylindrical langmuir probes in a collisionless, maxwellian plasma at rest. 1966.

[40] I. Langmuir. The effect of space charge and residual gases on thermionic currents in high vacuum. *Phys. Rev. 2, 450*, 1913.

[41] I. Langmuir. Oscillations in ionized gases. *Proc. Nat. Acad. Sci. U.S., vol. 14, p. 628*, 1928.

[42] I. Langmuir and H.M. Mott Smith. The theory of collectors in gaseous discharges.

[43] P.R. Lauren and J.D. Williams. A calcium aluminate electride hollow cathode. *IEEE Transactions on Plasma Science Vol. 43, pp. 190-194*, 2014.

[44] R.B. Lobbia. Recommended practice for use of langmuir probes in electric propulsion testing. *J. Propul. Power, Vol. 33, No. 3*, 2017.

[45] T. Lundström. Structure, defects and properties of some refractory borides. *Pure & Appl. Chem., Vol. 57, No. 10, pp. 1383—1390*, 1985.

[46] J.M. Martin, J. Bonde, W. Gekelman, and P. Pribyl. A resistively heated ceb6 emissive probe. *Review of Scientific Instruments, 86*, 2015.

[47] M.L. Minges and G.K. White. Thermophysical properties of some key solids: An update. *Int. J. Thermophys. 18*, 1997.

[48] K. Morita, H. Zen, K. Masuda, K. Torgasin, T. Katsurayama, T. Murata, S. Suphakul, H. Yamashita, T. Nogi, T. Kii, K. Nagasaki, and H. Ohgaki. Photoemission properties of lab6 and ceb6 under various temperature and incident photo energy conditions. *Proceedings of IPAC2016, Busan, Korea*, 2016.

[49] K.J. Morris. Cold isostatic pressing. *Concise Encyclopedia of Advanced Ceramic Materials, pp. 84–88*, 1991.

[50] K. Nishikawa and M. Wakatani. Plasma physics: Basic theory with fusion applications. 1994.

[51] D.N. Nkwetta and F. Haghighat. Thermal energy storage with phase change material — a state-of-the art review.

[52] R. Opher. Introduction to plasma astrophysics. *Plasma Physics and Controlled Fusion, Vol. 41.*

[53] D. Pedrini et al. Development of hollow cathodes for space electric propulsion at sitael. *Aerospace, 4*, 2017.

[54] F. Righini, J. Spigiak, G.C. Bussolino, A. Rosso, and G.K. White. Thermophysical properties of thoriated tungsten above 3600 k by a pulse-heating method. *Int Jour. of Thermophys. Vol. 17. No. 5,*, 1996.

[55] D.S. Sahota and K. Shelly. Review paper on resistance spot welding of austenitic stainless steel 316. *IJETT Vol. 47 No. 7*, 2017.

[56] E. Sani, L. Mercatelli, M. Meucci, L. Zoli, and D Sciti. Lanthanum hexaboride for solar energy applications. *Scientific Reports Vol. 7, No. 718*, 2017.

[57] R. Schrittwieser and et al. Measurements with an emissive probe in the castor tokamak. *Plasma Physics Control Fusion 44*, 2002.

[58] H. Seiler. Secondary electron emission in the scanning electron microscope. *Journal of Applied Physics 54*, 1983.

[59] J.P. Sheehan. Recommended practice for use of emissive probes in electric propulsion testing. *J. Propul. Power*, 2017.

[60] J.K. Shultis and R.E. Faw. Fundamentals of nuclear science and engineering. *Taylor and Francis Group*, 2002.

[61] G.P. Sutton. Rocket propulsion elements. *A Wiley-Interscience Publication*, 2001.

[62] Y. Toda, H. Yanagui, E. Ikenaga, J.J Kim, M. Kobata, S. Ueda, T. Kamiya, M. Hirano, K. Kobayasi, and H. Hosono. Work function of a room-temperature, stable electride [ca24al28o64]4+(e–)4. *Advanced Materials, 19*, 2007.

[63] Y. Toda et al. Field emission of electron anions clathered in subnanometer sized cages in [ca24al28o64]4+(e–)4. *Adv. Mater., 16 No. 8*, 2004.

[64] P. Tolias. Analytical expressions for thermophysical properties of solid and liquid tungsten relevant for fusion applications. *Space and Plasma Physics, Royal Institute of Technology, Sweden*, 2017.

[65] D.M. Trucchi and N.A. Melosh. Electron-emission materials. *MRS Bulletin, Vol. 42, Iss. 7, pp. 488-492*, 2017.

[66] K. Tsougenia, A. Bourkoula, P. Petrou, A. Tserepi, S.E. Kakabakos, and E. Gogolides. Photolithography and plasma processing of polymeric lab on chip for wetting and fouling control and cell patterning. *Microelectronic Engineering Vol. 124, pp. 47-52*, 2014.

[67] M.D. Williams, L.T. Jackson, D.O. Kippenhan, K.N. Leung, M.K. West, and C.K. Crawford. Lanthanum hexaboride (lab6) resistivity measurement. *Appl. Phys. Letters, 50*, 1987.

[68] T.M. York and H.B. Tang. Introduction to plasmas and plasma dynamics. *With Reviews of Applications in Space Propulsion, Magnetic Fusion and Space Physics*, 2015.